

EFFECT OF SURFACE LIGANDS AND SURFACE DEFECTS ON THE ELECTRONIC
AND OPTICAL PROPERTIES OF QUANTUM DOTS

A Dissertation
Submitted to the Graduate Faculty
of the
North Dakota State University
of Agriculture and Applied Science

By

Naveen Kumar Dandu

In Partial Fulfillment of the Requirements
for the Degree of
DOCTOR OF PHILOSOPHY

Major Department:
Chemistry and Biochemistry

November 2016

Fargo, North Dakota

North Dakota State University
Graduate School

Title

EFFECT OF SURFACE LIGANDS AND SURFACE DEFECTS ON THE
ELECTRONIC AND OPTICAL PROPERTIES OF QUANTUM DOTS

By

Naveen Kumar Dandu

The Supervisory Committee certifies that this *disquisition* complies with North Dakota State University's regulations and meets the accepted standards for the degree of

DOCTOR OF PHILOSOPHY

SUPERVISORY COMMITTEE:

Dr. Svetlana V. Kilina

Chair

Dr. Wenfang Sun

Dr. John Hershberger

Dr. Erik K. Hobbie

Dr. Andrei Kryjevski

Approved:

11/17/2016

Date

Dr. Gregory Cook

Department Chair

ABSTRACT

Quantum dots (QDs) have drawn a special attention since recent past due to their properties such as broad range absorption ability, size tunable narrow emission, high extinction coefficients, and charge carriers ability. Nonetheless, imbalanced surface passivation/defects leads to the appearance of surface trap states inside the band gap, affecting both radiative and non-radiative dynamics. Experimentally, it is difficult to explore the effect of surface states as they are optically inactive. However, computations provide valuable insights to these characteristics. We performed calculations using density functional theory (DFT) and time-dependent DFT (TDDFT) to provide our insights to such effects.

Firstly, we performed DFT studies to understand the effect of QD- ligand interactions on their photophysical properties. Our studies on thiols passivated CdSe QDs showed that passivation of their surface by equilibrium concentration of neutral thiols and negatively charged thiolates is essential to achieve photoluminescence (PL) enhancement. Additionally, we investigated the effect of surface defects on photophysical properties of silicon QDs. Our results showed that defects introduce mid gap states inside band-gap. Absorption spectra showed the appearance of dark/semi-dark states at the first energy band, proving that the surface states quench PL efficiency in QDs.

Secondly, we studied the effect of QD-QD interactions on their optoelectronic properties. In collaboration with the experimental group from Prof. Hobbies' lab, we studied interactions between defective and non-defective QDs. Calculated Forster Resonance Energy Transfer rates suggest that all the trap states in a defective QD would be filled by the excited electrons from the non-defective QD and thus emission happens from the highest bright energy state. We proposed this as the reason for the experimental observation of the increased on-time blinking and overall

enhancement of PL in these QDs. Furthermore, in collaboration with experimentalists from Los-Alamos National Lab, we have provided our insights into the chemical engineering of self-assembling of PbSe QDs into (100) directed 2D nanoplates. Our surface energy calculations on the oriented attachments revealed that 2D nanoplates grown in (100) are more feasible than 3D quantum dots. Overall, our calculations not only supported the experimental findings, but also provided solutions to questions raised by experimentalists.

ACKNOWLEDGEMENTS

During my time at North Dakota State University, I am very fortunate to interact with many talented scientists and instructors. I am especially very grateful to my PhD advisor, Dr. Svetlana Kilina, for being not just an advisor, but also a great mentor. She taught me how to do a meaningful research, effectively and efficiently. I truly could not have found a better advisor and mentor for my graduate studies. She has made me a better communicator, and a computational chemist.

I am extremely grateful to Dr. Dmitri Kilin for his invaluable effort in helping me to improve my technical knowledge and presentation skills. He stood like a second advisor in every respect throughout my graduate studies.

I place on record, my sincere gratitude to Prof. Wenfang Sun, Prof. John Hershberger, Prof. Erik Hobbie and Dr. Andrei Kryjevski for agreeing to serve as committee members for my PhD dissertation defense and for their constant support and feedback.

Additionally, a special thanks to Prof. Wenfang Sun and Prof. Erik Hobbie for being my direct experimental collaborators. It has been an irreplaceable experience working with them. I am also thankful to my other collaborators, Dr. Sergei Tretiak, Dr. Victor Klimov and Dr. Kirill Velizhanin from Los Alamos National Lab, for their help and support.

I am thankful to Center for Computationally Assisted Science and Technology (CCAST) at North Dakota State University for providing computational resources and support for my research.

Thanks to all the members of Kilina group: Brendan, Jabed, Levi, Peng, Dr. Tamukong, Mary, Dinusha, Bryan, Whitney and Braden for their scientific discussions. A special thanks to

Brendan, Javed and Levi for the support and friendship. It was truly an honor to work with this group.

I would also like to thank my friends and coffee-mates in the department for the never-ending support and discussions on various topics. I can't imagine my graduate experiences without them.

A special thanks to my friends at Fargo who made all these years incredibly fun filled. Thank you all for making my stay more enjoyable.

I thank my best friend Manoj Rudraraju for his constant motivation and support whenever needed.

Finally, I thank my family, to whom this dissertation is dedicated. My parents always encouraged me to pursue my passion and have supported me in every endeavor. My sister and brother-in-law has always been very supportive in every aspect. Lastly, I thank my wife Madhu for so many things. Thanks for going through this together and for the love and support.

DEDICATION

To my family

TABLE OF CONTENTS

ABSTRACT.....	iii
ACKNOWLEDGEMENTS.....	v
DEDICATION.....	vii
LIST OF TABLES.....	xii
LIST OF FIGURES.....	xiii
LIST OF EQUATIONS.....	xvi
LIST OF ABBREVIATIONS.....	xix
LIST OF SYMBOLS.....	xx
1. INTRODUCTION.....	1
1.1. Quantum Dots.....	1
1.2. Synthesis of QDs.....	3
1.3. Effect of Surface Chemistry on Photophysics of Quantum Dots.....	4
1.4. Role of Computational Modeling.....	5
1.5. Objectives and Outline.....	7
1.6. References.....	8
2. THEORETICAL FRAMEWORK.....	14
2.1. Introduction to Quantum Mechanical Calculations.....	14
2.1.1. The Many-body Problem.....	15
2.1.2. The Hohenberg and Kohn Theorems.....	17
2.1.2.1. HK Theorem 1.....	17
2.1.2.2. HK Theorem 2.....	17
2.1.3. The Kohn-Sham Method.....	18
2.1.4. The Exchange Correlation Functional.....	18
2.1.4.1. Local Density Approximation (LDA).....	19

2.1.4.2. Generalized Gradient Approximation (GGA)	20
2.1.4.3. meta-GGA.....	20
2.1.4.4. Hybrid Functionals.....	20
2.1.5. The Basis Sets.....	22
2.1.5.1. Localized Basis Sets	22
2.1.5.2. Plane Waves and Grids	23
2.1.6. Pseudopotentials	24
2.2. Computational Methodology.....	24
2.3. Electronic Structure.....	25
2.3.1. Density of States.....	25
2.4. Optical Properties	25
2.4.1. The Runge-Gross Theorem	25
2.4.2. The Quantum Mechanical Action	26
2.4.3. The Time-dependent Kohn-Sham Equations	27
2.4.4. The Linear Response Theory.....	28
2.4.5. Plotting Absorption Spectra	29
2.5. References	30
3. EFFECT OF SURFACE LIGANDS ON ELECTRONIC AND OPTICAL PROPERTIES OF QUANTUM DOTS	32
3.1. Effect of Thiols Capping on the Electronic and Optical Properties of CdSe QDs.....	33
3.1.1. Introduction	33
3.1.2. Computational Details	34
3.1.2.1. Structural Models.....	34
3.1.2.2. Electronic Structure and Optical Response Calculations.....	35
3.1.3. Results and Discussion	35
3.1.3.1. Structure Optimization of QDs	35

3.1.3.2. Natural Bond Order (NBO) Analysis	37
3.1.3.3. Electronic Properties of QDs	38
3.1.3.4. Absorption Spectra.....	41
3.1.4. Conclusions	45
3.2. Effect of Surface Oxidation of PbSe QDs on their Optoelectronic Properties	47
3.2.1. Introduction	47
3.2.2. Computational Details.....	48
3.2.2.1. Structural Models.....	48
3.2.2.2. Computational Methodology	49
3.2.3. Results and Discussions	49
3.2.3.1. Binding Energy	49
3.2.3.2. Density of States	53
3.2.4. Absorption Spectra	55
3.2.5. Natural Transition Orbitals.....	55
3.2.6. Conclusions	58
3.3. References	59
4. EFFECT OF LIGANDS PASSIVATED QUANTUM DOT – QUANTUM DOT INTERACTIONS ON THEIR OPTOELECTRONIC PROPERTIES	64
4.1. Enhanced Luminescent Stability through Particle Interactions in Silicon Nanocrystal Aggregates	65
4.1.1. Introduction	65
4.1.2. Computational Details.....	66
4.1.2.1. Structural Models and Their Optimization	66
4.1.2.2. Absorption Spectra.....	66
4.1.2.3. Förster Resonance Energy Transfer.....	67
4.1.3. Results and Discussions	67

4.1.4. Conclusions	79
4.2. Deeper Understanding of Surface Chemistry in Engineering Oriented Attachment in the Formation of Two Dimensional PbSe Nanoplates	80
4.2.1. Introduction	80
4.2.2. Computational Details	83
4.2.2.1. Gaussian Calculations of Isolated QDs with Ligand Passivation	83
4.2.2.2. VASP Calculations of 1-D, 2-D and 3-D QD-based Supersolids.....	83
4.2.2.3. Calculations of the Surface Energy.....	85
4.2.3. Results and Discussions	88
4.2.4. Conclusions	97
4.3. References	98

LIST OF TABLES

<u>Table</u>	<u>Page</u>
3.1. Initial and relaxed geometries of both protonated and deprotonated thiols functionalized CdSe QDs. Structures are labelled from 1(a) to 1(g) and these notations were used in description.....	36
3.2. Natural bond order charge analysis values of each of thiol capped QDs	39
3.3. HOMO and LUMO of the relaxed geometries in acetonitrile solvent.....	43
3.4. NTOs of 4 different cases in acetonitrile solvent.....	45
3.5. Comparison between oxygen ions and oxygen atoms of selected systems in both vacuum and in solvent (acetonitrile). Difference in binding energy (eV) is more pronounced in the case of oxygen ions.....	51
3.6. Lowest binding energy of three different mode of oxygen: atomic oxygen (O-atoms), ionic oxygen (O ²⁻) and molecular oxygen (O ₂) in each facet on Pb ₆₈ Se ₆₈ in vacuum.....	52
3.7. Surface reconstruction due to increase in the concentration of oxygen at (100) facet of 2 nm PbSe QD.....	53
3.8. Absorption spectra of oxygen atoms passivated PbSe QD.....	57
3.9. NTOs of selected systems that show some significant contributions	58
4.1. Size confinement effect in Si QDs.....	68
4.2. Natural transition orbitals (NTOs) contributing to the first excited state of the neutral and charged Si ₂₉ and Si ₃₅ QDs with methane passivation. The arrows mark the location of the surface defect, e.g., the Si ion from which two ligands are lost (L).....	74
4.3. The lifetime of the lowest excited state was calculated using the Einstein coefficients for spontaneous emission.....	78
4.4. Binding energy of single ligand on different surfaces	90
4.5. Binding energy per ligand calculated in case of attachment of multiple ligands on different surfaces	90
4.6. Surface energy of the (PbSe) ₆₈ quantum dot passivated by PbCl ₂ ligands in either 110 or 111 or both as labelled below. Values in parenthesis show surface energies for (PbSe) ₆₈ quantum dot passivated by 12 PbCl ₂ ligands on 110 surface growing along x and y directions. The z direction is passivated by 6 methyl amines on each side.	94
4.7. VASP optimized structures of the (PbSe) ₆₈ and (PbSe) ₁₆ quantum dot passivated by PbCl ₂ ligands in either 110 or 111 or both as labelled below	95

LIST OF FIGURES

<u>Figure</u>	<u>Page</u>
1.1. Energy levels band alignment.....	2
1.2. Effect of size confinement on emitting color.....	3
2.1. Schematic diagram of HK Theorem	17
2.2. Schematic diagram of Jacob’s Ladder	19
3.1. Total DOS of the QD in presence of amine and acetonitrile in absence and presence of ligands	40
3.2. Fragmented DOS of QD passivated by thiols in acetonitrile solvent in case of (a) mostly deprotonated ligands, (b) less deprotonated, (c) completely protonated and (d) completely deprotonated.....	41
3.3. Absorption spectra of the all four cases in presence of vacuum, propyl amine and acetonitrile solvents as indicated in the graphs (a) partially deprotonated, (b) mostly deprotonated, (c) completely deprotonated and (d) completely protonated.	44
3.4. Different facets on the structure colored differently on each surface to identify the facet. There are 6 yellow surfaces are facet 100, 12 purple surfaces are facet 110 and 8 blue surfaces are facet 111, totaling up to 26 surfaces on the QD.....	48
3.5. Different species of oxygens binding energies on Pb ₁₆ Se ₁₆ QD at different facets with (a) single oxygen molecule (b) single oxygen atom and (c) single oxygen ion	50
3.6. Representations of Fragmented DOS (FDOS) of few selected systems where several observations were made. In graph (1), there is a lost and broadening of peaks which is generating a slight blue shift. In graph (2), there is also lost in peaks that leads to blue shift. In graph (3), there is a narrow bandgap contributed by oxygen (oxygen lines scaled to 4 for representation).	54
3.7. Corresponding absorption spectra for the DOS plots in Figure 3.2 where graph (a) shows pristine Pb ₁₆ Se ₁₆ absorption spectra to compare with selected systems (b), (c) and (d). The blue shift can be observed on (b) and (c) while the first peak that contributes to red shift observed with oscillation strength of 0.004 in graph (d).....	56
4.1. Optimized structures of fully passivated (F) and ligands removed (L) Silicon QDs.....	68
4.2. Density of states of fully passivated Si QD (F) in neutral and charged systems	69
4.3. Density of states of two ligands removed Si QD (L) in neutral and charged systems	70

4.4. Calculated ground and excited state electronic structure of methane passivated Si ₂₉ and Si ₃₅ . Top and middle panels represent absorption spectra of neutral fully passivated (F) and with two lost ligands (L) Si clusters (top) and F and L clusters with -2 and +2 charge. The vertical arrows define the lowest-energy transitions. The highlighted pattern represents excitation energy range of 2.4 - 3.0 eV, corresponding to the donor. Bottom panel represents the ground state density of states (DOS) of the neutral and charged Si ₂₉ QD with full passivation (F) and with defects in the passivation (L).	73
4.5. The Forster energy transfer times between two methane passivated Si ₂₉ and Si ₃₅ QDs separated by the distance of ~1 nm. (a) The donor QD is excited at the range of 2.4 to 3.0 eV (marked by yellow pattern in Figure 2). (b) The donor QD is excited to the brightest state in the range of 4 - 5 eV. X-axis represents the acceptor QD with the same or different size and structure as compared to a donor. For both panels, solid lines correspond to the donor QD of a small size (Si ₂₉), while dashed lines correspond to the donor QD of the larger size (Si ₃₅).....	75
4.6. Top panel represents absorption spectra of the neutral and charged Si ₆₆ QD with full passivation by methane ligands (F) and with two ligands lost (L) from the Si ion on the surface. Bottom panel represents Density of States (DOS) of neutral fully passivated Si ₆₆ , Si ₃₅ , Si ₂₉ QDs. The confinement effect is well seen: the larger the QD, the smaller the gap.	76
4.7. Possible pathways for an exciton transfer (also called the energy transfer) between neighboring Si nanocrystals; the size of bold arrows qualitatively correspond to rates of the energy transfer. Left structures have no surface defects resulted in less number of optically dark (grey dashed lines) and semi-dark (dashed green lines) lowest-energy trap states. Right structures have surface defects, e.g., lost ligands from Si sites, marked by the grey ovals.....	77
4.8. FRET rate of all contributions (solid) and in the dipole approximations (dashed) between methane passivated Si ₂₉ as a function of separation from 0.1 nm to 10 nm.	79
4.9. (a) HR-TEM image of PbSe NPL synthesized using PbCl ₂ precursor. Inset: a selective area electron diffraction pattern, verifying the rock-salt crystal structure. (b) Top-down and (c) side-on TEM images of face-to-face stacks of NPLs (d) Absorption (solid) and PL (dashed) spectra of NPLs synthesized using PbCl ₂ . Inset: The PL spectrum redshifts slightly as QDs attach into NPLs, then remains constant. ²⁵	82
4.10. 100 surface of (PbSe) ₆₈ quantum dot with 12 PbCl ₂ on 110 surfaces growing in x, x', y and y'	87

- 4.11. (a) Represents three main crystallographic surfaces of $(\text{PbSe})_{68}$: six (100), twelve (110) passivated by PbCl_2 ligands, and four Pb-terminated and four Se-terminated (111). Selenium atoms are colored in yellow, leads are in grey, and chlorines are in green. The binding energy between the $(\text{PbSe})_{68}$ QD and different ligands calculated in propyl amine solvent media. (b) A single ligand attached on (100), (110), and (111) crystal lattice surfaces of the QD. (c) Multiple ligands passivate either (100), or (110), or (111) surfaces of the QD..... 89
- 4.12. Gaussian simulations of two PbSe QDs passivated with amines on 5 different (100) sites and PbCl_2 on (110). After relaxation, PbCl_2 at (110) tend to form a bridge between two QDs. 92
- 4.13. (a) and (b) are the geometries of $(\text{PbSe})_{68}$ QD passivated fully at (110) surface by PbCl_2 , before and after relaxation utilizing periodic boundary conditions to mimic QD-QD interactions in 2-D and 3-D directions. 2D network is stabilized due to formations of Pb-Cl-Pb bridging bonds selectively connecting neighboring QDs along (100) surface. Zoomed in pictures of before and after relaxations were projected to show the better visualization of the Pb-Cl-Pb bridge formations (c) Optimized geometry of 2-D structure constructed from $(\text{PbSe})_{68}$ QD with fully passivated (110) surface by PbI_2 ligands. Lacking of Pb-I-Pb bridging bonds reduce ordering and destabilize the 2-D array. (d) The calculated surface energy as a function of 2-D and 3-D super lattices constructed from $(\text{PbSe})_{16}$ or $(\text{PbSe})_{68}$ QDs with PbCl_2 ligands passivating either (110) or (111) or both surfaces with and without NH_2Me ligands capping (100) facets inactive in 2-D array formation. 93
- 4.14. Geometry relaxation of $(\text{PbSe})_{68}$ quantum dot passivated by 12 PbCl_2 ligands in either 110, with amines on (100) direction. (a) PbI_2 is placed at (100) and relaxed (b) PbCl_2 is placed at (100) and relaxed..... 97

LIST OF EQUATIONS

<u>Equation</u>	<u>Page</u>
2.1. Schrödinger equation	15
2.2. Hamiltonian operator	15
2.3. Electronic Hamiltonian	16
2.4. Born-Oppenheimer approximation	16
2.5. Slater determinants.....	16
2.6. Ground state electron density.....	17
2.7. Exact ground state energy functional.....	17
2.8. Kohn-Sham functional	18
2.9. One-particle Kohn-Sham equation	18
2.10. Kohn-Sham potential	18
2.11. Exchange-correlation potential	18
2.12. Local density approximation.....	19
2.13. Generalized gradient approximation.....	20
2.14. Exchange-correlation functional.....	20
2.15. Exact exchange energy term	21
2.16. Becke exchange correlation	21
2.17. PBE1PBE exchange correlation	21
2.18. Basis set	22
2.19. Slater type orbitals	22
2.20. Gaussian type orbitals	22
2.21. Periodic systems.....	23
2.22. Bloch's function.....	23
2.23. Plane waves periodicity	23

2.24. Electronic wavefunction	23
2.25. Kinetic energy cut-off	24
2.26. Pseudopotentials	24
2.27. Density of states	25
2.28. Time-dependent electron density	26
2.29. Action integral	26
2.30. Time-dependent Schrödinger equation	26
2.31. Runge-Gross theorem	27
2.32. Functional derivative of action integral	27
2.33. Time-dependent Kohn-Sham Equations	27
2.34. Time-dependent electron density	27
2.35. Time-dependent Kohn-Sham potential	27
2.36. Hartree term	27
2.37. Electron density at time t	28
2.38. Perturbation on electronic Hamiltonian	28
2.39. Hamiltonian correction	28
2.40. Time-dependent density	29
2.41. Transition densities	29
2.42. Expansion coefficients	29
2.43. Casida equations	29
2.44. Absorption spectra	30
2.45. Oscillation strengths	30
2.46. Transition dipole moments	30
3.1. Gaussian line-broadening	35
3.2. Oscillation strength	35

4.1. Surface energy value of $\gamma_{110}^{\text{bare}}$	85
4.2. Surface energy for the formation of 2D plate	85
4.3. Surface energy for the formation of 3D box	86
4.4. Surface energy for amines to attach on 100.....	86
4.5. Surface energy for the formation of 2D plate with amines.....	87
4.6. Adsorption energy of PbCl_2 in a 2D plate	88
4.7. Adsorption energy of PbCl_2 in a 3D box.....	88
4.8. Adsorption energy of amines in a 2D plate	88
4.9. Total surface energy of 2D plate.....	88
4.10. Total surface energy of 3D box	88
4.11. Total surface energy of 2D plate with amines	88

LIST OF ABBREVIATIONS

QD.....	Quantum dot
DFT.....	Density Functional Theory
TDDFT.....	Time dependent DFT
HK.....	Hohenberg and Kohn
KS	Kohn-Sham
LDA	Local Density Approximation
LSDA	Local-Spin Density Approximation
GGA.....	Generalized Gradient Approximation
VASP	Vienna Ab-initio Simulations Package

LIST OF SYMBOLS

ψ Wavefunction

ρ Density

Bold letters in equationsvector form

μ dipole moment

1. INTRODUCTION

1.1. Quantum Dots

Quantum dots (QDs) are semiconductor nanocrystalline particles that have a unique property known as exciton confinement, which allows one to tune their optical and electronic properties. These materials typically range in size from 1-10 nm where their energy levels are quantized rather than continuous as shown in Figure 1.1. It was for the first time, in 1982, Henglein reported that absorption spectra of colloidal CdS solution was blue shifted compared to that of bulk material.¹ A year later, Brus explained this effect while discovering their quantum mechanical nature.² Since then much progress was achieved in the synthesis of such nanoparticles with controlled size distributions. In 1993, Murray et. al. reported size selective synthesis of CdX (X = S, Se, Te) nanoparticles, which provided a platform for the detailed investigation of their photophysical properties and its applications.³

In the size regime of 1-10 nm, the macroscopic properties are dominated by quantum mechanical effects. Due to the presence of spatial restrictions in these nanoparticles, band gap is altered greatly. In other words, the energy difference between highest occupied molecular orbital (HOMO) and lowest unoccupied molecular orbital (LUMO) widens as the size decreases from bulk materials to QDs. This effect is known as quantum/size confinement.⁴ The famous quantum mechanical problem of “particle in a box” is the simplest example of this effect.

Unlike other fluorophores such as organic dyes and polymers, QDs exhibit broad absorption spectra; and narrow emission.⁵ They have high extinction coefficients and quantum yield, show high resistance to photo degradation and have long fluorescence lifetimes.⁶

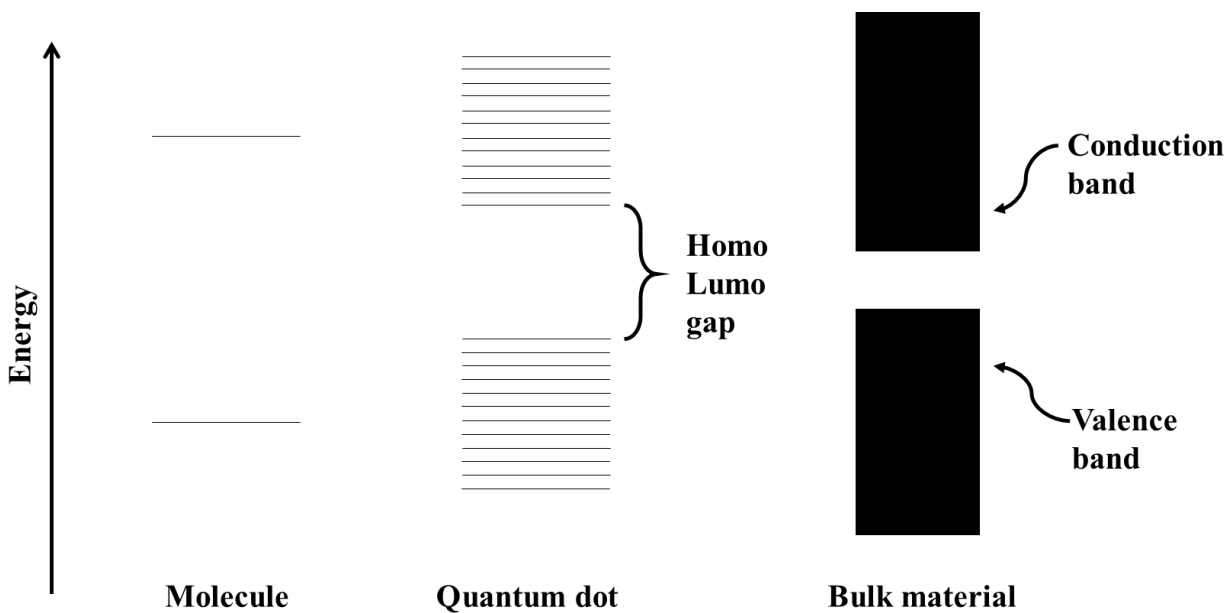


Figure 1.1. Energy levels band alignment

Due to presence of narrow emissive properties, discrete energy states and structural rigidity and tendency to facilitate charge carriers, QDs have drawn a special attention when compared to other well-known polymeric materials and organic dyes. Moreover, QDs have high extinction coefficients,⁶ broad absorption spectra,⁷ narrow emission,⁸ long fluorescence lifetime, high photostability, and can be easily functionalized.⁹

There are several factors that can affect exciton confinement and thus tuning their optical and electronic properties such as size,¹⁰ composition,¹¹ applied electric fields¹² and passivating ligands.¹³ Optoelectronic properties of QDs depend on their diameter: smaller the diameter, larger is their band gap, and hence their emitting wave length as shown in Figure 1.2.¹⁴ This allows these QDs to find their applications in various fields such as light emitting diodes (LEDs),¹⁵ solar cells,¹⁶ bioimaging,¹⁷ etc.

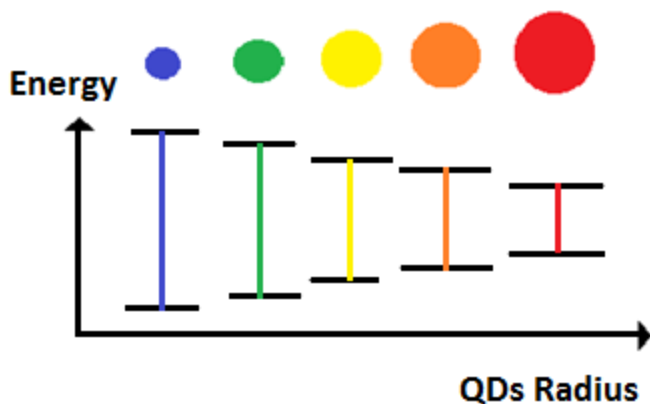


Figure 1.2. Effect of size confinement on emitting color

Composition of the QD plays an important role in its optoelectronic properties. A QD can be made of a single element or multiple elements. Some of the examples include Silicon,¹⁸ CdSe,¹⁹ CdTe,²⁰ PbSe,²¹ CdS,²² PbS,²³ and so on. Each of these QDs has its uniqueness that makes them interesting materials to study. Ligands passivated on the surface of QDs can greatly influence their electronic and optical properties.¹³ QDs are synthesized by colloidal method using different ligands such as amines, tri octyl phosphine oxide (TOPO), thiols and carboxylic acids to passivate on its surface. The main reasons for ligand passivation are to increase QDs solubility, decrease QD-QD interaction, remove dangling bonds and increase photoluminescence (PL) efficiency.²⁴ An external electric field plays a vital role in altering optical and electronic properties of QDs. This effect is known as quantum confined Stark effect (QCSE).²⁵ These methods especially used to find their applications in solar cells and LEDs.

1.2. Synthesis of QDs

QD cores are comprised of combination of II-VI periodic groups such as CdS, CdSe, ZnSe and CdTe, III-V groups such as InP, InAs, GaAs and IV-VI groups such as PbS, PbSe, PbTe, SnTe and other examples include silicon, graphene and carbon quantum dots. These materials emit wavelengths almost from UV to infrared. CdSe is the most commonly synthesized

QD which emits in visible region, leading to applications in fluorescence detectors.²⁶ Among many synthetic methods, colloidal synthesis has proven to be a cheap, quick, and efficient way to synthesize QDs. The production is carried out by quickly injecting precursors of cores into organic coordinating solvents (long chain alkyl amines, phosphines and phosphine oxides) at high temperatures.²⁷

Synthesized QDs are then purified using a solvent extraction process, where they are dispersed in non-polar solvents such as hexane and chloroform, and polar solvents are added to remove excess organic ligands. This process is very tricky and can cause the larger QDs to aggregate and then precipitate, while smaller QDs stay in the supernatant. To obtain QDs of desired size, the ratio of polar to non-polar solvents is altered. Although synthesizing QDs is easier, the purifying step may bring in structural disorders that can strongly affect their photophysical properties.²⁸ Moreover, other complex factors such as interfacial interactions and surface chemistry can greatly affect both, optical and electronic properties of QDs.²⁹

1.3. Effect of Surface Chemistry on Photophysics of Quantum Dots

Photophysics of QDs is extremely sensitive to their size, structure and surface. Presence of surface disorders in these single crystals can result in photobleaching (PL intensity degrades over time) and quantum blinking^{30,31} (emission light turn on and turn off irregularly, in other words: fluorescence intermittence); which create technical problems to their practical applications in biolabelling, optical sensors and solid state lighting). Atoms that comprise the core of QD are responsible for the main physical properties, whereas surface atoms usually tend to perturb these properties. The capped ligands on the surface satisfy the valency of surface atoms, thereby removing the dangling bonds, reduce the QD-QD interactions, enhance the solubility and suppress the chemical reactivity, thus strongly altering optical and electronic

properties.²⁴ Although ligands are advantageous, presence of imperfect ligands capping due to partial surface passivation or impurities, leads to the appearance of surface states and trap states near or inside the band gap, while affecting both radiative and non-radiative decay processes.^{32,33} Thus, surface chemistry of QDs plays a critical role in governing charge transfer and energy transfer processes between QD and QD or QD and ligand that define their efficiency in light harvesting and solar energy conversion to electric current. Nevertheless, there is still a limited research progress towards controlling this complex surface chemistry of QDs.²⁹ To explore these characteristics is experimentally difficult as the surface states appearing through the defects are dark; their transitions are optically inactive and hence cannot be observed. Some progress has been achieved through the help of scanning tunneling spectroscopy.³⁴ However, effects such as carrier multiplication, altering of charge transfers, energy transfers and PL due to ligands on QD are still poorly understood.³⁵ On the other hand, computations on atomistic level provide valuable insights in to these characteristics. My dissertation mainly focuses on computationally investigating the effect of surface passivation and their defects on photophysical properties of CdSe, PbSe and Si QDs.

1.4. Role of Computational Modeling

Theoretical/Computational approaches are helpful in understanding difficulties in the synthesis of QDS and in investigating their optoelectronic properties. Although experimental analytical techniques reveal salient features of synthesized QDs, thorough information of electronic structure properties in atomistic level and position of optically dark (forbidden) states is known mostly from quantum chemical approaches. Theoretical simulations have the potential to support experimental data, provide insights to the data and furnish information such as the

density of states and photophysical properties such as emission, absorption, electron transport, and decay processes which governs suggestions for designing novel nanomaterials.

The first step in these calculations is to obtain reasonable, yet experimentally relevant structures of the QDs in their ground state. There are many theoretical models ranging from low-accurate classical molecular mechanics (MM) force field method to moderately accurate Hartree-Fock (HF) and Density Functional Theory (DFT), to more accurate multi reference methods such as configuration interaction (CI) methods to serve this purpose. Each of these methods has their own applicability depending on the size of the system, that is, number of atoms present in the system.

MM approach can be used for exploring potential energy surfaces and obtain structures with minimal energies relying on force fields (FF) calculations. FF data is generally parameterized from experimental data or higher level quantum chemical calculations. The disadvantage with this method is that parameterization of FF for these complex systems is difficult as the morphology at the surface of QDs and their interfaces are difficult to predict.

These approaches are best to investigate mesoscopic properties but cannot provide description of electronic and optical properties of materials.³⁶ CI method is more accurate in determining the optoelectronic properties but require more number of computational resources such as long CPU time and large memory requirements, due to which this method is limited to only relatively small systems. A compromise is the moderately accurate DFT method is sufficiently enough to investigate electronic structure and optical properties of nanoparticles containing few 100s of atoms, such as the methods implemented in this work. Thus many researchers use DFT in their calculations as it as effective approximate method being able to describe the photophysical properties accurately enough.^{37,38} Unfortunately DFT is limited to a

maximum QD size of 2 nm, compared to the overall size regime of 2-10 nm. Recent synthetic routes developed were successful in producing QDs with 1-2 nm size range CdSe and PbSe,³⁹ making it possible for the direct comparison of DFT methods to experimental observations. Detailed description of various methodologies employed in this work is briefed in chapter 2.

1.5. Objectives and Outline

The main difficulty in the practical application of quantum dots is their sensitivity to surface chemistry. Although QDs have promising properties, they still lag in proving their efficiency compared to other known traditional technologies. The reason for this inefficiency is the uncontrolled interfacial charge transport associated by surface defects. Nevertheless, the question of how the surface defects affect the electronic structure and optical properties of QDs is still unanswered. The main goal of my dissertation is to investigate these issues by answering questions like, the reason for the appearance of surface states: is it due to the ligand choice, or due to the improper attachment of ligands or due to the presence of charge impurities? Secondly, my dissertation also addresses the issue on how, not just the interactions between QD and ligand, but between QD and QD will affect their electronic structure and photophysical properties.

The outline of my dissertation is organized as follows.

In chapter 2, a detailed description of theoretical methods employed in this dissertation is briefed.

In chapter 3, effect of ligand passivation on the electronic structure and optical properties of QDs is investigated. This chapter is also divided into two sub-chapters, namely 3.1 and 3.2. Chapter 3.1 describes the effect of thiols capping on the electronic structure and optical properties of CdSe QDs. Chapter 3.2 introduces the effect of surface oxidation of PbSe QDs on their optoelectronic properties.

In chapter 4, the effect of particles interactions on the optical and electronic properties of QDs are detailed. This chapter is sub-divided into two chapters 4.1 and 4.2. In chapter 4.1, the effect of charge and ligand defects on electronic structure and optical properties of interacting Silicon QDs is detailed. In chapter 4.2, insights into engineering of PbSe QDs interactions with each other and with the passivating ligands in the formation of 2D PbSe nanoplates are investigated.

1.6. References

- 1 Henglein, A. Photochemistry of Colloidal Cadmium-Sulfide .2. Effects of Adsorbed Methyl Viologen and of Colloidal Platinum. *J Phys Chem-US* **86**, 2291-2293, doi:Doi 10.1021/J100210a010 (1982).
- 2 Brus, L. E. A Simple-Model for the Ionization-Potential, Electron-Affinity, and Aqueous Redox Potentials of Small Semiconductor Crystallites. *J Chem Phys* **79**, 5566-5571, doi:Doi 10.1063/1.445676 (1983).
- 3 Murray, C. B., Norris, D. J. & Bawendi, M. G. Synthesis and Characterization of Nearly Monodisperse Cde (E = S, Se, Te) Semiconductor Nanocrystallites. *Journal of the American Chemical Society* **115**, 8706-8715, doi:Doi 10.1021/Ja00072a025 (1993).
- 4 Henglein, A. Mechanism of Reactions on Colloidal Microelectrodes and Size Quantization Effects. *Top Curr Chem* **143**, 113-180 (1988).
- 5 Chan, W. C. W. & Nie, S. M. Quantum dot bioconjugates for ultrasensitive nonisotopic detection. *Science* **281**, 2016-2018, doi:DOI 10.1126/science.281.5385.2016 (1998).
- 6 Doose, S., Tsay, J. M., Pinaud, F. & Weiss, S. Comparison of photophysical and colloidal properties of biocompatible semiconductor nanocrystals using fluorescence correlation spectroscopy. *Analytical chemistry* **77**, 2235-2242, doi:10.1021/ac050035n (2005).

- 7 Alivisatos, A. P. Semiconductor clusters, nanocrystals, and quantum dots. *Science* **271**, 933-937, doi:DOI 10.1126/science.271.5251.933 (1996).
- 8 Somers, R. C., Bawendi, M. G. & Nocera, D. G. CdSe nanocrystal based chem-/bio-sensors. *Chem Soc Rev* **36**, 579-591, doi:10.1039/b517613c (2007).
- 9 Karakoti, A. S., Shukla, R., Shanker, R. & Singh, S. Surface functionalization of quantum dots for biological applications. *Adv Colloid Interfac* **215**, 28-45, doi:10.1016/j.cis.2014.11.004 (2015).
- 10 Han, H., Di Francesco, G. & Maye, M. M. Size Control and Photophysical Properties of Quantum Dots Prepared via a Novel Tunable Hydrothermal Route. *J Phys Chem C* **114**, 19270-19277, doi:10.1021/jp107702b (2010).
- 11 Schliwa, A., Winkelkemper, M. & Bimberg, D. Impact of size, shape, and composition on piezoelectric effects and electronic properties of In(Ga)As/GaAs quantum dots. *Physical Review B* **76**, doi:Artn 205324 10.1103/Physrevb.76.205324 (2007).
- 12 Teubert, J. *et al.* InGaN/GaN quantum dots as optical probes for the electric field at the GaN/electrolyte interface. *J Appl Phys* **114**, doi:Artn 074313 10.1063/1.4818624 (2013).
- 13 Green, M. The nature of quantum dot capping ligands. *Journal of Materials Chemistry* **20**, 5797-5809, doi:10.1039/c0jm00007h (2010).
- 14 Parak, W. J., Manna, L., Simmel, F. C., Gerion, D. & Alivisatos, P. in *Nanoparticles* 4-49 (Wiley-VCH Verlag GmbH & Co. KGaA, 2005).
- 15 Shea-Rohwer, L. E., Martin, J. E., Cai, X. C. & Kelley, D. F. Red-Emitting Quantum Dots for Solid-State Lighting. *Ecs J Solid State Sc* **2**, R3112-R3118, doi:10.1149/2.015302jss (2013).

- 16 Plass, R., Pelet, S., Krueger, J., Gratzel, M. & Bach, U. Quantum dot sensitization of organic-inorganic hybrid solar cells. *J Phys Chem B* **106**, 7578-7580, doi:10.1021/jp020453l (2002).
- 17 Erathodiyil, N. & Ying, J. Y. Functionalization of Inorganic Nanoparticles for Bioimaging Applications. *Accounts Chem Res* **44**, 925-935, doi:10.1021/ar2000327 (2011).
- 18 Bley, R. A., Kauzlarich, S. M., Davis, J. E. & Lee, H. W. H. Characterization of silicon nanoparticles prepared from porous silicon. *Chem Mater* **8**, 1881-1888, doi:Doi 10.1021/Cm950608k (1996).
- 19 Peng, X. G. *et al.* Shape control of CdSe nanocrystals. *Nature* **404**, 59-61 (2000).
- 20 Aldeek, F., Balan, L., Lambert, J. & Schneider, R. The influence of capping thioalkyl acid on the growth and photoluminescence efficiency of CdTe and CdSe quantum dots. *Nanotechnology* **19**, doi:Artn 475401 10.1088/0957-4484/19/47/475401 (2008).
- 21 Yong, K. T. *et al.* Shape control of PbSe nanocrystals using noble metal seed particles. *Nano Letters* **6**, 709-714, doi:10.1021/nl052472n (2006).
- 22 Sun, W. T. *et al.* CdS quantum dots sensitized TiO₂ nanotube-array photoelectrodes. *Journal of the American Chemical Society* **130**, 1124-+, doi:10.1021/ja0777741 (2008).
- 23 Joo, J. *et al.* Generalized and facile synthesis of semiconducting metal sulfide nanocrystals. *Journal of the American Chemical Society* **125**, 11100-11105, doi:10.1021/ja0357902 (2003).
- 24 Kilina, S., Kilin, D. & Tretiak, S. Light-Driven and Phonon-Assisted Dynamics in Organic and Semiconductor Nanostructures. *Chem Rev* **115**, 5929-5978, doi:10.1021/acs.chemrev.5b00012 (2015).

- 25 Miller, D. A. B. *et al.* Band-Edge Electroabsorption in Quantum Well Structures - the Quantum-Confined Stark-Effect. *Physical review letters* **53**, 2173-2176, doi:DOI 10.1103/PhysRevLett.53.2173 (1984).
- 26 Medintz, I. L., Uyeda, H. T., Goldman, E. R. & Mattoussi, H. Quantum dot bioconjugates for imaging, labelling and sensing. *Nat Mater* **4**, 435-446, doi:10.1038/nmat1390 (2005).
- 27 Murray, C. B., Kagan, C. R. & Bawendi, M. G. Synthesis and characterization of monodisperse nanocrystals and close-packed nanocrystal assemblies. *Annu Rev Mater Sci* **30**, 545-610, doi:DOI 10.1146/annurev.matsci.30.1.545 (2000).
- 28 Qu, L. H. & Peng, X. G. Control of photoluminescence properties of CdSe nanocrystals in growth. *Journal of the American Chemical Society* **124**, 2049-2055, doi:10.1021/ja017002j (2002).
- 29 Kilina, S. V., Tamukong, P. K. & Kilin, D. S. Surface Chemistry of Semiconducting Quantum Dots: Theoretical Perspectives. *Acc Chem Res* **49**, 2127-2135, doi:10.1021/acs.accounts.6b00196 (2016).
- 30 Kuno, M., Fromm, D. P., Hamann, H. F., Gallagher, A. & Nesbitt, D. J. Nonexponential "blinking" kinetics of single CdSe quantum dots: A universal power law behavior. *J Chem Phys* **112**, 3117-3120, doi:Doi 10.1063/1.480896 (2000).
- 31 Neuhauser, R. G., Shimizu, K. T., Woo, W. K., Empedocles, S. A. & Bawendi, M. G. Correlation between fluorescence intermittency and spectral diffusion in single semiconductor quantum dots. *Physical review letters* **85**, 3301-3304, doi:DOI 10.1103/PhysRevLett.85.3301 (2000).

- 32 Miller, J. B. *et al.* Enhanced Luminescent Stability through Particle Interactions in Silicon Nanocrystal Aggregates. *Acs Nano* **9**, 9772-9782, doi:10.1021/acsnano.5b02676 (2015).
- 33 Cooney, R. R., Sewall, S. L., Anderson, K. E. H., Dias, E. A. & Kambhampati, P. Breaking the phonon bottleneck for holes in semiconductor quantum dots. *Physical review letters* **98**, doi:Artn 177403 10.1103/Physrevlett.98.177403 (2007).
- 34 Gervasi, C. F. *et al.* Diversity of sub-bandgap states in lead-sulfide nanocrystals: real-space spectroscopy and mapping at the atomic-scale. *Nanoscale* **7**, 19732-19742, doi:10.1039/c5nr05236j (2015).
- 35 Peterson, M. D. *et al.* The Role of Ligands in Determining the Exciton Relaxation Dynamics in Semiconductor Quantum Dots. *Annu Rev Phys Chem* **65**, 317-339, doi:10.1146/annurev-physchem-040513-103649 (2014).
- 36 Hornak, V. *et al.* Comparison of multiple amber force fields and development of improved protein backbone parameters. *Proteins* **65**, 712-725, doi:10.1002/prot.21123 (2006).
- 37 Nguyen, K. A., Day, P. N. & Pachter, R. Understanding Structural and Optical Properties of Nanoscale CdSe Magic-Size Quantum Dots: Insight from Computational Prediction. *J Phys Chem C* **114**, 16197-16209, doi:10.1021/jp103763d (2010).
- 38 Tamukong, P. K., Peiris, W. D. & Kilina, S. Computational insights into CdSe quantum dots' interactions with acetate ligands. *Physical chemistry chemical physics : PCCP* **18**, 20499-20510, doi:10.1039/c6cp01665k (2016).

- 39 Dolai, S. *et al.* Isolation of Bright Blue Light-Emitting CdSe Nanocrystals with 6.5 kDa Core in Gram Scale: High Photoluminescence Efficiency Controlled by Surface Ligand Chemistry. *Chem Mater* **26**, 1278-1285, doi:10.1021/cm403950f (2014).

2. THEORETICAL FRAMEWORK

In this dissertation, we performed theoretical calculations to investigate the electronic and optical properties of semiconductor nanomaterials. We have investigated a variety of nanomaterials including 0D materials such as quantum dots (QDs) and 2D nanoplatelets. These materials have potential to be used as solar cells and photovoltaic devices depending on their band gap and PL efficiency. Thus, engineering the band gap is essential to increase the efficiency of these materials to find their applications in solar cells. Moreover, the band gap depends on various factors such as ligands, solvent, defects, etc. With the aid of computational materials design and simulations, one can study the effect of such factors on the electronic and optical properties of these materials. In this dissertation, we utilized DFT methods to study ground state electronic properties of QDs. For studying the optical properties, we used Time Dependent DFT (TDDFT) approach. In this chapter, the fundamental concepts of various theoretical approaches were discussed.

2.1. Introduction to Quantum Mechanical Calculations

The purpose of using quantum mechanics or theoretical approach is to investigate the properties of semiconductor nanomaterials and to understand/overcome any problems that may occur in the process of their synthesis. Through experimental analytical techniques, one can easily determine the properties of bulk and crystal structures. However, knowing in detail, the atomic structure properties is extracted largely from theoretical approaches. There are several theoretical approaches for studying atomic structures, ranging from highly accurate methods such as CI and coupled cluster methods to somewhat moderately accurate HF and DFT based methods to less accurate classical methods such as molecular mechanics force fields approach. Every method has its own importance based on the size of the system and type of property study.

To describe electronic properties of materials, like in this work, DFT methods are commonly used. To investigate mesoscopic properties such as surface roughening is usually dealt using classical potentials like that in molecular mechanics.

2.1.1. The Many-body Problem

For a system containing N number of electrons and M number of nuclei, their properties can be dealt by solving Schrödinger equation:

$$\hat{H}\psi(\mathbf{r}_1, \mathbf{r}_2, \dots, \mathbf{r}_N, \mathbf{R}_1, \mathbf{R}_2, \dots, \mathbf{R}_M) = E\psi(\mathbf{r}_1, \mathbf{r}_2, \dots, \mathbf{r}_N, \mathbf{R}_1, \mathbf{R}_2, \dots, \mathbf{R}_M) \quad (2.1)$$

Here \hat{H} is the Hamiltonian operator, ψ is the wavefunction, r_N denotes coordinates of the electrons and R_M denotes the coordinates of nuclei.

Hamiltonian operator H is given as:

$$\begin{aligned} \hat{H} &= -\frac{\hbar^2}{2} \sum_{i=1}^N \frac{\nabla_k^2}{m_e} + \frac{1}{2} \sum_{i \neq j}^N \frac{e^2}{|r_i - r_j|} - \frac{\hbar^2}{2} \sum_{k=1}^M \frac{\nabla_k^2}{M_k} + \frac{1}{2} \sum_{k \neq l}^M \frac{Z_k Z_l e^2}{|R_k - R_l|} - \sum_{i,k}^{N,M} \frac{Z_k e^2}{|r_i - R_k|} \\ &= \hat{T}^e + \hat{V}^{ee} + \hat{T}^N + \hat{V}^{NN} + \hat{V}^{Ne}. \end{aligned} \quad (2.2)$$

Here $\hbar = \frac{h}{2\pi}$ is Plank constant, Z is the nuclear charge, M_k and m_e are the masses of nuclei and electron respectively, \hat{T}^e is the kinetic energy of electrons, \hat{V}^{ee} is the potential energy, \hat{T}^N is the kinetic energy of nucleus, \hat{V}^{NN} is the nuclei-nuclei interactions term and \hat{V}^{Ne} is the electron-nuclei's interactions term.

Solving Eq. (2.3) gives an exact solution only for Hydrogen atom. However, to solve even for a helium atom, various approximations are needed to arrive at a close-form solution. Thus, for the systems of our interest, such as QDs, which is having a complex many-body problem, requires more approximations for solving Eq. (2.3).

Born-Oppenheimer approximation assumes that the motion of nuclei and electrons can be separable, since nuclei are heavier than electrons in terms of mass, and that electron can relax

rapidly to ground state configuration. Thus, in solving the time independent Schrödinger obtained from Eq. (2.3), nuclei coordinates can be assumed stationary. Hence total wavefunction can be obtained from the product of electronic wavefunction and nuclei wavefunction. Therefore Eq. (2.2) can be reduced to Eq. (2.3) to solve for electronic Hamiltonian.

$$\hat{H}_e = -\frac{\hbar^2}{2} \sum_{i=1}^N \frac{\nabla_k^2}{m_e} + \frac{1}{2} \sum_{i \neq j}^N \frac{e^2}{|r_i - r_j|} - \sum_{i,k}^{N,M} \frac{Z_k e^2}{|r_i - R_k|} = \hat{T}^e + \hat{V}^{ee} + \hat{V}^{Ne} \quad (2.3)$$

Eq. (2.3) can be further broken down to Eq. (2.4) that has internal and external terms in the equation. Here coordinates of nuclei are fixed, hence the notation R_0 .

$$\hat{H}_e = \hat{T}^e(\mathbf{r}) + V_{int}(\mathbf{r}) + \hat{V}_{ext}(\mathbf{r}; \mathbf{R}_0) \quad (2.4)$$

Although the overall complexity of the problem has been simplified, it is still problematic to solve for an exact solution due to the difficulties in finding exact electron-electron interaction (second term in Eq. (2.4)).

Hartree and Fock (Reference) proposed a solution to many-body equation by expanding wavefunction in the form of Slater determinants as shown in Eq. (2.5)

$$\Phi = \frac{1}{\sqrt{N!}} \begin{vmatrix} \phi_1(\vec{x}_1) & \phi_2(\vec{x}_1) & \dots & \phi_N(\vec{x}_1) \\ \phi_1(\vec{x}_2) & \phi_2(\vec{x}_2) & \dots & \phi_N(\vec{x}_2) \\ \vdots & \vdots & \ddots & \vdots \\ \phi_1(\vec{x}_N) & \phi_2(\vec{x}_N) & \dots & \phi_N(\vec{x}_N) \end{vmatrix} \quad (2.5)$$

Problem with this method is that it completely neglected the electron correlations, which gave large deviations to experimental results. To solve many body problem, there emerges DFT, which provides a mapping of many-body problem to a single-body problem.

The central idea behind DFT is that it replaces the ground state electronic wavefunction ψ_0 variable with ground state electron density n_0 as shown in Eq. (2.6).

$$n_0(\mathbf{r}) = \iint \dots \int |\psi_0(\mathbf{r}, \mathbf{r}_2, \dots, \mathbf{r}_N)|^2 dr_2 dr_3 \dots dr_N \quad (2.6)$$

Its origin arises from the two famous theorems proposed by Hohenberg and Kohn.

2.1.2. The Hohenberg and Kohn Theorems

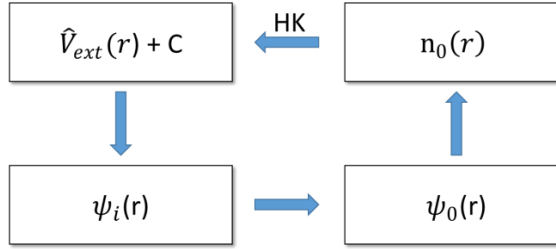


Figure 2.1. Schematic diagram of HK Theorem

In 1964, Hohenberg and Kohn laid the origin for all the modern DFT based methodologies. In their seminal paper,¹ they proposed two theorems; Hohenberg and Kohn (HK) theorem 1 and theorem 2.

2.1.2.1. HK Theorem 1

The ground state density $n_0(\mathbf{r})$ of a many-electron system uniquely determines the many-body wave function $\psi_0(\mathbf{r})$ and the potential $\hat{V}_{ext}(\mathbf{r})$. According to this theorem, if we determine exact ground state density, then we can uniquely find other properties of many-electron system.

2.1.2.2. HK Theorem 2

A universal functional for the energy ‘ $E[n(\mathbf{r})]$ ’ can be defined in terms of the density ‘ $n(\mathbf{r})$ ’ as shown in Eq. (2.7), where F_{HK} term includes the kinetic energy of electrons and electron-electron interactions. The exact ground state of the system is the global minimum value of this functional and the density that performs functional minimization is the exact ground state density, $n_0(\mathbf{r})$.

$$E[n(\mathbf{r})] = F_{HK}[n(\mathbf{r})] + \int dr \hat{V}_{ext}(\mathbf{r})n(\mathbf{r}) \quad (2.7)$$

Although HK theorems prove their statements, it tells nothing about the form of the exact functional. It considers the case with non-degenerate ground state energies, however did not incorporate degenerate ground states. Later, Levy² and Lieb³ extended the work by including degenerate ground states into the realm of DFT.

2.1.3. The Kohn-Sham Method

The Kohn-Sham (KS) method states that the interacting many-body system can be replaced by a non-interacting one particle system. According to KS approach, the total energy functional, also known as Kohn-Sham functional can be written as shown in Eq. 2.8.

$$E[n(\mathbf{r})] = T[n(\mathbf{r})] + \int d\mathbf{r} \hat{V}_{ext}(\mathbf{r})n(\mathbf{r}) + \frac{1}{2} \iint \frac{n(\mathbf{r})n(\mathbf{r}')}{|\mathbf{r} - \mathbf{r}'|} d\mathbf{r}' d\mathbf{r} + E_{xc}[n(\mathbf{r})] \quad (2.8)$$

Here the third term is the Coulomb integral potential (Hartree term) and the fourth term is exchange-correlation functional. According to the HK theorem 2, minimization of KS functional by density $n(\mathbf{r})$ using variational principle, gives one-particle KS equations.

$$\left(\frac{-\hbar^2}{2m_e} \nabla^2 + V_{KS} \right) \varphi_i(\mathbf{r}) = \varepsilon_i \varphi_i(\mathbf{r}) \quad (2.9)$$

Here $\varphi_i(\mathbf{r})$ are the KS orbitals, ε_i are the eigenvalues and V_{KS} is the KS potential,

$$V_{KS} = V_{ext} + \int \frac{n(\mathbf{r}')}{|\mathbf{r} - \mathbf{r}'|} d\mathbf{r}' + V_{xc} \quad (2.10)$$

Here V_{xc} is the exchange-correlation potential defined as:

$$V_{xc} = \frac{\delta E_{xc}[n]}{\delta n(\mathbf{r})} \quad (2.11)$$

2.1.4. The Exchange Correlation Functional

The fourth term in Eq. 2.8 is difficult to evaluate exactly and hence is approximated by approximations such as local-density approximation (LDA), local-spin density approximation (LSDA), generalized gradient approximation (GGA) and meta-GGA. Perdew and Schmidt have

proposed “Jacob’s ladder” that categorizes existing exchange-correlation approximations as shown in Fig 1.2.⁴ In this figure, $n(\mathbf{r})$ refers electron density, $\nabla n(\mathbf{r})$ refers to gradient of electron density, $\tau(\mathbf{r})$ refers to kinetic energy density and $\nabla^2 n(\mathbf{r})$ refers to the second derivative of the electron density. In the following subsections, these approximations will be briefly discussed.

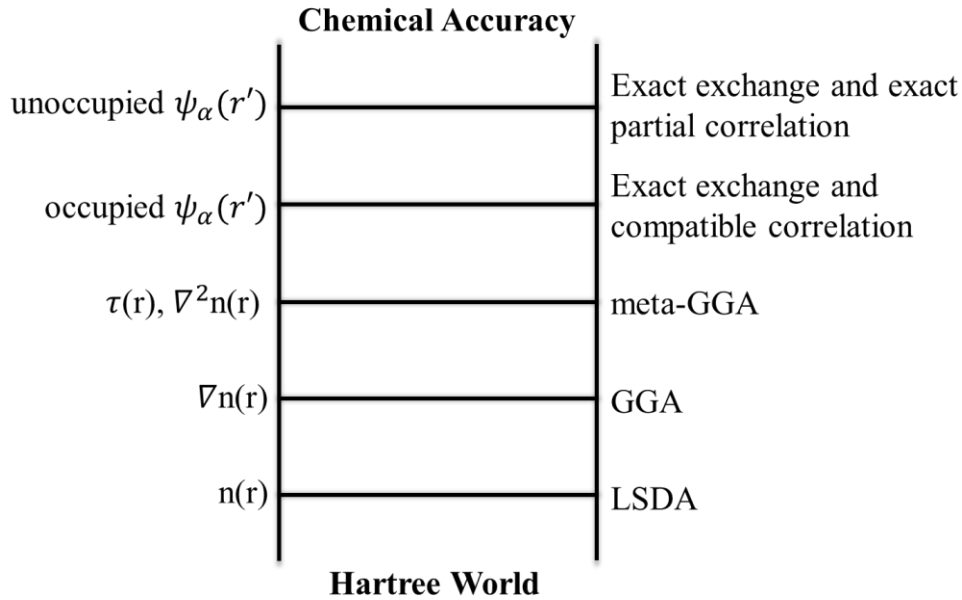


Figure 2.2. Schematic diagram of Jacob’s Ladder

2.1.4.1. Local Density Approximation (LDA)

In this approximation, one assumes that the electrons sit in an infinite region of space, with uniform positive external potential, chosen to preserve overall neutrality charge. This approximation evaluates kinetic and exchange energies through Slater determinants of plane waves. Correlation energy is evaluated using Monte Carlo calculations.

$$E_{xc}^{LDA}[n(\mathbf{r})] = \int d\mathbf{r} n(\mathbf{r}) \epsilon_{xc}^{hom}[n(\mathbf{r})] \quad (2.12)$$

Here $\epsilon_{xc}^{hom}[n(\mathbf{r})]$ is the exchange-correlation energy density of homogeneous uniform electron gas. LDA can be valid only to slow varying density systems. Surprisingly, calculations

of atoms, molecules and solids show that it works well for these systems. However, LDA overestimates cohesive energies and underestimates lattice constants for metals and insulators.

2.1.4.2. Generalized Gradient Approximation (GGA)

In this approximation, density gradient is included in addition to the approximations of LDA. GGA functional can be represented as follows

$$E_{xc}^{GGA}[n(\mathbf{r})] = \int d\mathbf{r} n(\mathbf{r}) \epsilon_{xc} [n(\mathbf{r}), |\nabla n(\mathbf{r})|] = \int d\mathbf{r} n(\mathbf{r}) \epsilon_{xc}^{hom} F_{xc} [n(\mathbf{r}), |\nabla n(\mathbf{r})|] \quad (2.13)$$

Here ϵ_{xc}^{hom} is the exchange energy of homogeneous uniform electron gas and F_{xc} is functional of the density $n(\mathbf{r})$ and the gradient of density $\nabla n(\mathbf{r})$. Examples of GGA include B88, PW91 and PBE. Due to the inclusion of gradient of density $\nabla n(\mathbf{r})$ term, GGA functionals result in improved agreement with the experimental data compared to LDA, for properties of molecules and solids such as structural features and ground state energies.

2.1.4.3. meta-GGA

These are considered as third generation functionals in Jacob's ladder. In this approximation, second derivative of the density $\nabla^2 n(\mathbf{r})$ along with kinetic energy density τ_σ were included in the exchange-correlation potential. Examples of the functionals that fall under this type are TPSS, revTPSS and AM06-L. These functionals result in better agreement with experiment for properties such as lattice constants and surface energies.

2.1.4.4. Hybrid Functionals

Hybrid exchange correlation functionals development is considered to be another milestone, whose central idea was formulated by Becke, who introduced a certain amount of exact exchange energy into the exchange-correlation functional term.

$$E_{xc}[n(\mathbf{r})] = cE_x^{exact}[n(\mathbf{r})] + (1 - c)E_x^{GGA}[n(\mathbf{r})] + E_c^{GGA}[n(\mathbf{r})] \quad (2.14)$$

Here $E_x^{GGA}[n(\mathbf{r})]$ and $E_c^{GGA}[n(\mathbf{r})]$ are the exchange and correlation density functionals respectively computed using GGA functional and c is a weighing coefficient. The exact exchange energy term is exchange energy of the Slater determinant containing KS spin orbitals.

$$E_x^{exact}[n(\mathbf{r})] = -\frac{1}{2} \sum_{i=1}^N \sum_{j=1}^N K_{ij} = -\frac{1}{2} \sum_{i=1}^N \sum_{j=1}^N \langle ij|ji \rangle \quad (2.15)$$

Becke introduced the exchange correlation in the following form:

$$E_{xc}[n(\mathbf{r})] = E_{xc}^{LSDA}[n(\mathbf{r})] + a_0(E_x^{exact}[n(\mathbf{r})] - E_x^{LSDA}[n(\mathbf{r})]) + a_x \Delta E_x^{B88}[n(\mathbf{r})] + a_c \Delta E_c^{PW91}[n(\mathbf{r})] \quad (2.16)$$

Here $E_{xc}^{LSDA}[n(\mathbf{r})]$ and $E_x^{LSDA}[n(\mathbf{r})]$ are LSDA exchange-correlation functional energy and LSDA exchange energy respectively. $\Delta E_x^{B88}[n(\mathbf{r})]$ is the correction to exchange energy introduced by Becke and $\Delta E_c^{PW91}[n(\mathbf{r})]$ is the correction to the correlation energy due to Perdew and Wang. The coefficients a_0 , a_x and a_c were obtained through least-square fits to experimental data. The resulting functional is known to be as B3PW91, the number 3 representing three semiempirical coefficients. After Becke's pioneering studies, many other hybrid functionals have been developed, among which are, B3LYP, PBE1PBE, HSE, M06-L and many more. Other functionals include long range corrections such as CAM-B3LYP and dispersion correction functionals such as B97XD. Among these, PBE1PBE, which is a mix of PBE exchange energy and HF exchange energy is 3:1 ratio, along with the full PBE correlation energy, is shown to be somewhat accurate and in better agreement with the experiments, especially in calculating the band gaps and excitation energies. Thus, in our work, we have mostly employed PBE1PBE functional to perform computations, whose formulation is shown below.

$$E_{xc}^{PBE0} = \frac{1}{4} E_{xc}^{HF} + \frac{3}{4} E_x^{PBE} + E_c^{PBE} \quad (2.17)$$

2.1.5. The Basis Sets

The solution to Kohn-Sham Eq. (2.9) involves determining corresponding eigenvectors and eigenvalues. In this process, eigenvectors are expanded in terms of functions of some known properties, where ensemble of such functions forms a basis.

$$\psi_i(\mathbf{r}) = \sum_k c_{ik} f_k(\mathbf{r}) \quad (2.18)$$

The basis can be chosen in many ways, each of these ways have its own advantages and disadvantages. However, there is a certain criterion for choosing a basis, they are: efficiency, accuracy, asymptotic completeness, complexity of computations, easy implementation, physical interpretation and relevance to the problem. There are three main classifications in which existing methods fall, whose importance and applicability is briefed as follows.

2.1.5.1. Localized Basis Sets

In case of isolated solids and molecules, the wavefunction decays exponentially to zero are larger distances, and hence the chosen basis functions should obey this likewise. Atomic orbitals fall in this type which is of two kinds: Slater type orbitals (STOs) and Gaussian type orbitals (GTOs).

STOs are represented as follows:

$$\phi_{STO}^{n,l,m,\zeta}(r, \theta, \phi) = \alpha Y_{lm}(\theta, \phi) r^{(n-1)} e^{-\zeta r} \quad (2.19)$$

Here α is normalization constant, $Y_{lm}(\theta, \phi)$ is spherical harmonic, l , m and n are quantum numbers, ζ is the radius of the orbit. Exponential dependency of r is same as for hydrogen atom.

GTOs are represented as follows:

$$\phi_{GTO}^{n,l,m,\zeta}(r, \theta, \phi) = \alpha Y_{lm}(\theta, \phi) r^{(2n-2-l)} e^{-\zeta r^2} \quad (2.20)$$

The main difference between GTOs and STOs is the power of \mathbf{r} . GTOs fall rapidly with distance compared to that of STOs. STOs are accurate but GTOs are computationally efficient. GTOs to reach same accuracy as STOs, needs at least three GTOs per basis set. In this category are the examples that include, 3-21G, 6-31G*, etc. There are basis sets that include polarization and diffusion functions to improve the accuracy. In our work, we have mostly used 6-31G* basis set for smaller atoms: C, H, N, O, Cl, I and S, which is a valence double-zeta polarized bass set that adds to the six d-type Cartesian-Gaussian polarization functions on each of the atoms, as implemented in Gaussian Software package.

2.1.5.2. Plane Waves and Grids

For periodic systems, the potential has the property that:

$$V(\mathbf{r} + n\mathbf{a}) = V(\mathbf{r}) \quad (2.21)$$

Here \mathbf{a} is a lattice vector and n is an integer. Using the Bloch's theorem, the wavefunction can be written as a product of periodic cell part and a wavelike part

$$\psi_i(\mathbf{r}) = e^{i\mathbf{k}\cdot\mathbf{r}} f_i(\mathbf{r}) \quad (2.22)$$

Due to its periodicity, $f_i(\mathbf{r})$ can be expanded as a set of plane waves.

$$f_i(\mathbf{r}) = \sum_G c_i(G) e^{i\mathbf{G}\cdot\mathbf{r}} \quad (2.23)$$

Here G are reciprocal lattice vectors, and the electronic wavefunction can be written as

$$\psi_i(\mathbf{r}) = \sum_G c_i(G) e^{i(\mathbf{k}+\mathbf{G})\cdot\mathbf{r}} \quad (2.24)$$

Like the method in localized basis sets, infinite number of basis function will be required to build an exact real wavefunction. The largest wave vector in the expansion of Eq. (2.23) controls the number of wavefunctions. Instead, a cut-off is imposed on the kinetic energy, whose value with wave vector \mathbf{k} is given by

$$E_k = \frac{\hbar^2 |\mathbf{k}|^2}{2m} \quad (2.25)$$

Plane wave basis set can be applied to isolated molecules as well, where the molecule is placed at the center of the cell with vacuum surrounded. The *ab initio* work used this dissertation used plane wave basis sets implemented in Vienna *ab initio* simulation package (VASP) code.⁵

2.1.6. Pseudopotentials

A typical solid state molecule contains two types of electrons: core electrons and valence electrons. Core electron describes the localized wavefunctions tightly bound to the nuclei, for which localized basis sets can be used. However, valence electrons are responsible for the atomic bonds, and impact the materials properties. Thus, an idea of excluding core electrons from the calculations for basis sets is to construct effective pseudopotentials. In this procedure, all electron wavefunctions are replaced by pseudo wavefunctions identical to electronic wavefunctions outside the core region. The most general form of pseudopotentials is

$$V_{pp} = \sum_{l,m} Y_{l,m}(\theta, \phi) V_l(r) Y_{l,m}^*(\theta, \phi) \quad (2.26)$$

Here $V_l(r)$ is the pseudopotential for the l^{th} angular momentum component. An example of basis set that has the pseudopotential is LANL2Dz, which is used in this dissertation, where ever heavy atoms were computed, examples include Pb, Se, and Cd.

2.2. Computational Methodology

In this dissertation, two different software packages were used: Gaussian 09⁶ and VASP, to perform DFT, depending on the need and purpose. Gaussian software was used to study single crystalline solids and VASP was particularly used in need to build periodic boundaries. Using both these codes, we performed structural optimizations to obtain zero-point energy structures

that were then used for further investigations on property studies. These include investigation of electronic structure and optical properties (obtaining absorption spectra)

2.3. Electronic Structure

After obtaining the optimized structures, one can determine the molecular orbital energies of the systems and thus compute the band gap by determining the difference between energies of highest occupied molecular orbital (HOMO) and lowest unoccupied molecular orbital (LUMO).

2.3.1. Density of States

Density of States (DOS) was computed employing Gaussian line-broadening as follows:

$$A(\omega) = \frac{1}{\sigma\sqrt{2\pi}} \sum_n h_n \exp\left(-\frac{(\omega_n - \omega)^2}{\sigma^2}\right) \quad (2.27)$$

Here h_n is transition strength, ω_n is the transition energy and σ is the spectral line width, whose definitions vary with type of calculations we perform. For plotting DOS, $\omega_n = \varepsilon_k$, where ε_k is the ground state molecular orbital energy. For evaluating total DOS, $h_n = 1$, whereas for the fragmented DOS, it is evaluated as the fraction of orbital localized on a specific fragment, as computed in Gaussian 09.⁶

2.4. Optical Properties

To calculate the absorption spectra and to investigate the optical properties on the systems of our interest, we need to perform computations using methods that consider the time dependency of the potential and hence electron density, an extension to DFT, known to be as TDDFT. The ground basis for TDDFT is the Runge-Gross theorem and quantum mechanical action.

2.4.1. The Runge-Gross Theorem

Runge and Gross generalized the HK theorem I to the time-dependent case.⁷ The Runge-Gross theorem states that when a many-electron system evolving from a fixed initial density is

subjected to either of two time-dependent external potentials, $v_1(\mathbf{r}, t)$ and $v_2(\mathbf{r}, t)$, that differ by more than an additive time-dependent term $c(t)$, they cannot produce the same time-dependent electron density.

$$v_1(\mathbf{r}, t) \neq v_2(\mathbf{r}, t) + c(t) \Leftrightarrow \rho_1(\mathbf{r}, t) \neq \rho_2(\mathbf{r}, t) \quad (2.28)$$

Using this theorem, the time-dependent potential can be calculated from the time-dependent electron density. From the obtained time-dependent potential, we can solve the time-dependent Schrödinger equation to obtain time-dependent wavefunction.

2.4.2. The Quantum Mechanical Action

Another principle that is required in constructing TDDFT is variational principle, which is analogous to HK theorem II. In the regime of time-dependency, this theorem states that there exists a functional $E_v^{HK}[\rho]$ of the electron density which, for a given external potential and number of electrons, takes the value of the ground state energy E_0 if the electron density ρ is the ground state electron density ρ_0 , and the higher values for any other electron density. The ground state electron density can be obtained by minimizing the value of $E_v^{HK}[\rho]$.

For the conservation of total energy in time, a quantity which is conserved for any correct time-dependent wavefunction is consider, that is, the action integral as follows:

$$\mathcal{A}[\Psi] = \int_{t_0}^{t_1} \left\langle \Psi(\mathbf{r}, t) \left| i \frac{\partial}{\partial t} - \hat{H}(\mathbf{r}, t) \right| \Psi(\mathbf{r}, t) \right\rangle dt \quad (2.29)$$

Now by comparing the action integral to the time-dependent Schrödinger Eq. (2.30), we notice that for a wavefunction to be the solution of Schrödinger equation, $\mathcal{A}[\Psi]$ must be zero.

$$\hat{H}(\mathbf{r}, t)\Psi(\mathbf{r}, t) = i \frac{\partial}{\partial t} \Psi(\mathbf{r}, t) \quad (2.30)$$

Based on Runge-Gross theorem, the action integral can be expressed also as a function of the exact electron density.

$$\mathcal{A}[\rho] = \int_{t_0}^{t_1} \left\langle \Psi[\rho](\mathbf{r}, t) \left| i \frac{\partial}{\partial t} - \hat{H}(\mathbf{r}, t) \right| \Psi[\rho](\mathbf{r}, t) \right\rangle dt \quad (2.31)$$

Also, the functional derivative of \mathcal{A} with respect to $\rho(\mathbf{r}, t)$ is zero for an exact time-dependent electron density $\rho(\mathbf{r}, t)$.

$$\frac{\delta \mathcal{A}}{\delta \rho(\mathbf{r}, t)} = 0 \quad (2.32)$$

2.4.3. The Time-dependent Kohn-Sham Equations

Based on the above theorems and principles, Runge and Gross then extended the case to time-dependent Kohn-Sham approach. Within the time dependency, Kohn-Sham spin orbitals can be expressed by Kohn-Sham equations, as follows.

$$\left[-\frac{1}{2} \nabla^2 + v_0(\mathbf{r}, t) \right] \phi_k(\mathbf{r}, t) = i \frac{\partial}{\partial t} \phi_k(\mathbf{r}, t) \quad (2.33)$$

The time dependent electron density is equal to the sum of the square of the Kohn-Sham spin orbitals ϕ_k :

$$\rho(\mathbf{r}, t) = \sum_{k=1}^N |\phi_k(\mathbf{r}, t)|^2 \quad (2.34)$$

Like in the time-independent case, time-dependent Kohn-Sham potential can be broken down into three terms, as follows:

$$v_0[\rho](\mathbf{r}, t) = v_{External}(\mathbf{r}, t) + v_{Hartree}[\rho](\mathbf{r}, t) + v_{xc}[\rho](\mathbf{r}, t) \quad (2.35)$$

The first term is the external potential acting on electrons due to the electromagnetic radiation and the second term is the Hartree term which is given by:

$$v_{Hartree}[\rho](\mathbf{r}, t) = \int \frac{\rho(\mathbf{r}', t)}{|\mathbf{r} - \mathbf{r}'|} d\mathbf{r}' \quad (2.36)$$

The third term is the time-dependent exchange-correlation potential, whose functional form is unknown as in the case with the time-independent systems. Thus, some approximations

were proposed to construct exchange correlation potential, $v_{xc}[\rho](\mathbf{r}, t)$. In the simplest case, it is assumed to be completely local in time, and that it can be evaluated as the ground state (time-independent) exchange-correlation functional of the instantaneous electron density at time t as follows:

$$v_{xc}[\rho](\mathbf{r}, t) \approx v_{xc}[\rho_t](\mathbf{r}) \quad (2.37)$$

This method, called as adiabatic approximation, describes the time evolution of the electron density. However, this method involves very high computational cost, as it involves numerically integrating the time-dependent Kohn-Sham equations for any significant amount of time.

2.4.4. The Linear Response Theory

In this approach, the electronic excitation energies are computed by considering the linear response⁸ of the ground state densities over a small perturbation to the system by external electromagnetic field. The great advantage in using this approach is that the variation of the system only depends on the ground state densities so that we can use all the properties of DFT.

Considering a small perturbation on electronic Hamiltonian due to external electromagnetic field, Hamiltonian becomes,

$$H = H^{g.s.} + H^1(t) \quad (2.38)$$

Here $H^1(t)$ is perturbed Hamiltonian correction. Because the perturbation is arising due to the electric field with electric dipole moment, we write,

$$H^1(t) = -\mu_z E \cos(\omega t) \quad (2.39)$$

Here ω is the frequency and μ is the transition dipole moment operator and E is electric field energy.

And the density will also change as follows

$$\rho(\mathbf{r}, t) = \rho^{g.s.} + \rho^{trans}(\mathbf{r}, \omega) \cos(\omega t) \quad (2.40)$$

Here, $\rho^{trans}(\mathbf{r}, \omega)$ are the transition densities in the form of amplitudes with the ω frequency

This change in total densities or otherwise called transition densities is made with occupied orbitals (holes) and unoccupied orbitals (electrons), which is given by,

$$\delta\rho(\mathbf{r}, \omega) = \sum_{ai} \delta P_{ai}(\omega) \psi_a(\mathbf{r}) \psi_i^*(\mathbf{r}) + \sum_{ia} \delta P_{ia}(\omega) \psi_i(\mathbf{r}) \psi_a^*(\mathbf{r}) \quad (2.41)$$

Here $\delta P_{ai} (ia)$ are the expansion coefficients that connect spatial distribution of orbitals and increment in total density. The whole problem with TDDFT is to find proper frequencies and proper expansion coefficients (one for excitation and other for emission), whose expressions are given as:

$$X_{ai} = \delta P_{ai}(\omega) \text{ and } Y_{ai} = \delta P_{ia}(\omega) \quad (2.42)$$

These expansion coefficients are expressed in the form of matrix known as Casida equations, which are explored as eigenvectors, and the solutions to which correspond to the excitation energies (ω_I)

$$\begin{bmatrix} A & B \\ B & A \end{bmatrix} \begin{bmatrix} X \\ Y \end{bmatrix} = \omega_I \begin{bmatrix} 1 & 0 \\ 0 & -1 \end{bmatrix} \begin{bmatrix} X \\ Y \end{bmatrix} \quad (2.43)$$

Using this approach (practiced in Gaussian 09 software), optical absorption spectra can be obtained in a good agreement with experimental data.

2.4.5. Plotting Absorption Spectra

For plotting absorption spectra, ω_I (energies of occupied and unoccupied energy states) and f_I (the oscillation strengths) obtained for linear response method are used. The oscillation strengths are given as

$$A(\omega) = \frac{1}{\sigma\sqrt{(2\pi)}} \sum_I f_I \exp \frac{-(\omega_I - \omega)^2}{\sigma^2} \quad (2.44)$$

Here the expression for the oscillation strengths is given by:

$$f_I = \frac{2m_e(\epsilon_k - \epsilon_l)}{3\hbar^2} |D_I|^2 \quad (2.45)$$

Here, ϵ_k and ϵ_l are energies of occupied and unoccupied energy states; D_I are the expectation values of transition dipole moments whose expression is given as follows:

$$\langle D \rangle_I = \text{tr}(\rho(\mathbf{r}, \omega)\boldsymbol{\mu}) \quad (2.46)$$

Here $\rho(\mathbf{r}, \omega)$ are the transition densities obtained from Casida equations and $\boldsymbol{\mu}$ is the dipole moment operator.

2.5. References

- 1 Hohenberg, P. & Kohn, W. Inhomogeneous Electron Gas. *Physical Review B* **136**, B864-+, doi:DOI 10.1103/PhysRev.136.B864 (1964).
- 2 Levy, M. Electron-Densities in Search of Hamiltonians. *Physical Review A* **26**, 1200-1208, doi:DOI 10.1103/PhysRevA.26.1200 (1982).
- 3 Lieb, E. H. Density Functionals for Coulomb-Systems. *Int J Quantum Chem* **24**, 243-277, doi:DOI 10.1002/qua.560240302 (1983).
- 4 Perdew, J. P. & Schmidt, K. Jacob's ladder of density functional approximations for the exchange-correlation energy. *Aip Conf Proc* **577**, 1-20 (2001).
- 5 Kresse, G. & Furthmuller, J. Efficiency of ab-initio total energy calculations for metals and semiconductors using a plane-wave basis set. *Computational Materials Science* **6**, 15-50 (1996).
- 6 Frisch, M. J. *et al. Gaussian 09*. (Gaussian, Inc., 2009).

- 7 Runge, E. & Gross, E. K. U. Density-Functional Theory for Time-Dependent Systems. *Physical review letters* **52**, 997-1000, doi:DOI 10.1103/PhysRevLett.52.997 (1984).
- 8 Petersilka, M., Gossmann, U. J. & Gross, E. K. Excitation energies from time-dependent density-functional theory. *Phys Rev Lett* **76**, 1212-1215, doi:10.1103/PhysRevLett.76.1212 (1996).

3. EFFECT OF SURFACE LIGANDS ON ELECTRONIC AND OPTICAL PROPERTIES OF QUANTUM DOTS

Photophysics of QDs is significantly sensitive to its surface chemistry. Presence of any dangling bonds results in blinking and photobleaching, thus reduces its applicability in fields such as biolabelling, sensors and optics. To avoid such problems, QDs surface is passivated by certain ligands in the process of their synthesis using methods like colloidal synthesis. Although the surface atoms are passivated by ligands, their core nature preserves the structure of its bulk parent crystal.

Even though core structure is responsible for the actual physical properties and confinement effects of QD, surface passivation perturbs these properties. Thus, one has to be careful with the choice of the ligands passivation. Ligands passivation must enhance the solubility and reduce the chemical sensitivity of QDs.

However, inefficient surface passivation, as we will see in chapter 4, will lead to the appearance of surface/trap states and thus affecting radiative and non-radiative processes.

Although QDs are known for about 40 years to date, much less is understood about the surface chemistry effects on photophysical properties. Nonetheless, studying the surface chemistry itself is very complicated. Herein we provide our insights into the effect of ligand passivation on the electronic structure and optical properties of QD are essential to understand the role of surface chemistry.

This chapter is subdivided into two chapters, namely 3.1 and 3.2. In chapter 3.1, effect of thiols capping on the electronic structure and optical properties of CdSe QDs is detailed. In chapter 3.2, effect of surface oxidation of PbSe QDs on their optoelectronic properties are investigated.

3.1. Effect of Thiols Capping on the Electronic and Optical Properties of CdSe QDs

3.1.1. Introduction

CdSe Quantum dots (QDs) have received an increasing attention in wide range of applications such as solar cells¹, optical sensors² and light emitting diodes (LEDs)³, because of their narrow emission and photo stability nature. Application of these QDs in biomedical field requires bright photoluminescence (PL) emission and biocompatibility. Commonly synthesized CdSe quantum dots through colloidal synthesis uses hydrophobic ligands such as trioctyl phosphine oxide (TOPO) and hexadecyl amine (HDA) as the passivating ligands.^{4,5} However, these ligands limit their scope for further functionalization at the ends⁶; they are poorly soluble in polar solvents and are not biocompatible.

Thus, many researchers focused on synthesizing water soluble QDs through ligand exchange and encapsulation methods. The encapsulation method led to the increase in particle size of QDs, restricting their applications in bio-imaging.⁷ Ligand exchange, although possible, required high temperatures to replace TOPO and HDA, thus making it a demanding area of research to overcome this limitation.⁸ Thiols are known to be more stable than phosphine capped QDs, and they are easy to be functionalized further making them suitable for various applications.

Majetich et al. reported an increased PL of CdSe QDs capped with butanethiolate.⁹ Kuno et al. reported a decreased PL quantum yield (QY) of CdSe QDs from 15% to 1% after ligand exchange of TOPO with thiophenol and 4-(trifluoromethyl)thiophenol.¹⁰ Also, Su et al. reported ligand exchange of TOPO with aromatic thiol ligands enhanced PL quenching.¹¹ Their studies showed that thiol ligands effectively scavenge the photo-generated holes in CdSe, thus

quenching their PL. In another study, Hollingsworth et. al showed that effect of QDs PL can be advantageous or adverse, depending on the concentration of thiolate anion.¹²

Recently Zheng et al. published their results on ligand exchange of TOPO capped CdSe/ZnS QD with thiol ligands such as glutathione and cysteamine under mild conditions. The resulted QDs showed superior stability and optical properties.¹³

Based on the literature studies, it is still unclear whether thiols increase or decrease the PL efficiency to date. One of the reasons for this discrepancy is due to the complex surface chemistry of QDs. Thus, here in, we report our quantum chemistry results to give insights in to the optical and electronic properties of CdSe QDs passivated by small ligands such as methanethiol.

3.1.2. Computational Details

3.1.2.1. Structural Models

We performed our theoretical calculations on the magic sized quantum dot ($\text{Cd}_{33}\text{Se}_{33}$) cut from a bulk crystal of wurtzite. $\text{Cd}_{33}\text{Se}_{33}$ QD has 21 surface atoms of each of Cd and Se. To study photophysical properties of thiol functionalized QDs, all 21 of Cd atoms were capped with CH_3SH . The geometries were optimized with Gaussian 09 software package¹⁴, utilizing the PBE1PBE¹⁵⁻¹⁷ functional and a mixed basis set containing LANL2DZ^{18,19} for Cd and Se, and 6-31g*^{20,21} for all other atoms that are included in a ligand. Solvent effects were studied using the CPCM²² (Conductor-like Polarization Continuum Model) that was implemented in Gaussian 09 software. We have particularly implemented this methodology as this was proven to show band gaps in good agreement with experimental results in previously published papers for these systems.²³

3.1.2.2. Electronic Structure and Optical Response Calculations

Density of States (DOS) and absorption spectra were computed employing Gaussian line-broadening as follows:²⁴

$$A(\omega) = \frac{1}{\sigma\sqrt{2\pi}} \sum_n h_n \exp\left(-\frac{(\omega_n - \omega)^2}{\sigma^2}\right) \quad (3.1)$$

Here h_n is transition strength, ω_n is the transition energy and σ is the spectral line width, whose definitions vary with type of calculations we perform. For plotting DOS, $\omega_n = \varepsilon_k$, where ε_k is the ground state molecular orbital energy. For evaluating total DOS, $h_n = 1$, whereas for the fragmented DOS, it is evaluated as the fraction of orbital localized on a specific fragment, as computed in Gaussian 09. For plotting absorption spectra, $\omega_n = \varepsilon_k - \varepsilon_l$ (where ε_k and ε_l are energies of occupied and unoccupied energy states) and $h_n = f_{kl}$ (where f_{kl} is the oscillation strength). The oscillation strengths are given as

$$f_{kl} = \frac{2m_e(\varepsilon_k - \varepsilon_l)}{3\hbar^2} \mu_{kl}^2 \quad (3.2)$$


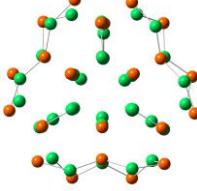
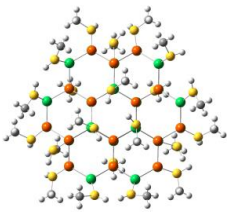
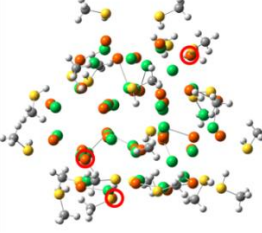
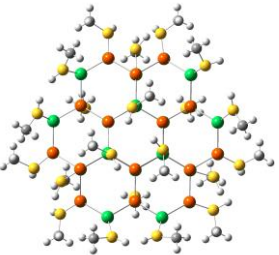
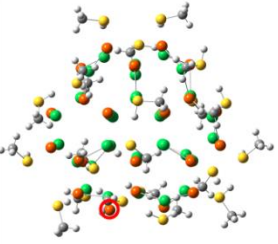
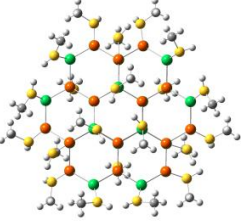
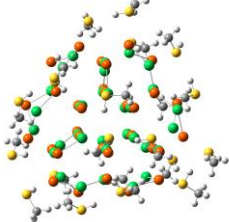
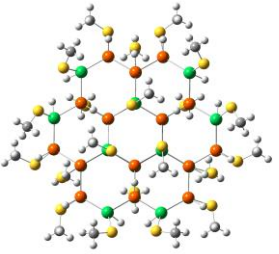
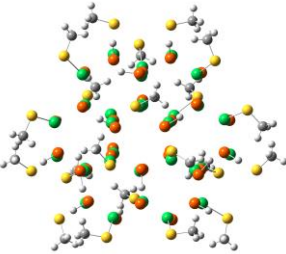
Here $\mu_{kl} = \langle \psi_k | \hat{\mu} | \psi_l \rangle$, are the transition dipole moments between ψ_k and ψ_l molecular orbitals and $\hat{\mu}$ is the dipole moment operator.

3.1.3. Results and Discussion

3.1.3.1. Structure Optimization of QDs

We optimized structures of bare Cd₃₃Se₃₃ (without any ligand passivation) and full passivation of Cd₃₃Se₃₃ with 21 methanethiol ligands (CH₃SH) in vacuum, propyl amine (less polar solvent) and acetonitrile (more polar solvent) using methodology that was described in section 3.1.2. The initial and final relaxed structures are shown in Table 3.1. After relaxation, the thiol capped QDs structures seemed to look different depending on the relaxation conditions.

Table 3.1. Initial and relaxed geometries of both protonated and deprotonated thiols functionalized CdSe QDs. Structures are labelled from 1(a) to 1(g) and these notations were used in description

Description	Relaxation conditions	Geometry before relaxation	Geometry after relaxation
Bare QD	Initial geometry relaxed in acetonitrile solvent	1(a) 	1(b) 
Mostly deprotonated	Completely protonated geometry relaxed in vacuum and in acetonitrile solvent	1(c) 	1(d) 
Partially deprotonated	Completely protonated geometry relaxed in amine and then relaxed in acetonitrile solvent	1(c) 	1(e) 
Completely protonated	Completely protonated geometry relaxed in acetonitrile solvent	1(c) 	1(f) 
Completely deprotonated	Completely deprotonated geometry relaxed in acetonitrile solvent	1(g) 	1(h) 

In vacuum, at least 14 out of 21 of the thiols lost their protons and among them, 3 protons were formed bonds with each of the 3 surface selenium atoms. This relaxed geometry was re-optimized in acetonitrile solvent as shown in Table 3.1, structure 1(d) where the protonated Se atoms were marked in red circles. This relaxation is termed as mostly deprotonated case for better description of the model in further sections. In another study, in propyl amine solvent, only 9 out of 21 thiols deprotonated and out of which only of proton formed bond with surface selenium atoms. This structure was re-optimized in acetonitrile solvent, whose structure labelled as 1(e) is shown in Table 3.1. This is termed as partially deprotonated case, as fewer ligands were deprotonated. Furthermore, no such deprotonation was observed in presence of acetonitrile (very polar solvent) as shown in structure 1(f) as shown in Table 3.1. The obtained geometry in this case was termed as completely protonated case. For our curiosity, we functionalized QD with thiolate (deprotonated thiols) at all 21 of the Cd atoms and H^+ ions (protons) at every surface Se atom as shown in Table 3.1, entry 1(c). Overall, the system remains neutral and in singlet state, that allows it to behave as a closed shell system. After relaxation, we did not observe any disturbance in the position of attached ligands as shown in structure 1(h) in Table 3.1. This is termed as completely deprotonated case.

3.1.3.2. Natural Bond Order (NBO) Analysis

NBO charge analysis was performed to investigate the charge of transferred H atom from S to Se. Table 3.2 lists the NBO values, which show that H-atom transferred is indeed a proton. Also we observed that overall charge on an atom increases with increase in polarity of solvent. The values also show the charge on thiols in both protonated and deprotonated forms, which provides an interesting observation that thiolates to thiol ratio is different in different cases.

Analyzing the values from this table along with the information about absorption spectra, one can correlate the relation between thiolates concentration and PL efficiency.

3.1.3.3. Electronic Properties of QDs

As shown in Figure 3.1, total Density of States (DOS) were plotted for the QDs passivated with thiol ligands in presence propyl amine and acetonitrile. We couldn't find any significant changes from this data. Overall, it shows that functionalization of QD with thiols has a minor effect on the band gap and DOS structure. To further evaluate the contribution of ligands specifically in detail, we plotted fragmented DOS as shown in Figure 3.1. We show fragmented DOS of all the relaxed structures that were mentioned in section 3.1.3.1 in acetonitrile solvent exclusively to compare the effect of structural changes on the fate of energy states in a polar medium. Our results show that in case of mostly and partially deprotonated cases, ligands added states only deep inside the conduction and valence band, and most of the band edge states are corresponding to the surface Cd and Se atoms as shown in Figure 3.1(a) and (b) respectively. Similar effect was seen in case of completely protonated system as shown in Figure 3.1 (c), but a huge difference is seen in the case of completely deprotonated system, Figure 3.1 (d). We observed a major contribution from thiolates near the edge of valence band decreasing the band gap. It has been reported previously that thiols act as hole scavengers. Our results show that these states (HOMO, Table 3.3) are very localized near the ligands indicating that they are acting as hole traps. To understand the nature of these energy states, we further examined the absorption spectra of these cases, discussed in section 3.1.3.4.

Table 3.2. Natural bond order charge analysis values of each of thiol capped QDs

Solvent	System notations (Ref Table 1)	Natural bond order charge analysis							
		Cd		Se		S		H	
		Bond to Se	Bond to S	Bond to Cd	Bond to H	Bond to Cd	Bond to H	Bond to Se	Bond to S
Vacuum	1d	+0.95	+1.07	-1.00	-0.60	-0.51	-0.06	0.13	0.19
Acetonitrile	1d	+1.03	+1.24	-1.17	-0.66	-0.57	-0.12	+0.10	0.16
	1e	+1.00	+1.30	-1.00	-0.65	-0.14	-0.08	0.10	0.17
	1f	+1.15	+0.95	-1.11	N/A	-0.10	-0.06	N/A	0.18
	1h	+1.10	+1.33	-1.09	-0.65	-0.62	N/A	0.11	N/A

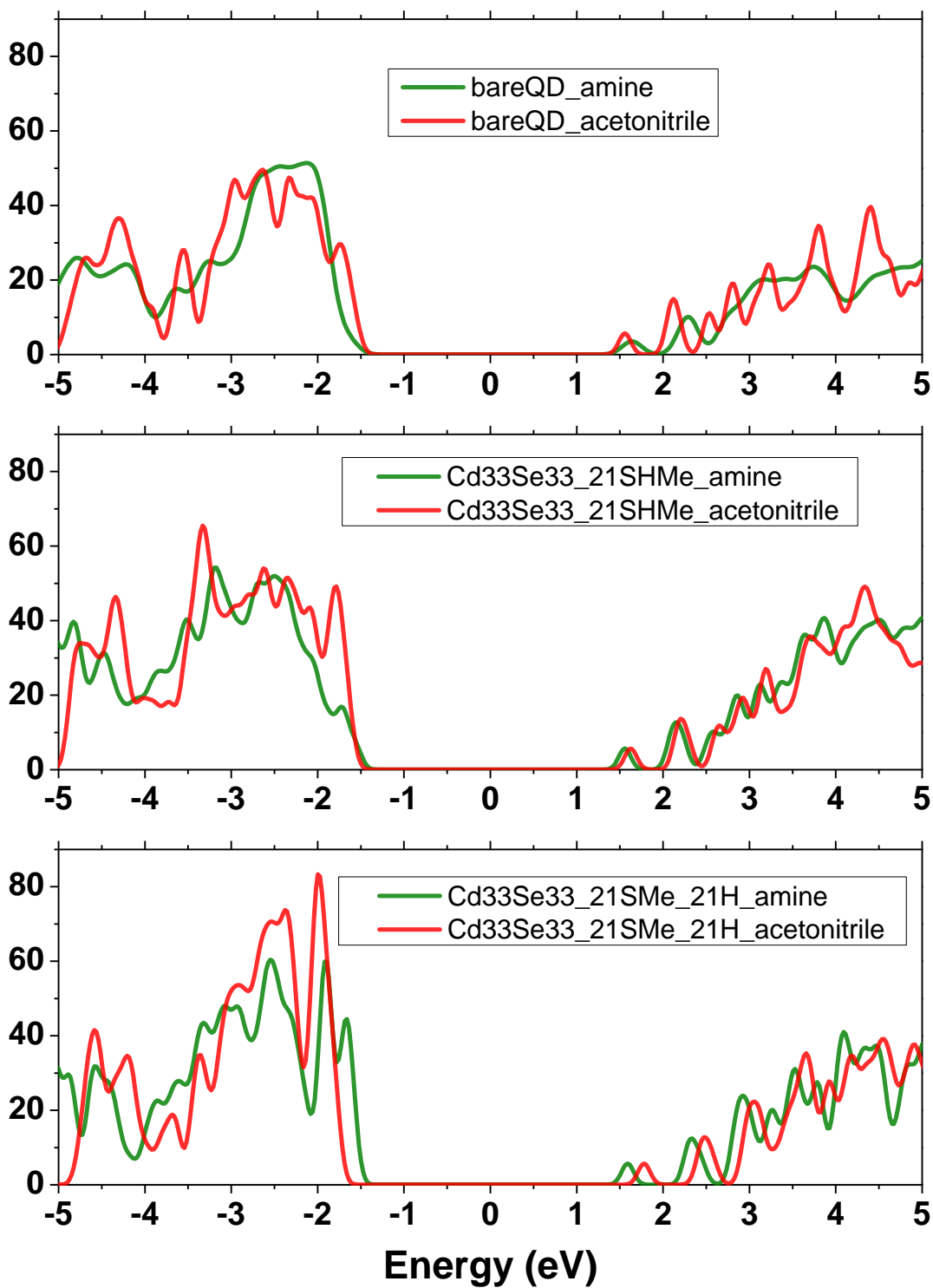


Figure 3.1. Total DOS of the QD in presence of amine and acetonitrile in absence and presence of ligands

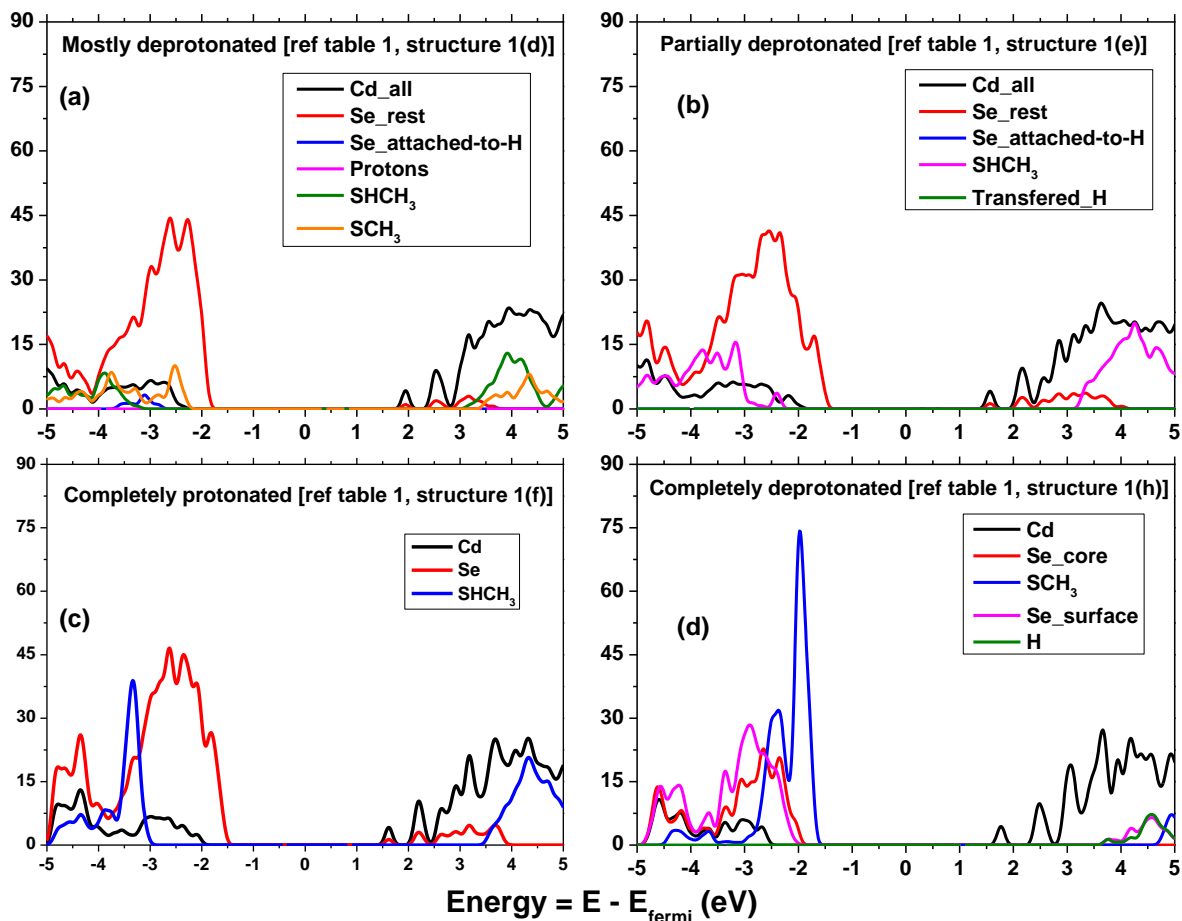


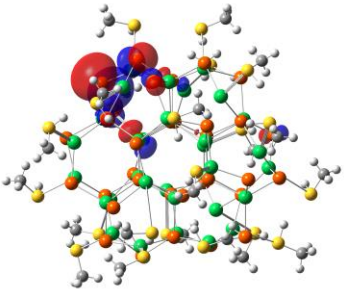
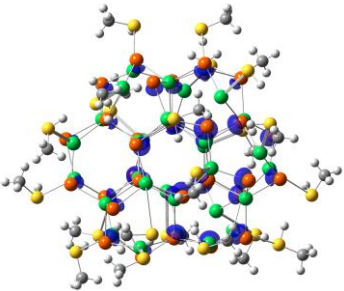
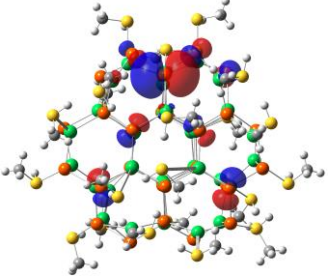
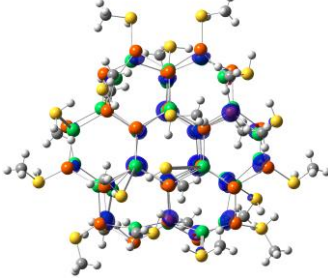
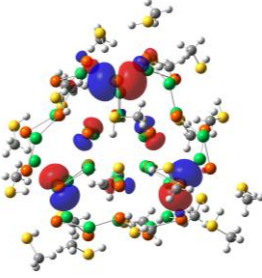
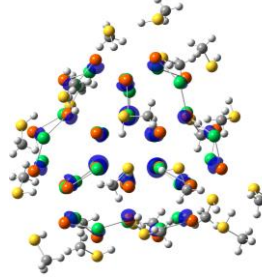
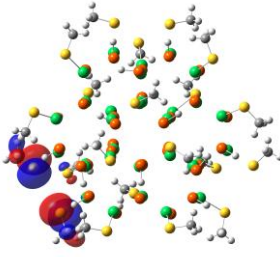
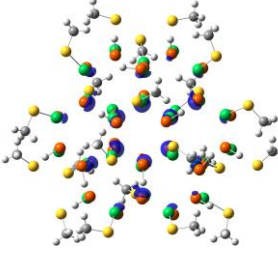
Figure 3.2. Fragmented DOS of QD passivated by thiols in acetonitrile solvent in case of (a) mostly deprotonated ligands, (b) less deprotonated, (c) completely protonated and (d) completely deprotonated

3.1.3.4. Absorption Spectra

We performed time dependent density functional theory (TDDFT) calculations to obtain the absorption spectra. For these computations, we used same functional and basis set as discussed in the previous sections. The first 100 singlet energy states were calculated; with Gaussian line width broadening of 80 meV to produce the spectra on the obtained oscillation strengths from TDDFT as shown in Figure 3.3. The absorption spectra were further red-shifted in all the four cases, in presence of vacuum compared to that in polar solvents. This effect clearly shows the sensitivity of thiol capped ligands in solvents, the trend of blue-shifting of the spectra

with increase in polarity shows that these QDs behave as hypsochromes (negative solvatochromism). We observed not very bright first energy states in case of partial deprotonation. This is also evident from natural transition orbital diagrams shown in Table 3.4, that the HOTO is somewhat localized, whereas LUTO is more delocalized. In case of mostly deprotonated system, we observed that bright energy states appear at the first energy band showing that this case will enhance the PL of QD. Also delocalization of NTOs support the reason for the bright states in first energy band. In case of completely protonated system, we could not obtain the absorption spectra in presence of vacuum or propyl amine solvent. We have obtained the spectra only in presence of acetonitrile. Although fragmented DOS did not show any evidence of trap states, absorption spectra revealed semi-dark states at the first energy region. In the case of completely deprotonated system, we observed many trap states at the first energy band and the related NTOs also show very localized orbitals. This suggests that presence of more negatively charged ligands (thiolates) introduce trap states which in turn decreases the PL efficiency. An equilibrium concentration of thiols/thiolates as in case of mostly deprotonated system a necessary to serve as better capping for the PL enhancement.

Table 3.3. HOMO and LUMO of the relaxed geometries in acetonitrile solvent

Case	HOMO	LUMO
Mostly deprotonated		
Partially deprotonated		
Completely protonated		
Completely deprotonated		

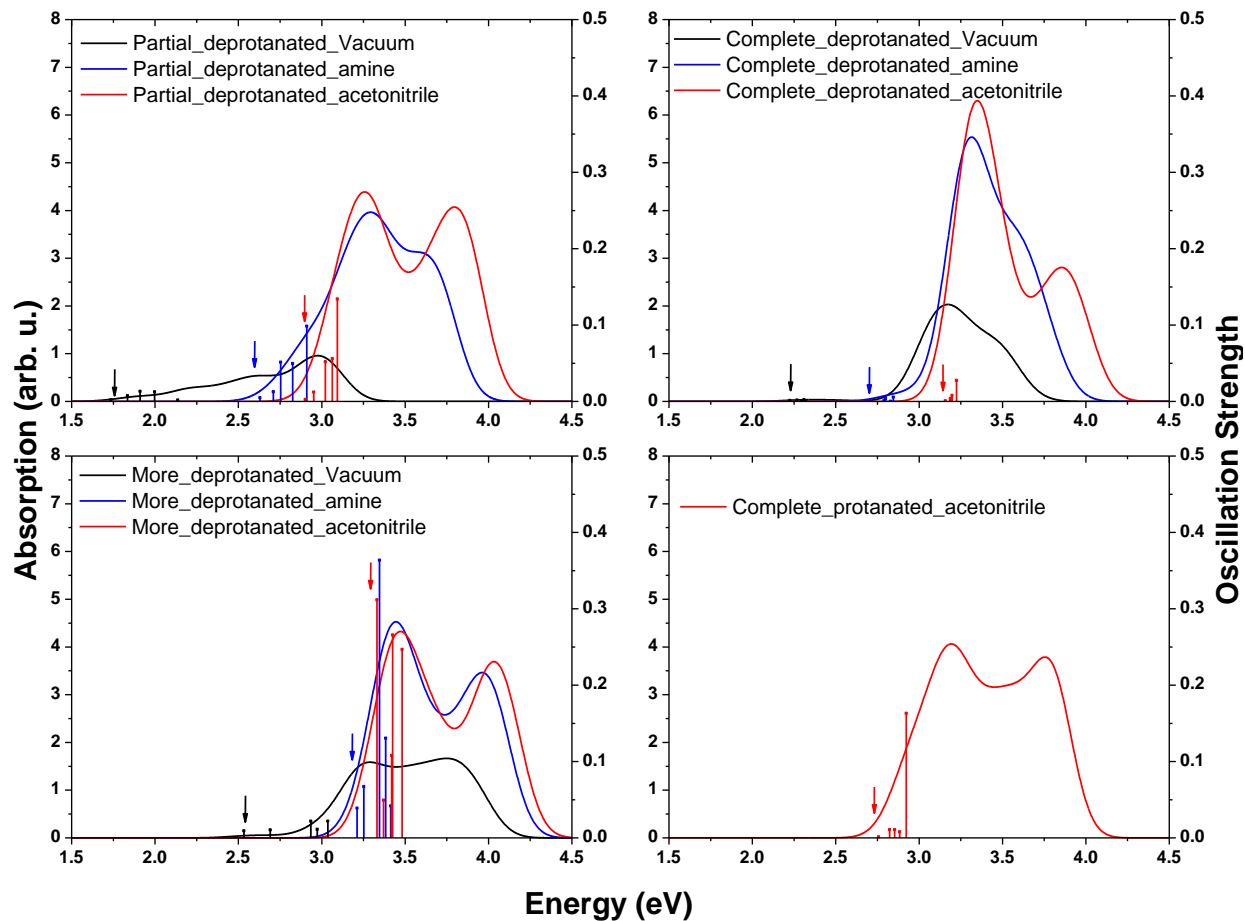
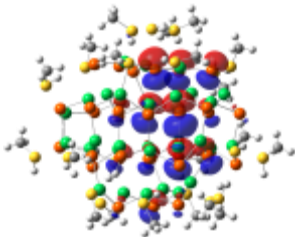
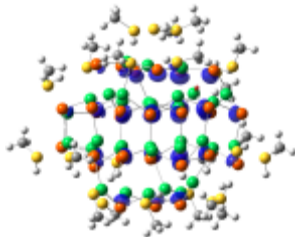
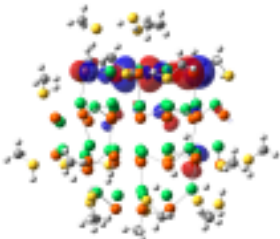
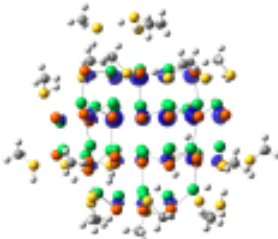
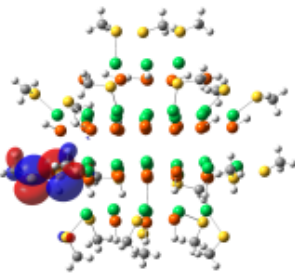
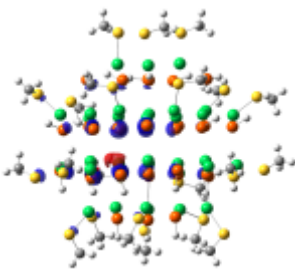
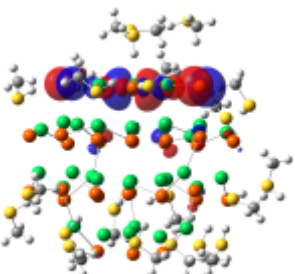
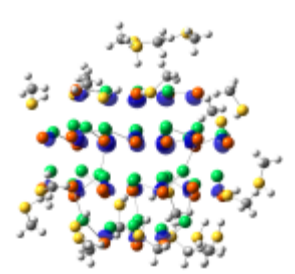


Figure 3.3. Absorption spectra of the all four cases in presence of vacuum, propyl amine and acetonitrile solvents as indicated in the graphs (a) partially deprotonated, (b) mostly deprotonated, (c) completely deprotonated and (d) completely protonated.

Table 3.4. NTOs of 4 different cases in acetonitrile solvent

Case	HOTO	LUTO
Mostly deprotonated		
Partially deprotonated		
Completely deprotonated		
Completely protonated		

3.1.4. Conclusions

In this paper, we have investigated the effect of solvents efficiency in capping the thiol ligands on to the QDs surface and their optical properties. Although a minimal effect of ligands

on the total DOS and the band gap value was seen, we observed that the ligands alter the nature of energy states near band edges. We did not see trap states in case of complete protonated, mostly deprotonated and partial protonated systems, but there were trap states introduced at the valence band edge in case of complete deprotonation. We concluded that the appearance of these states are due to localization of orbitals on the ligands, proving that in this case, thiols act as hole traps.

From the absorption spectra calculations, we determined that presence of only thiolates brings up dark/semi-dark states near the first energy band, showing that this will quench the PL. Presence of thiolates/thiols in equilibrium not only removes these dark states, but also introduce much brighter first energy states and a blue-shift of the spectra.

3.2. Effect of Surface Oxidation of PbSe QDs on their Optoelectronic Properties

3.2.1. Introduction

Extensive research has been already done since past 10 years in studying lead chalcogenides quantum dots due to their potentiality to serve as optoelectronic devices.^{25,26} In this category, PbSe QDs proved to exhibit strong confinement effects as they have a large exciton Bohr radius of about 46 nm.²⁷ This property along with their strong tendency towards charge carrier multiplications made them to find their applications in fields such as photovoltaic cells and diodes.²⁸

Nevertheless, there have been reports showing that PbSe QDs are chemically instable when exposed to air.²⁹ Even trioctylphosphine ligand passivated PbSe QDs prepared by colloidal synthesis showed a rapid degradation when exposed to air for just a short period of time.³⁰ Although an extensive work is under way to improve synthesis methods by altering ligands to reduce aerial oxidation, the actual effects of oxidation on the surface of PbSe QDs is still not explored largely. One of the interesting observations made by Klimov's research group from Los Alamos National Lab in their synthesized PbSe QDs is that a rapid oxidation led to a reduction of their volume to about 50% within 24 h.²⁹ Their experiments showed that absorption and PL shifted to higher energies and causing a rapid PL quenching within minutes after aerial exposure, followed by slow recovery of PL quantum yield within few hours, exceeding to those observed prior to air exposure. They attributed the short-term PL quenching to enhanced carrier trapping and PL recovery to reduction in the efficiency of non-radiative inter-band recombination due to increase of the band gap in oxidized QDs.

In this chapter, emphasis is given to theoretically understand the effect of oxidation on electronic structure and optical properties by studying the overall mechanism on how aerial exposure for a short time can cause PL quenching followed by a slower enhancement of PL.

Previously published theoretical results mainly concentrated on molecular oxygen, showing that oxygen bound to the surface of PbSe QD introduce in-gap states in their DOS and that these surface states are responsible for PL quenching.^{31,32} In our paper, we extend our investigation to other forms of oxygen as well, such as, ionic oxygen and atomic oxygen, and how each of these species can interfere or effect the electronic structure and absorption spectra of QDs.

3.2.2. Computational Details

3.2.2.1. Structural Models

We modelled two different sized PbSe QDs of Wurtzite structure: 1 nm QD comprising 16 atoms of each of Pb and Se, represented as $\text{Pb}_{16}\text{Se}_{16}$ and a 2 nm QD with 68 atoms of each of Pb and Se, represented as $\text{Pb}_{68}\text{Se}_{68}$. As shown in Figure 3.4, these structures have 3 different facets, namely, 100, 110 and 111. Various attachment modes of oxygen source, such as oxygen ion, atom and molecule with varying concentrations in 3 different facets were modelled and optimized.

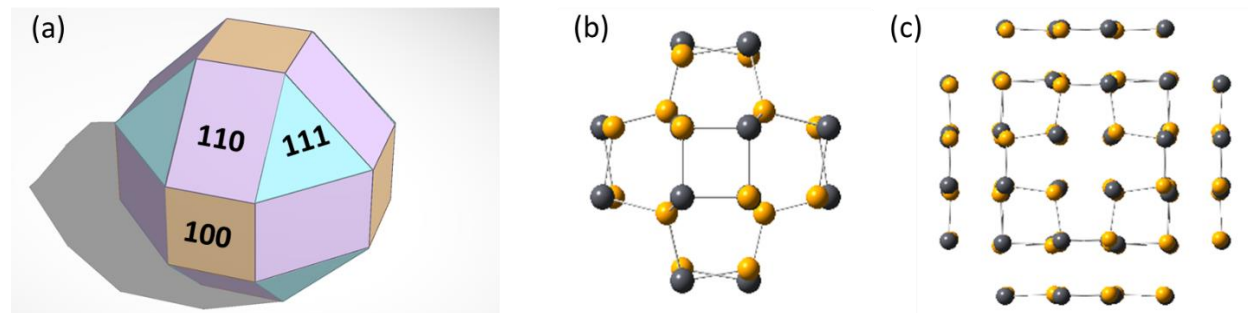


Figure 3.4. Different facets on the structure colored differently on each surface to identify the facet. There are 6 yellow surfaces are facet 100, 12 purple surfaces are facet 110 and 8 blue surfaces are facet 111, totaling up to 26 surfaces on the QD

3.2.2.2. Computational Methodology

All calculations were performed using Gaussian 09¹⁴ software package including ground-state geometry optimization and TDDFT. The systems were mostly optimized in singlet states (with exception of oxygen atom and molecule in triplet state for binding energy calculations) using density functional theory (DFT) based on the hybrid functional, PBE1PBE¹⁵ with 6-31G*²¹ basis set for O atoms and LANL2DZ¹⁸ basis set for Pb and Se atoms. Same basis set and functional were used to perform TDDFT, to obtain absorption spectra.

3.2.3. Results and Discussions

3.2.3.1. Binding Energy

Binding energy of ligands on QDs was determined to understand the strength of each of the oxygen species on every facet of PbSe QD. We computed the binding energy in all cases using the following equation:

$$\text{Binding energy / ligand} = \frac{E_{QD_ligand} - E_{QD} - n * E_{ligand}}{n}$$

Here E_{QD_ligand} , is the total energy of ligand attached QD, E_{QD} is the total energy of bare QD, E_{ligand} is the total energy of the ligand and n is the number of attached ligands.

The binding energy values were plotted for each of the oxygen species, including atom, ion and molecule as shown in Figure 3.5. Overall, binding energy is strongest in case of ion, moderately strong in case of atom and lowest binding in case of oxygen molecule. In case of binding of oxygen as molecule, at 100, O₂ dissociates to form Pb-O and Pb-O-Se, at 110, they form Se-O or not dissociated Pb-O₂ bond and at 111, there is formation of Se-O bond. This result shows that there is strong chance for oxygen to dissociate at 100 and 110 facets. However, O-atoms found to strongly bind at 110 and that they tend to form bonds with 2 Pb atoms and 1 Se atom as shown in the entry 2 of Table 3.5. In case of O-ions, we observe that they are strongly

biding in the form of Pb-O-Pb nearly same in all facets as shown in Figure 3.5. The most interesting result is the oxygen in their ionic form is trying to bind on the surface by replacing surface Se atom as shown in entries 3 and 4 in Table 3.5. There is no difference in the overall optimization of structure in vacuum versus acetonitrile solvent, except that the binding energy is decreased in presence of solvent.

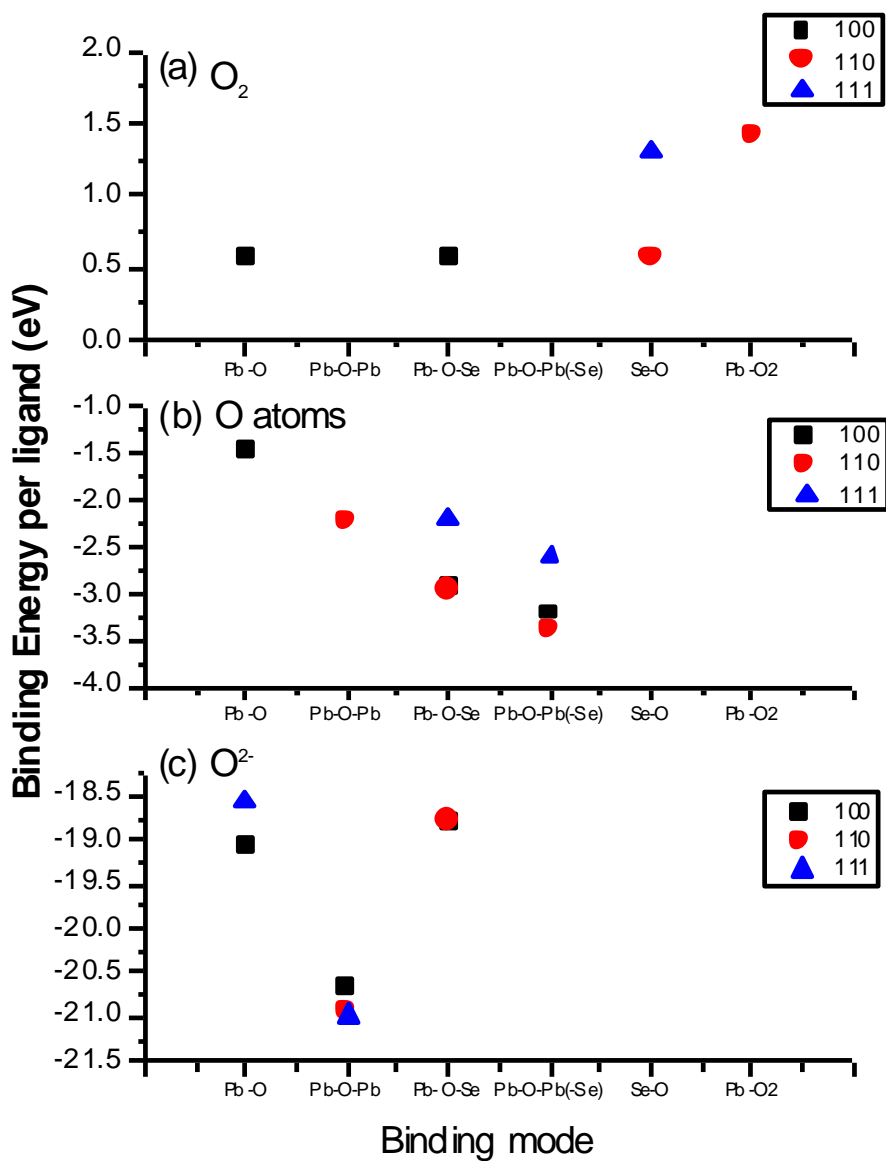

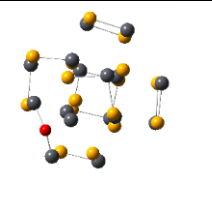
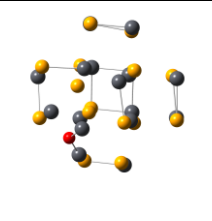
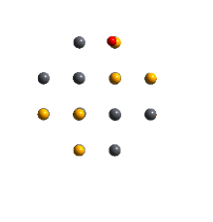
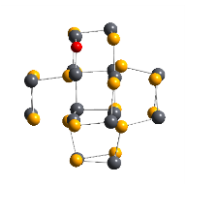
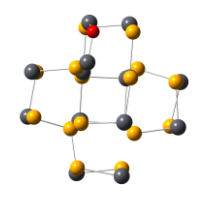
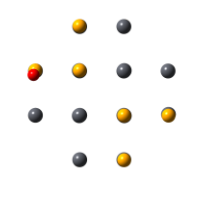
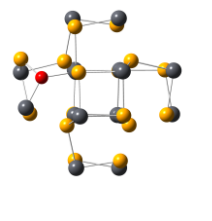
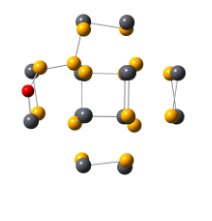
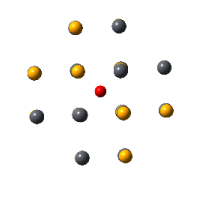
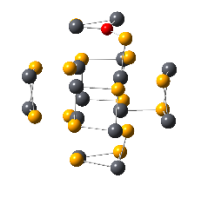
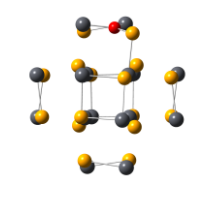


Figure 3.5. Different species of oxygens binding energies on $Pb_{16}Se_{16}$ QD at different facets with (a) single oxygen molecule (b) single oxygen atom and (c) single oxygen ion

Table 3.5. Comparison between oxygen ions and oxygen atoms of selected systems in both vacuum and in solvent (acetonitrile). Difference in binding energy (eV) is more pronounced in the case of oxygen ions.

State	Notation	Initial structure	Optimized geometry structure in vacuum	Bond Length (Å)	Binding Energy (eV)	Optimized geometry structure in solvent (acetonitrile)	Bond Length (Å)	Binding Energy (eV)
Ion	Pb-Pb-Pb 111			Pb-O = 2.07 Pb-O = 2.22 Se O = 3.26 Pb Se = 2.90	-20.99		Pb-O = 2.09 Pb-O = 2.20 Se O = 3.23 Pb Se = 2.90	-9.80
	Se-Se 110			Pb _{1,2} -O = 2.03 Se O = 3.44 Pb Se = 2.92	-20.94		Pb _{1,2} -O = 2.05 Se O = 3.44 Pb Se = 2.94	-10.15
Atom	Se-Se 110			Pb-O = 2.18 Pb-O = 2.23 Se-O = 1.89 Pb-Se = 2.83	-3.39		Pb-O = 2.07 Se-O = 1.84 Pb-Se = 2.87	-2.89
	Pb-Pb 100			Pb-O = 2.17 Se-O = 1.90 Pb-Se = 2.84	-3.21		Pb-O = 2.18 Se-O = 1.90 Pb-Se = 2.86	-3.11

We have also computed binding energies of oxygen on a 2 nm QD. A similar trend is found when compared to 1 nm QD, that, overall an increase in binding was observed going from oxygen molecule to atom to ion as can be seen.

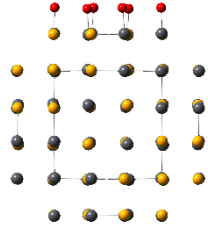
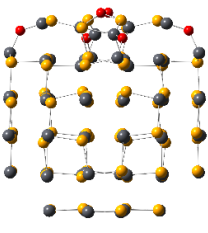
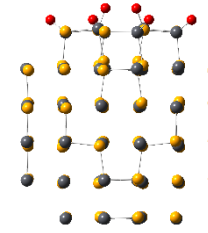
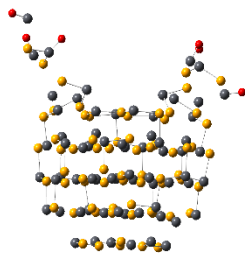
Table 3.6. Lowest binding energy of three different mode of oxygen: atomic oxygen (O-atoms), ionic oxygen (O^{2-}) and molecular oxygen (O_2) in each facet on $Pb_{68}Se_{68}$ in vacuum.

Facet	O atoms		O^{2-}		O_2	
	Initial structure	Optimized structure	Initial structure	Optimized structure	Initial structure	Optimized structure
100						
	-3.05 eV		-21.40 eV		1.47 eV	
110						
	-3.00 eV		-23.40 eV		0.75 eV	
111						
	-2.87 eV		-23.40 eV		1.09 eV	

We have also simulated systems with increased concentration of ions and atoms on a particular facet as shown in Table 3.7. Our results show that there is a strong surface

reconstruction with increase in the concentration of oxygen atom or ions on the surface of QD. In case of ions, we have observed a complete decomposition of a layer of 100 as we attached 6 of O^{2-} ions as shown in Table 3.7. In case of O-atoms binding at 100 facet in vacuum, we observed that there is tendency of these species to penetrate inside the QD, while this effect is less pronounced in presence of acetonitrile as solvent. In case of ionic oxygen, we observed a diminishing of size of QD as charge on the system is high and concentration of electronegative oxygen ions is more.

Table 3.7. Surface reconstruction due to increase in the concentration of oxygen at (100) facet of 2 nm PbSe QD

Initial structure	O-atoms in vacuum	O-atoms in solvent	O^{2-} in vacuum
			

3.2.3.2. Density of States

We then performed DOS plots of the optimized structures and Figure 3.6 is showing DOS of some selected system which show strong influence on the overall electronic structure of QDs. As can be seen in Figure 3.6, O_2 molecule introduces new states near the band edge that show localized HOMO orbitals. In case of decomposed O_2 molecule to atoms, this states seems to be not present near the band edge. Also, in case of O^{2-} , we do not see any new states near band edge. This result confirms that oxygen molecule is the main reason for introduction of new surface states that can in turn result in the quenching of PL.

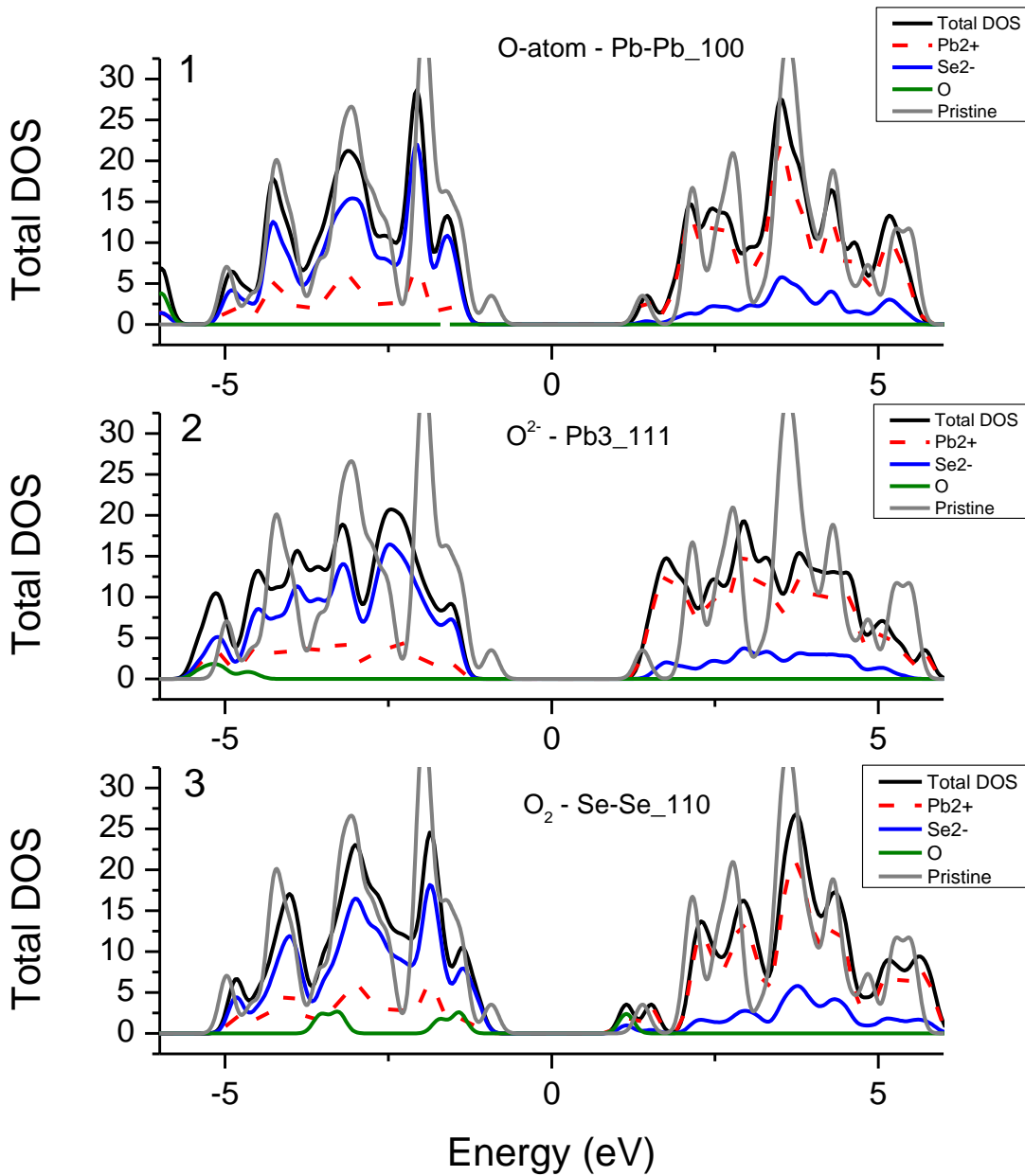


Figure 3.6. Representations of Fragmented DOS (FDOS) of few selected systems where several observations were made. In graph (1), there is a lost and broadening of peaks which is generating a slight blue shift. In graph (2), there is also lost in peaks that leads to blue shift. In graph (3), there is a narrow bandgap contributed by oxygen (oxygen lines scaled to 4 for representation).

3.2.4. Absorption Spectra

As can be seen from Figure 3.7, as the molecular oxygen binds at 110, we saw a strong red shift of the absorption spectra when compared with pristine (bare) $\text{Pb}_{16}\text{Se}_{16}$ QD. However, in case of ion and atom, we observed slightly blue shifted absorption peaks. Overall, the main conclusion we can draw from absorption spectra is that there is appearance of more dark and semi-dark states in case of molecular oxygen binding on the surface of QD. As soon as the oxygen molecule decomposed to ions and atoms, we see a regain of the absorption peaks that resemble pristine QDs absorption spectra. As we observed that O-atoms are replacing surface Se atoms, we made an attempt to optimize 1 nm and 2 nm QDs where all surface Se atoms were replaced with O atoms. Overall, we observed that absorption spectra are resembling the pristine QD with bright 1st energy state. This observation gives an important insight to the experimental observation by Klimov's group that how the quenched PL was recovered after certain number of hours. This observation that oxygen molecules bring surface states at the edge of band gap is also consistent with the theoretical findings from the reported results.

3.2.5. Natural Transition Orbitals

We then plotted excited state electron and hole orbitals, known as natural transition orbitals of these selected systems as shown in Table 3.9. From the NTOs, it is clear that oxygen molecule introduces trap states in the form localized holes. Once the oxygen molecule is dissociated into atoms, we observed delocalized NTOs. Attachment of O-atom also show delocalized NTOs and blue shifted 1st energy state.

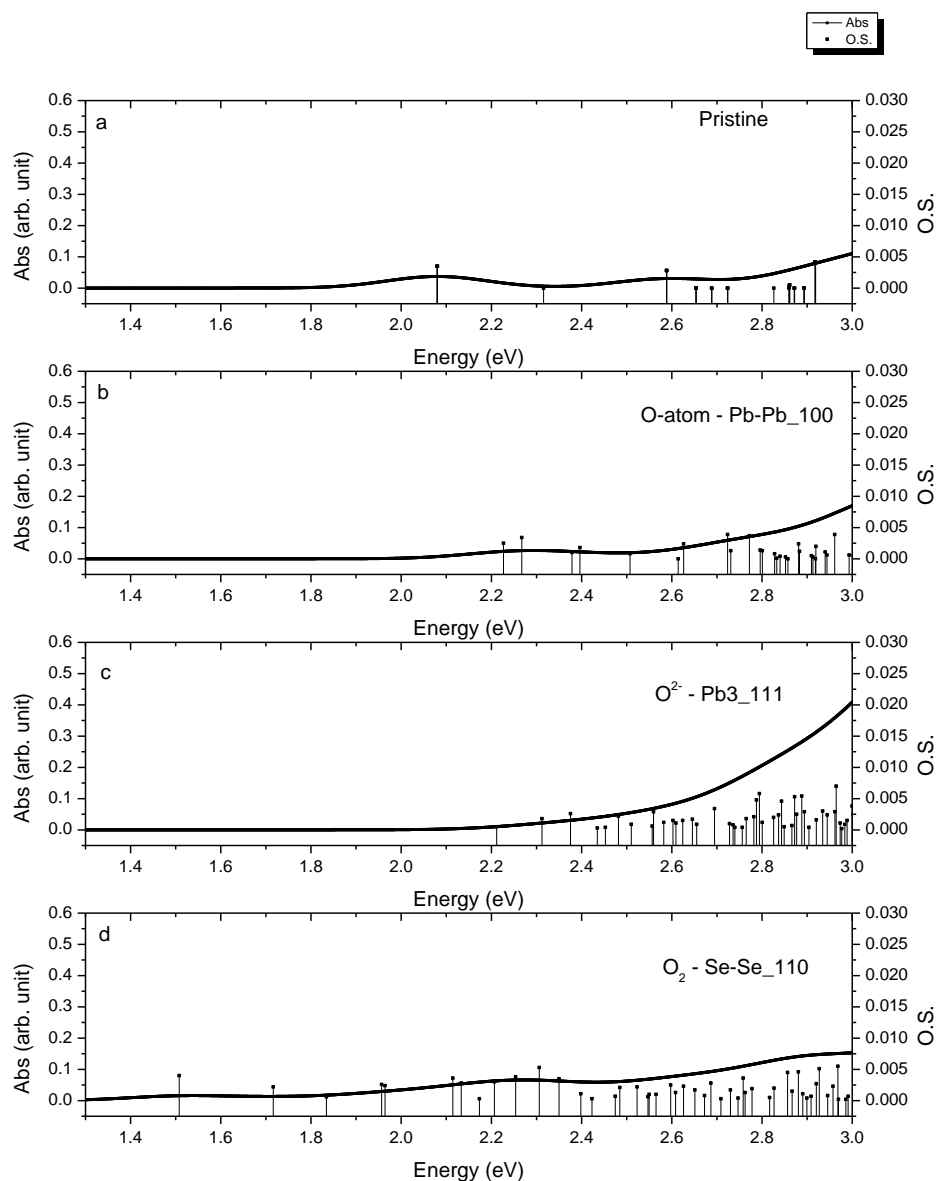


Figure 3.7. Corresponding absorption spectra for the DOS plots in Figure 3.6 **Error! Reference source not found.** where graph (a) shows pristine $\text{Pb}_{16}\text{Se}_{16}$ absorption spectra to compare with selected systems (b), (c) and (d). The blue shift can be observed on (b) and (c) while the first peak that contributes to red shift observed with oscillation strength of 0.004 in graph (d)

Table 3.8. Absorption spectra of oxygen atoms passivated PbSe QD

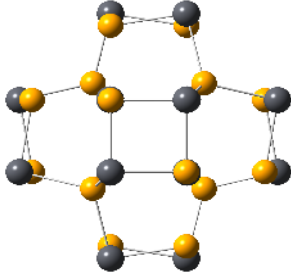
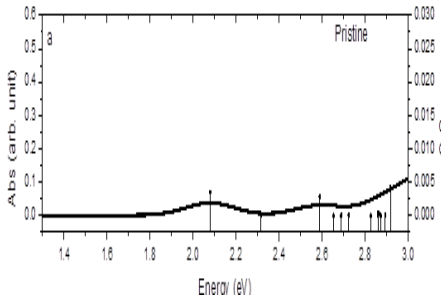
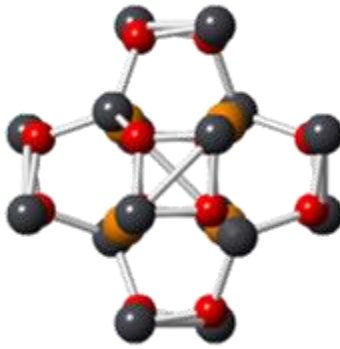
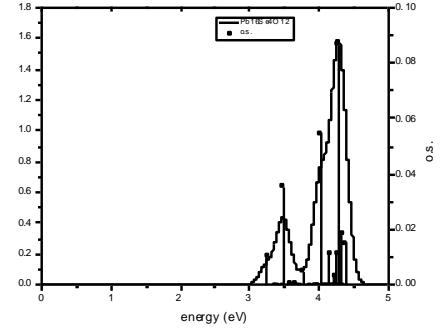
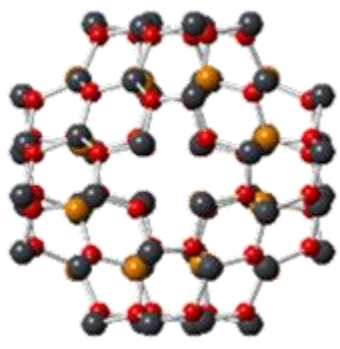
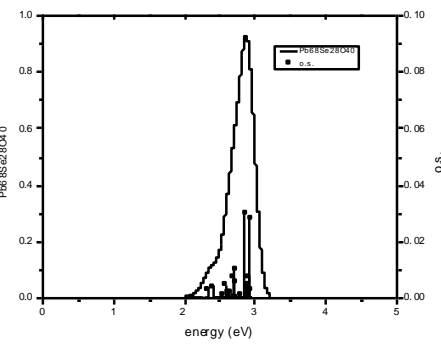
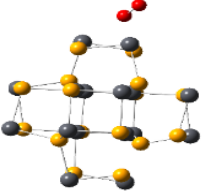
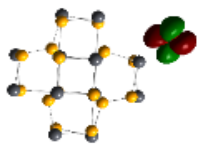
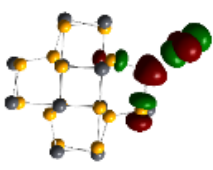
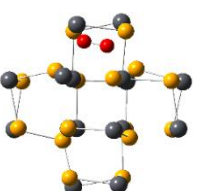
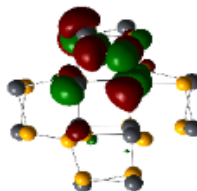
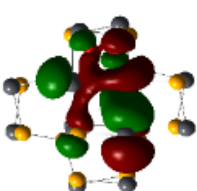
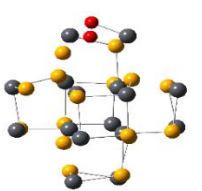
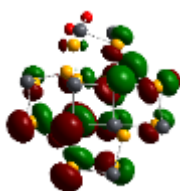
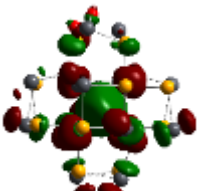
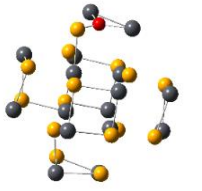
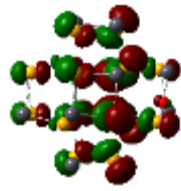
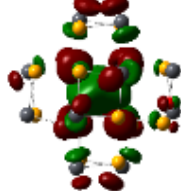
Mode of attachment	Optimized structure	Absorption spectra
Bare QD		
O-atoms substituting all of the Se atoms present on the surface of $Pb_{16}Se_{16}$ QD		
O-atoms substituting all of the Se atoms present on the surface of $Pb_{68}Se_{68}$ QD		

Table 3.9. NTOs of selected systems that show some significant contributions

Mode of attachment	Optimized structure	Hole	Electron	1 st energy state, eV
Oxygen molecule at 100				0.36
Oxygen molecule at 110				1.51
Decomposed oxygen molecule at 100				2.20
Oxygen atom at 100				2.23

3.2.6. Conclusions

Our results support experimental observations on how oxygen initially quenches the PL and after a while, there is a recovery of PL. We proposed a mechanistic pathway to this observation. Initially O₂ molecule comes in contact to the surface of QD, introducing surface trap states near the edge of the band gap and causing a red shift in absorption. After close encounter to the

surface, the oxygen molecule dissociates. At this stage, the trap states disappear and an overall blue shift in absorption spectra was observed. NTO plots also support this point, while showing localized orbitals in case of molecular oxygen and delocalized orbitals in case of oxygen atom bound on the surface of QD.

3.3. References

- 1 Koley, G. I. *et al.* Efficient, stable infrared photovoltaics based on solution-cast colloidal quantum dots. *Acs Nano* **2**, 833-840, doi:10.1021/nn800093v (2008).
- 2 Colvin, V. L., Schlamp, M. C. & Alivisatos, A. P. Light-Emitting-Diodes Made from Cadmium Selenide Nanocrystals and a Semiconducting Polymer. *Nature* **370**, 354-357, doi:10.1038/370354a0 (1994).
- 3 Caruge, J. M., Halpert, J. E., Wood, V., Bulovic, V. & Bawendi, M. G. Colloidal quantum-dot light-emitting diodes with metal-oxide charge transport layers. *Nat Photonics* **2**, 247-250, doi:10.1038/nphoton.2008.34 (2008).
- 4 Li, J. J. *et al.* Large-scale synthesis of nearly monodisperse CdSe/CdS core/shell nanocrystals using air-stable reagents via successive ion layer adsorption and reaction. *J Am Chem Soc* **125**, 12567-12575, doi:10.1021/ja0363563 (2003).
- 5 Peng, Z. A. & Peng, X. G. Mechanisms of the shape evolution of CdSe nanocrystals. *J Am Chem Soc* **123**, 1389-1395, doi:10.1021/ja0027766 (2001).
- 6 Liu, W. *et al.* Compact biocompatible quantum dots functionalized for cellular imaging. *J Am Chem Soc* **130**, 1274-1284, doi:10.1021/ja076069p (2008).
- 7 Choi, H. S. *et al.* Renal clearance of quantum dots. *Nat Biotechnol* **25**, 1165-1170, doi:10.1038/nbt1340 (2007).

- 8 Fan, H. Y. *et al.* Surfactant-assisted synthesis of water-soluble and biocompatible semiconductor quantum dot micelles. *Nano Lett* **5**, 645-648, doi:10.1021/nl050017l (2005).
- 9 Majetich, S. A. & Carter, A. C. Surface Effects on the Optical-Properties of Cadmium Selenide Quantum Dots. *J Phys Chem-US* **97**, 8727-8731, doi:Doi 10.1021/J100136a013 (1993).
- 10 Kuno, M., Lee, J. K., Dabbousi, B. O., Mikulec, F. V. & Bawendi, M. G. The band edge luminescence of surface modified CdSe nanocrystallites: Probing the luminescing state. *J Chem Phys* **106**, 9869-9882, doi:Doi 10.1063/1.473875 (1997).
- 11 Liu, I. S. *et al.* Enhancing photoluminescence quenching and photoelectric properties of CdSe quantum dots with hole accepting ligands. *J Mater Chem* **18**, 675-682, doi:10.1039/b715253a (2008).
- 12 Jeong, S. *et al.* Effect of the thiol-thiolate equilibrium on the photophysical properties of aqueous CdSe/ZnS nanocrystal quantum dots. *J Am Chem Soc* **127**, 10126-10127, doi:10.1021/ja042591p (2005).
- 13 Zheng, H., Mortensen, L. J. & DeLouise, L. A. Thiol Antioxidant-Functionalized CdSe/ZnS Quantum Dots: Synthesis, Characterization, Cytotoxicity. *J Biomed Nanotechnol* **9**, 382-392, doi:10.1166/jbn.2013.1561 (2013).
- 14 Frisch, M. J. *et al.* *Gaussian 09*. (Gaussian, Inc., 2009).
- 15 Perdew, J. P., Burke, K. & Ernzerhof, M. Generalized Gradient Approximation Made Simple. *Physical review letters* **77**, 3865-3868 (1996).

- 16 Ernzerhof, M. & Scuseria, G. E. Assessment of the Perdew–Burke–Ernzerhof exchange-correlation functional. *The Journal of Chemical Physics* **110**, 5029-5036, doi:doi:http://dx.doi.org/10.1063/1.478401 (1999).
- 17 Adamo, C. & Barone, V. Toward reliable density functional methods without adjustable parameters: The PBE0 model. *The Journal of Chemical Physics* **110**, 6158-6170, doi:doi:http://dx.doi.org/10.1063/1.478522 (1999).
- 18 Hay, P. J. & Wadt, W. R. Ab initio effective core potentials for molecular calculations. Potentials for K to Au including the outermost core orbitals. *The Journal of Chemical Physics* **82**, 299-310, doi:doi:http://dx.doi.org/10.1063/1.448975 (1985).
- 19 Wadt, W. R. & Hay, P. J. Ab initio effective core potentials for molecular calculations. Potentials for main group elements Na to Bi. *The Journal of Chemical Physics* **82**, 284-298, doi:doi:http://dx.doi.org/10.1063/1.448800 (1985).
- 20 Francl, M. M. *et al.* Self-consistent molecular orbital methods. XXIII. A polarization-type basis set for second-row elements. *The Journal of Chemical Physics* **77**, 3654-3665, doi:doi:http://dx.doi.org/10.1063/1.444267 (1982).
- 21 Hariharan, P. C. & Pople, J. A. The influence of polarization functions on molecular orbital hydrogenation energies. *Theoret. Chim. Acta* **28**, 213-222, doi:10.1007/bf00533485 (1973).
- 22 Cossi, M., Rega, N., Scalmani, G. & Barone, V. Energies, structures, and electronic properties of molecules in solution with the C-PCM solvation model. *Journal of Computational Chemistry* **24**, 669-681, doi:10.1002/jcc.10189 (2003).

- 23 Hedrick, M. M., Mayo, M. L., Badaeva, E. & Kilina, S. First-Principles Studies of the Ground- and Excited-State Properties of Quantum Dots Functionalized by Ru(II)–Polybipyridine. *J. Phy. Chem. C* **117**, 18216-18224, doi:10.1021/jp403819h (2013).
- 24 Fischer, S. A., Crotty, A. M., Kilina, S. V., Ivanov, S. A. & Tretiak, S. Passivating ligand and solvent contributions to the electronic properties of semiconductor nanocrystals. *Nanoscale* **4**, 904-914, doi:10.1039/c2nr11398h (2012).
- 25 Murray, C. B. *et al.* Colloidal synthesis of nanocrystals and nanocrystal superlattices. *Ibm J Res Dev* **45**, 47-56 (2001).
- 26 McDonald, S. A. *et al.* Solution-processed PbS quantum dot infrared photodetectors and photovoltaics. *Nat Mater* **4**, 138-142, doi:10.1038/nmat1299 (2005).
- 27 Steckel, J. S., Coe-Sullivan, S., Bulovic, V. & Bawendi, M. G. 1.3 μm to 1.55 μm tunable electroluminescence from PbSe quantum dots embedded within an organic device. *Adv Mater* **15**, 1862-1866, doi:10.1002/adma.200305449 (2003).
- 28 Luther, J. M. *et al.* Structural, optical and electrical properties of self-assembled films of PbSe nanocrystals treated with 1,2-ethanedithiol. *ACS Nano* **2**, 271-280, doi:10.1021/nn7003348 (2008).
- 29 Sykora, M. *et al.* Effect of Air Exposure on Surface Properties, Electronic Structure, and Carrier Relaxation in PbSe Nanocrystals. *ACS Nano* **4**, 2021-2034, doi:10.1021/nn100131w (2010).
- 30 Dai, Q. Q. *et al.* Stability Study of PbSe Semiconductor Nanocrystals over Concentration, Size, Atmosphere, and Light Exposure. *Langmuir* **25**, 12320-12324, doi:10.1021/la9015614 (2009).

- 31 Kilina, S. V., Kilin, D. S., Prezhdo, V. V. & Prezhdo, O. V. Theoretical Study of Electron–Phonon Relaxation in PbSe and CdSe Quantum Dots: Evidence for Phonon Memory. *J. Phy. Chem. C* **115**, 21641-21651, doi:10.1021/jp206594e (2011).
- 32 Kilina, S. V., Kilin, D. S. & Prezhdo, O. V. Breaking the Phonon Bottleneck in PbSe and CdSe Quantum Dots: Time-Domain Density Functional Theory of Charge Carrier Relaxation. *ACS Nano* **3**, 93-99, doi:10.1021/nn800674n (2009).

4. EFFECT OF LIGANDS PASSIVATED QUANTUM DOT – QUANTUM DOT INTERACTIONS ON THEIR OPTOELECTRONIC PROPERTIES

In this chapter, we present the study of electronic and optical properties of interacting QDs. Particles interactions lead to the formation of either closely packed quantum dots or two dimensional (2D) nanoplates. Each of these nanoparticles have their own significance and applications in solar cells and LEDs. This chapter is subdivided into two chapters, namely, 4.1 and 4.2.

In chapter 4.1, we report quantum mechanical studies to investigate how interactions between closely packed defects induced silicon quantum dots passivated with methyl (CH_3) ligands can influence the photoluminescence (PL) stability through rapid exciton energy transfer from optically active (bright) states of a non-defective quantum dot to a surface trap state of its neighboring defective quantum dot.

In chapter 4.2, we report our DFT studies and provided insights into the formation of two-dimensional (2-D) PbSe nanoplatelets via oriented attachment based on ligand engineering of surface chemistry in their crystal growth. We show that halide passivation is critical in the growth of the (100) facet-dominant 2-D nanostructures.

4.1. Enhanced Luminescent Stability through Particle Interactions in Silicon Nanocrystal Aggregates

4.1.1. Introduction

Silicon nanocrystals (SiNCs) have been demonstrated as potential materials in applications such as bioimaging and sensing,¹ especially because of their non-toxicity nature and earthly abundancy. These materials are also known for their tunable PL efficiency across the visible to near-infrared regions. However, there are a number of unresolved questions related to the role of surface states,² the interplay of quantum confinement and the indirect band gap of silicon,³ and the impact of particle interactions in closely packed assemblies on PL.⁴ In terms of latter, it has been reported that close-packed assemblies of ligand-passivated colloidal nanocrystals can exhibit enhanced PL stability, but the origin of this effect is unclear.⁵

A fundamental understanding of such phenomena must start with the smallest distinct element: the emission from an individual nanocrystal. Like all fluorophores, semiconductor nanocrystals exhibit fluorescence intermittency or “blinking”, whereby the PL randomly switches between bright (on) and dark (off) states.⁶

In a tight collaboration with experimental group from Prof. Erik Hobbie, we performed DFT simulations to examine the influence of inter particle interactions on the PL stability of silicon nanocrystal aggregates.

From their experimental results, it was found that, in case of monodispersed 4 nm sized SiNCs, in contrast to the behavior typically exhibited by the metal chalcogenides, the measured PL stability shows an enhancement with respect to the non-interacting scenario with increasing aggregate size. Additionally, they found that on-time blinking is more compared to that of off-time blinking. Moreover, size disparity reduced this collective enhancement in PL. To

investigate this phenomenon and give insights to the above mentioned experimental observations, we performed computations on three different sized Silicon QDs.

4.1.2. Computational Details

4.1.2.1. Structural Models and Their Optimization

The SiNCs were modeled as silicon QD with a bulk-diamond structure. We consider 29 Si atoms (1.2 nm diameter), 35 Si (1.35 nm diameter) and 66 Si (1.6 nm diameter). Methyl (CH_3) ligands were covalently bonded to the surface Si atoms to passivate dangling bonds. The charged and neutral, fully passivated nanocrystals (denoted F) were optimized at the DFT level using the PBE1PBE⁷ functional and the 6-31g*⁸ basis set implemented in Gaussian-09.⁹ We have also simulated structures with a surface defect, which is modeled by removing a methane group from nearest two 3-coordinated Si ions (denoted as L), and then optimizing geometry in the same way as for the fully passivated structures. The optimized structures of fully passivated (F) Si₂₉ and with a surface defect (L) are shown in Figure 1(a). Charged structures with -2 or +2 charge and full passivation (F²⁻) and with surface defects (L²⁺ and L²⁻) are also optimized holding even number of electrons to maintain the close shell configuration.

4.1.2.2. Absorption Spectra

Absorption spectra were calculated for all optimized structures within linear response using time-dependent density functional theory (TDDFT) with the same functional and basis set used in the ground state calculations. For each absorption spectrum, the first 100 excited states were calculated and a Gaussian line width of 0.08 eV was used to reproduce the inhomogeneous broadening of experimental spectra. Natural transition orbitals (NTOs)¹⁰ were used to study the localization/delocalization properties of the excited-state electron density.

All calculations were conducted in vacuum. Although the inclusion of polar media (e.g., solvent) via CPCM increases the oscillator strengths of the optical transitions, it does not change the shape/energy of spectral peaks for fully passivated SiNCs and results in a uniform blue shift (0.5 eV) of the SiNCs spectra with defects. Because the experimental measurements are performed in an N₂ atmosphere, the effect of a polar solvent is thus neglected.

4.1.2.3. Förster Resonance Energy Transfer

Förster resonance energy transfer is a phenomenon in which an energy transfer takes place between donor and acceptor fluorophores through non-radiative dipole-dipole coupling, provided they both positioned in between 1-10 nm apart. For this process to occur, emission of donor must be in resonance with absorption of acceptor. Typically, in experiments, the efficiency of these rates is proportional to $1/r^6$, where r being the distance between the two chromophores.

Theoretically, in this work, the energy transfer rates were calculated between pairs (donor/acceptor) of structurally similar and different SiNCs based on the transition density matrix obtained from their TDDFT calculations using a FRET code generated at LANL. This approach goes beyond dipole-dipole coupling to include all multipole contributions.

4.1.3. Results and Discussions

The optimized QD structures of 29 Si atoms passivated by methyl ligands in both F and L forms are shown in Figure 4.1. Similarly, other sized QDs, with 35 Si atoms and 66 Si atoms were also optimized and the information about homo lumo gap is shown in Table 4.1. From the data, it can be seen that these structures follow size confinement effect very well.

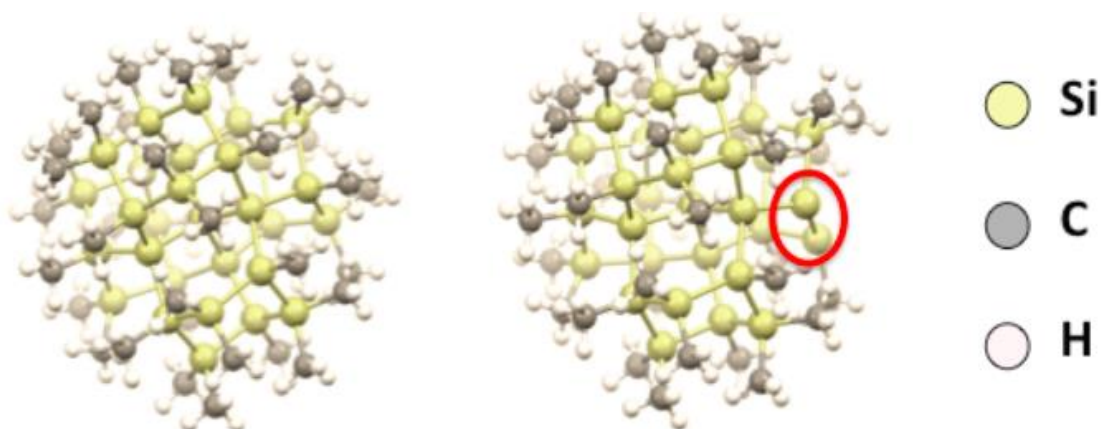


Figure 4.1. Optimized structures of fully passivated (F) and ligands removed (L) Silicon QDs.

Table 4.1. Size confinement effect in Si QDs

System	HOMO LUMO GAP	
	Si 29	Si 35
F	4.88	4.76
F ²⁻	1.48	1.35
L	2.56	3.11
L ²⁻	1.95	1.93
L ²⁺	2.76	1.94

After optimization in neutral and charge (± 2), we have calculated density of states (DOS) of each of these systems and the plotted shown in Figure 4.2 and Figure 4.3. The plots reveal an important observation that in presence of charge (± 2), both F and L introduce new mid-gap states. For the charged systems, there is either an occupied, hole, (-2 charge) or an unoccupied, electron, (+2) trap states, while both electron and hole trap states appear in the gap of the neutral structure with the surface defect. To further assess the effect of these states on absorption, TDDFT calculations were performed.

Density Of States of Si_QD with ligands fully covered

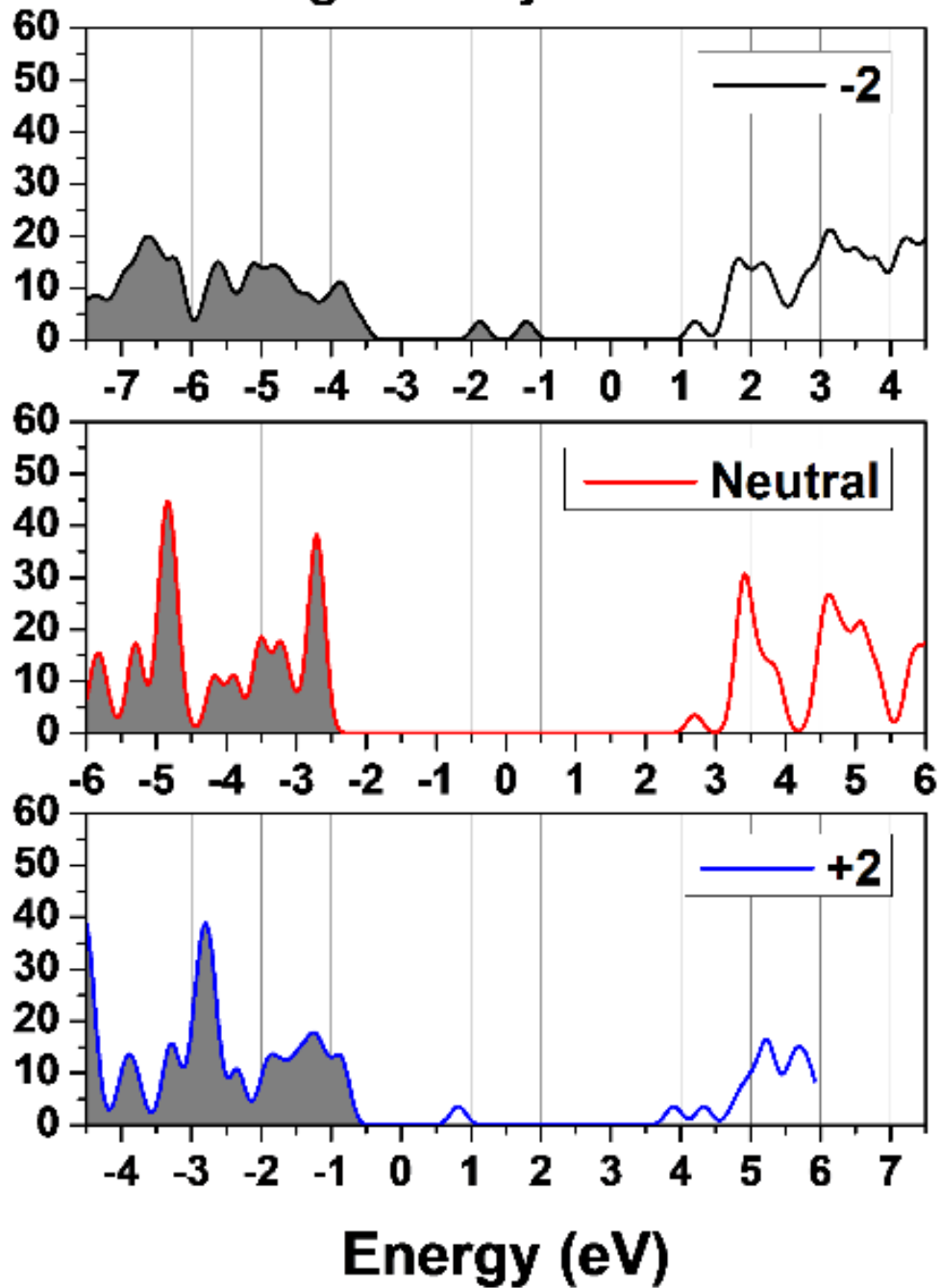


Figure 4.2. Density of states of fully passivated Si QD (F) in neutral and charged systems

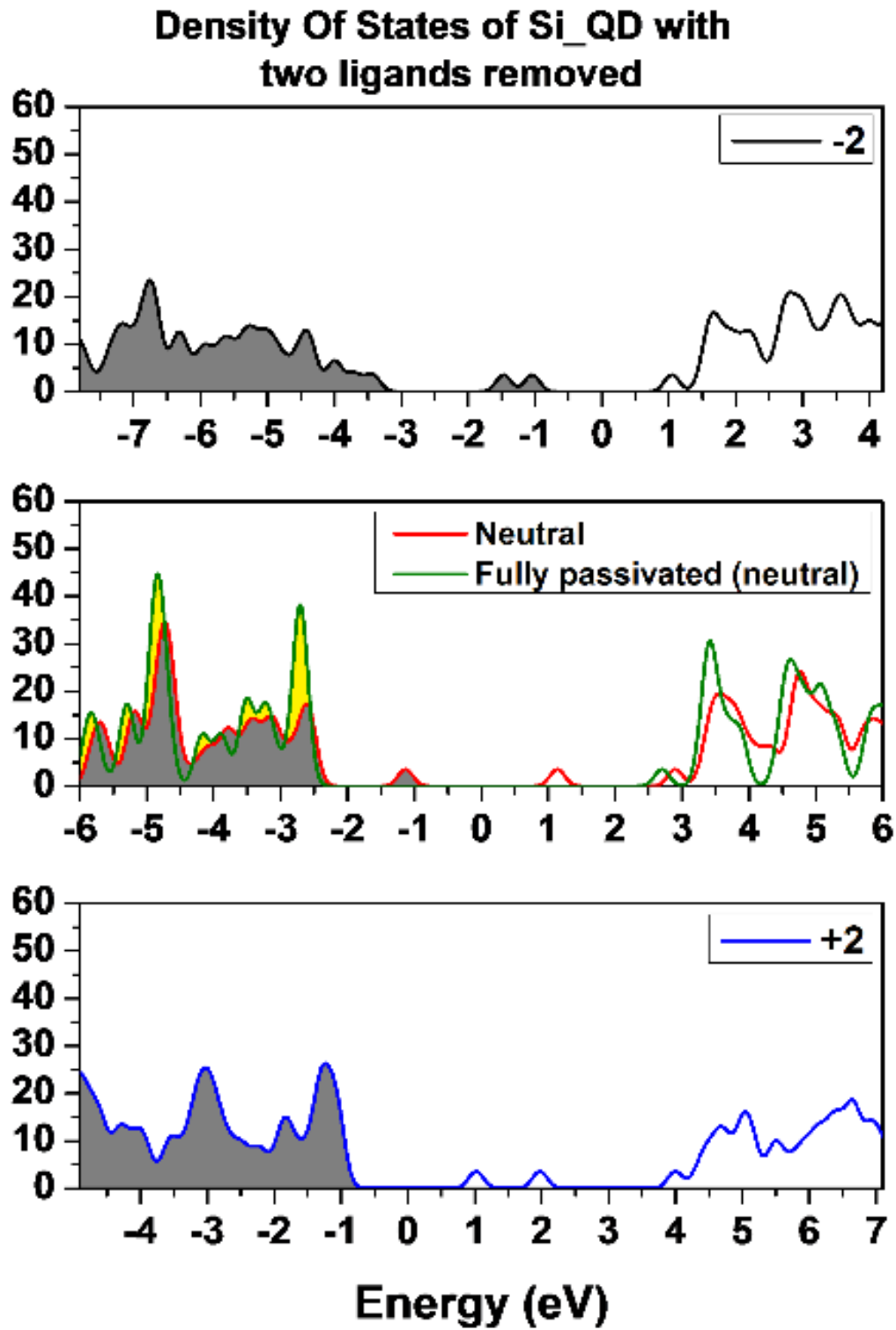


Figure 4.3. Density of states of two ligands removed Si QD (L) in neutral and charged systems

Surprisingly, transitions between these trap states are not completely optically forbidden resulting in manifold of semi bright red-shifted transitions with non-zero oscillator strengths at the energy range of 0.5-4 eV. Not dark nature of mid gap states is the most pronounced for charged small Si₂₉ clusters, Figure 2 (top two panels). Semi-bright character of these transitions originates from a strong confinement that delocalizes the charge over the entire QD, as can be seen from NTOs contributing to the lowest energy transition shown in Table 4.2 (the left panel). Surface defects result in some localization of the charge density near the Si site with lost ligands, resulting in weaker oscillator strength as compared to the charged fully passivated structure F²⁻. Increase in the QD size leads to noticeable localization of NTOs for charged systems and systems with surface defects; so that the lowest-energy transitions become optically dark for Si₃₅ (Table 4.2).

The energy transfer rates between two neighboring QDs separated by a fixed distance depend on three factors: the value of the transition dipole moment for donor's and acceptor's state, the density of states of the acceptor at the energy range of the excitation of the donor, and the resonance conditions between the donor's and acceptor's energies. If all three factors are optimal, the FRET rate is the largest. Indeed, these conditions are satisfied when the donor and acceptor have the same structure. Therefore, the rates are the largest for the same pairs of Si₃₅ and Si₂₉ QDs, as depicted in most cases in Figure 3, while the absolute values of rates are just slightly fluctuating with the QD size and a presence of the surface defect and the charge, staying in the range of 0.27-0.4 ns⁻¹ (3-4 ns), when the donor is excited at the energies of 2.4-3 eV (Figure 4.5.a) and 0.13-0.23 ns⁻¹ (4-8 ns), when the donor is excited at the brightest energy state in the range of 4.0- 5.0 eV (Figure 4.5.b).

However, the interplay between each of these factors is also important. For example, the rates are slightly larger for the energy transition between the donor Si35 with a surface defect (35L) and the same size QD but with ideal passivation (35F) (Figure 4.5.b). This is because both QDs have the excitation energies in resonance (see the absorption peaks at 4.7 eV for 35L and 35F in Figure 4.4, top panel), while the acceptor has larger transition dipole moment at this energy range than the donor QD with a surface defect. Similarly, energy transitions between photo excited Si35 with a surface defect (35L) to Si29 with a surface defect and negative charge (29L²⁻) are the largest due to higher oscillator strength of several transitions at the excitation energy range of 2.4-3 eV combined with significantly larger density of states of the acceptor at this energy range (see Figure 2, top and middle panels). With a few exceptions, the energy transition rate from different size QDs is smaller than for the same size QDs. This trend is the most pronounced in the narrow excitation window, Figure 3(b), with energy transfer time changing from 5 ns to 30 ns for smaller donor (Si29) to larger acceptor (Si35) and from 3 ns to 20 ns for larger donor (Si35) to smaller acceptor (Si29).

Although the calculated energy transfer (3-30 ns) are much slower than typical rates of the phonon-induced relaxation rates in QDs (~1-100 ps), it is fast enough to happen before photoluminescence (PL) takes place. Note that energy transfer is found to be efficient even for states with low oscillator strengths (semi-dark trap states) happening during 10-15 ns. This provides additional channel for occupation of the lowest-laying trap states with dark or semi-dark optical character in the neighboring QDs. For phonon-induced relaxation, energy transfer thus facilitates the occupation of non-radiative trap states, which would increase the stability of PL from optically bright states associated with the nanocrystal core. This, in turn, would lead to

an increase in the average on time for densely packed SiNCs ensembles as illustrated in Figure 1 (b), consistent with the experiments.

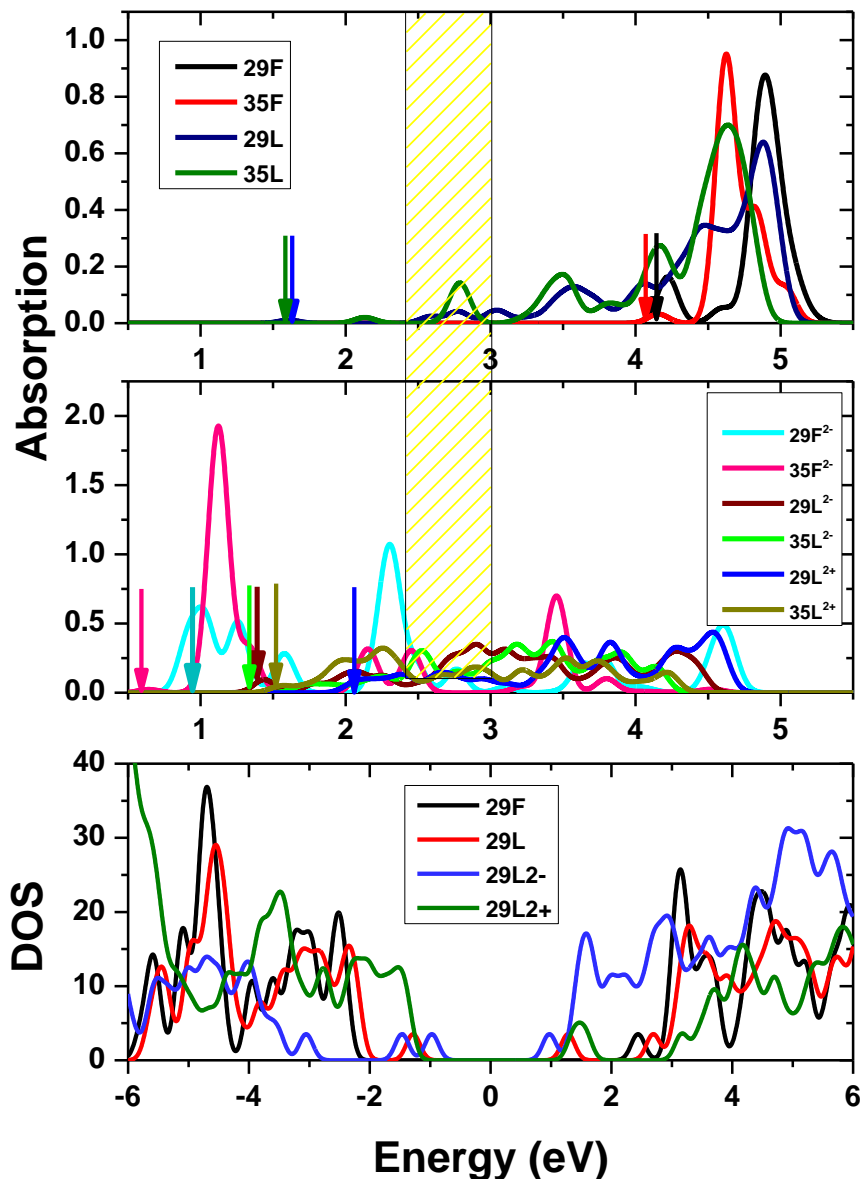


Figure 4.4. Calculated ground and excited state electronic structure of methane passivated Si29 and Si35. Top and middle panels represent absorption spectra of neutral fully passivated (F) and with two lost ligands (L) Si clusters (top) and F and L clusters with -2 and +2 charge. The vertical arrows define the lowest-energy transitions. The highlighted pattern represents excitation energy range of 2.4 - 3.0 eV, corresponding to the donor. Bottom panel represents the ground state density of states (DOS) of the neutral and charged Si29 QD with full passivation (F) and with defects in the passivation (L).

Table 4.2. Natural transition orbitals (NTOs) contributing to the first excited state of the neutral and charged Si29 and Si35 QDs with methane passivation. The arrows mark the location of the surface defect, e.g., the Si ion from which two ligands are lost (L).

	Si-29		Si-35	
	HOLE	ELECTRON	HOLE	ELECTRON
F	E = 4.1088 eV, $f = 0.0002$		E = 4.0351 eV, $f = 0.0000$	
F²⁻	E = 0.9114 eV, $f = 0.0218$		E = 0.6382 eV, $f = 0.0014$	
L	E = 1.6089 eV, $f = 0.0019$		E = 2.1332 eV, $f = 0.0036$	
L²⁻	E = 1.4383 eV, $f = 0.0168$		E = 1.4020 eV, $f = 0.0004$	
L²⁺	E = 2.0426 eV, $f = 0.0086$		E = 1.4806 eV, $f = 0.0006$	

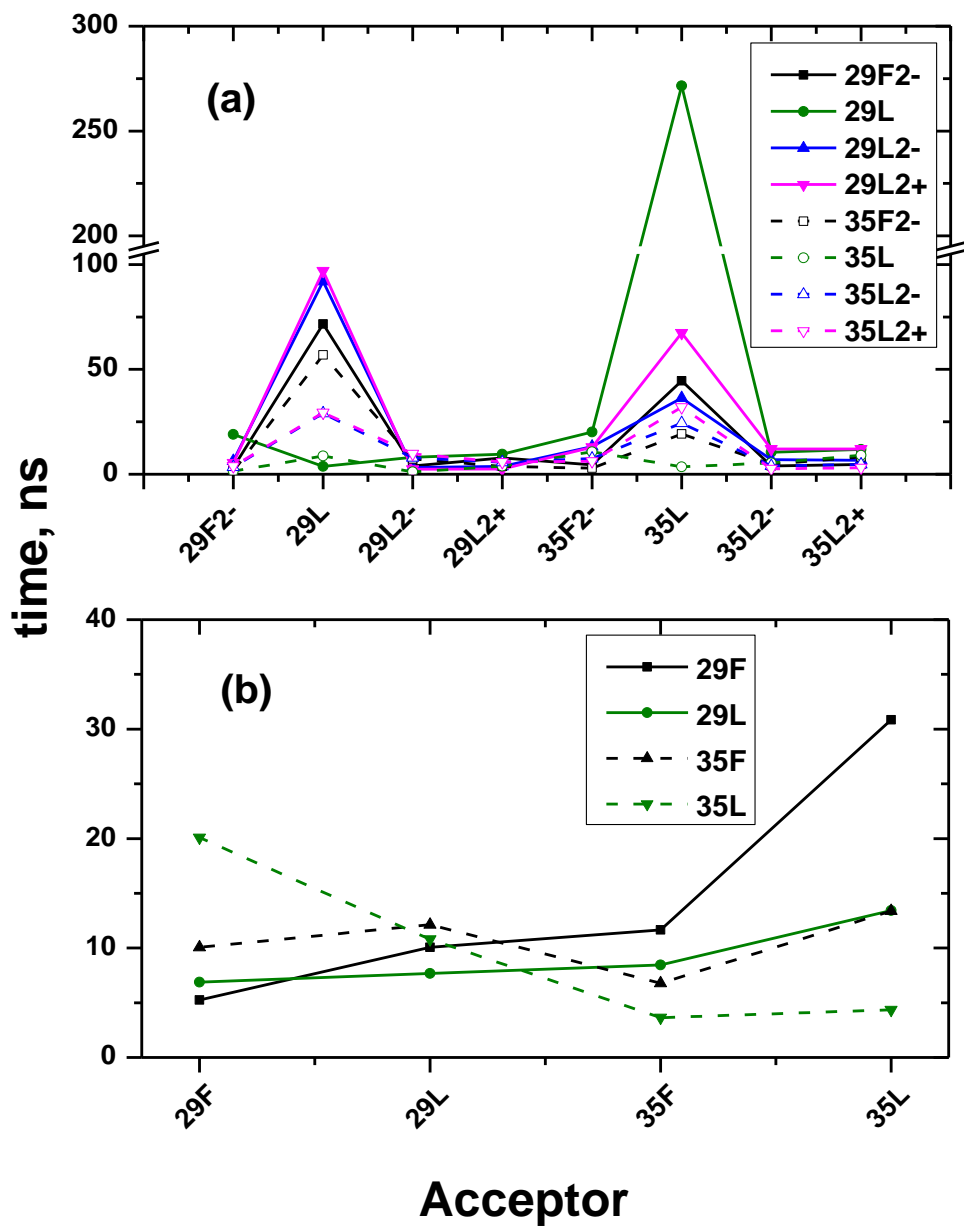


Figure 4.5. The Forster energy transfer times between two methane passivated Si29 and Si35 QDs separated by the distance of ~1 nm. (a) The donor QD is excited at the range of 2.4 to 3.0 eV (marked by yellow pattern in Figure 2). (b) The donor QD is excited to the brightest state in the range of 4 - 5 eV. X-axis represents the acceptor QD with the same or different size and structure as compared to a donor. For both panels, solid lines correspond to the donor QD of a small size (Si29), while dashed lines correspond to the donor QD of the larger size (Si35).

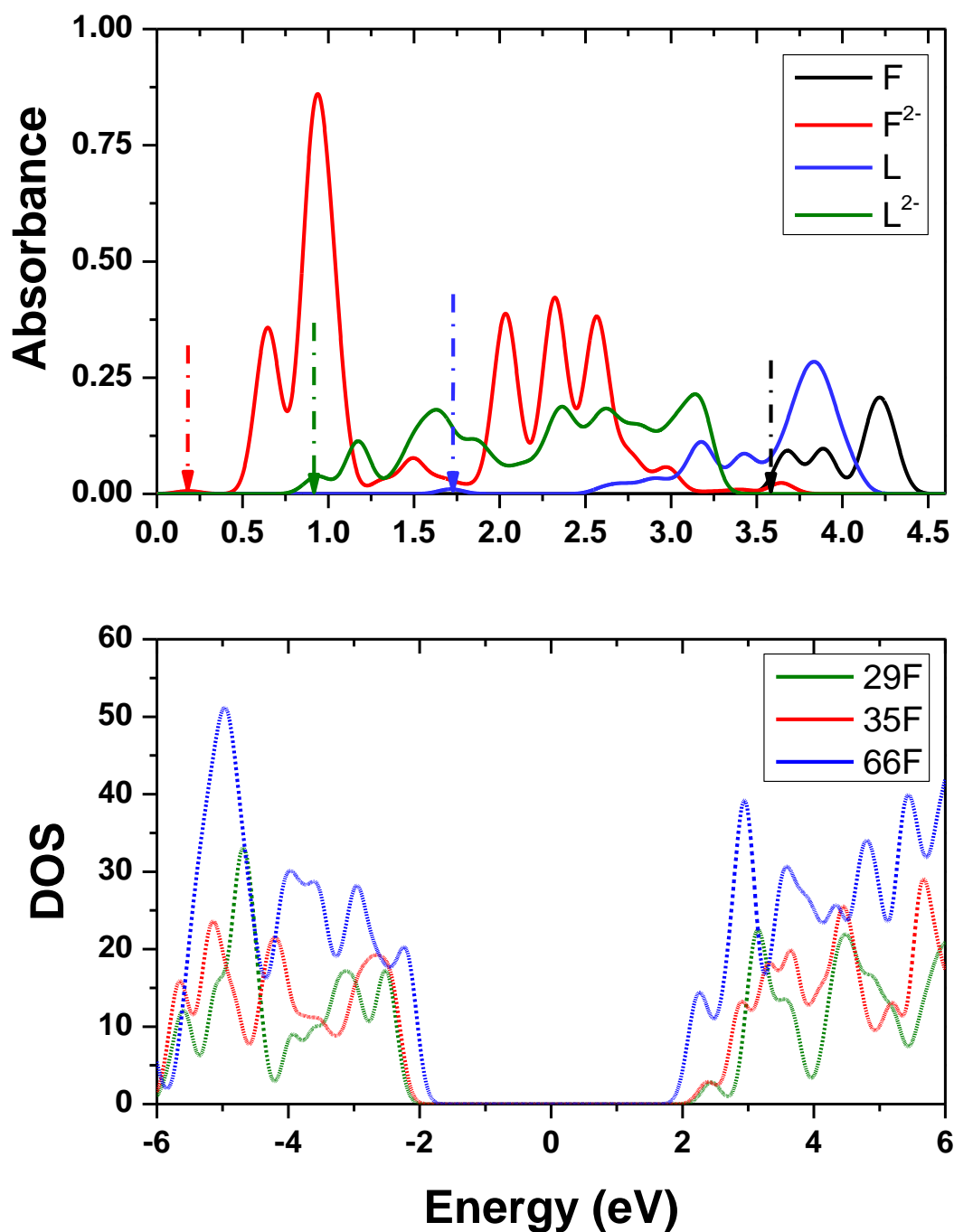


Figure 4.6. Top panel represents absorption spectra of the neutral and charged Si₆₆ QD with full passivation by methane ligands (F) and with two ligands lost (L) from the Si ion on the surface. Bottom panel represents Density of States (DOS) of neutral fully passivated Si₆₆, Si₃₅, Si₂₉ QDs. The confinement effect is well seen: the larger the QD, the smaller the gap.

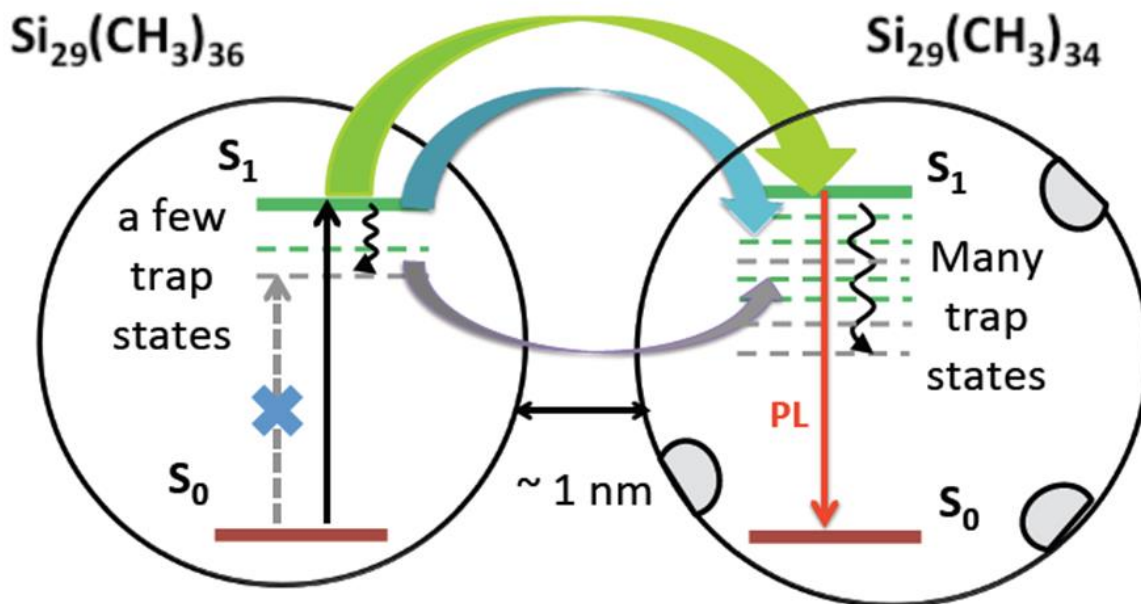


Figure 4.7. Possible pathways for an exciton transfer (also called the energy transfer) between neighboring Si nanocrystals; the size of bold arrows qualitatively correspond to rates of the energy transfer. Left structures have no surface defects resulted in less number of optically dark (grey dashed lines) and semi-dark (dashed green lines) lowest-energy trap states. Right structures have surface defects, e.g., lost ligands from Si sites, marked by the grey ovals.

In Figure 4.7, optical excitation from the ground state (S_0) to the first bright state (S_1) is defined by the vertical black arrow, while transitions to semi-dark and dark trap states are marked by the vertical dashed grey lines. Photoluminescence (PL) is shown by a red vertical arrow. The wavy black arrow illustrates phonon-induced relaxation of an excitation to the lowest states. Both exciton transfer and exciton relaxation govern fast population of the lower-energy trap states, so that PL takes place from higher energy states with stronger oscillator strengths, thus enhancing PL emission as observed in experimental results.

The lifetime of the lowest excited state was calculated using the Einstein coefficients for spontaneous emission based on the oscillator strength and wavelength (nm) of these transitions as obtained from time-dependent DFT calculations (Table 4.3).

Table 4.3. The lifetime of the lowest excited state was calculated using the Einstein coefficients for spontaneous emission

QD	System	wavelength, nm	O.S.	Life time, ns
Si-29	F	293.73	0.0096	85
	F ²⁻	1360.38	0.0218	797
	L	446.79	0.0071	265
	L ²⁻	862.01	0.0168	417
	L ²⁺	516.09	0.0118	213

FRET calculations approaches were performed considering only dipole-dipole approximations and compared with rates obtained by including all contributions to understand the importance of higher order multipolar contributions. As shown in Figure 4.8, for the distances in range of 1-3 nm, multipole contributions are quite important, whereas those contributions were found negligible at long distances. In this plot, FRET rate of all contributions (solid) and in the dipole approximations (dashed) between methane passivated Si29 as a function of separation from 0.1 nm to 10 nm. The donor is excited at the brightest energy from 4.7-to-4.9 eV and the acceptor is scanned over the entire range (from 1-to-5 eV). The horizontal axis is the end-to-end distance between Si29 nanocrystals and vertical axis the transfer time. F denotes fully passivated and L is with two ligands removed.

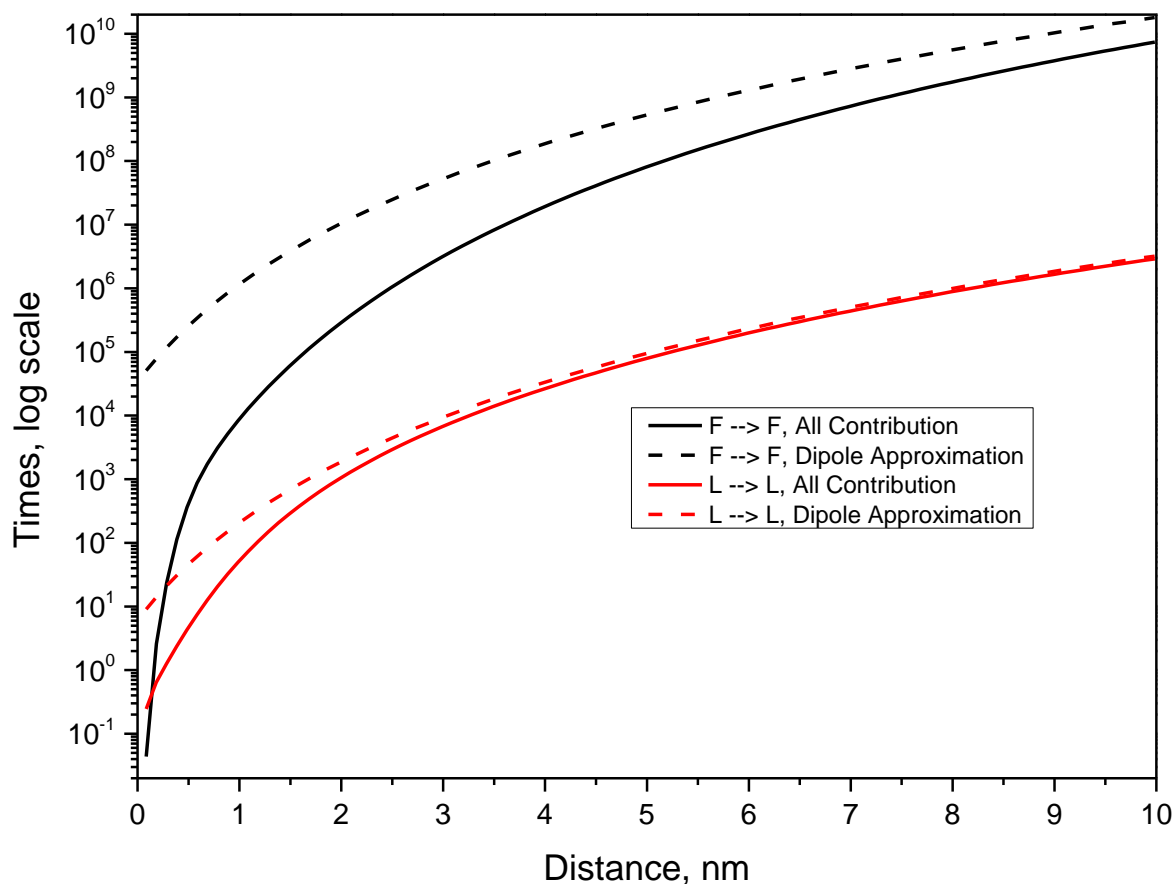


Figure 4.8. FRET rate of all contributions (solid) and in the dipole approximations (dashed) between methane passivated Si29 as a function of separation from 0.1 nm to 10 nm.

4.1.4. Conclusions

In conclusion, using DFT studies, we have shown that in presence of charge (± 2), both F and L introduce new mid-gap states. For the charged systems, there is either an occupied, hole, (-2 charge) or an unoccupied, electron, (+2) trap states, while both electron and hole trap states appear in the gap of the neutral structure with the surface defect. Our FRET results suggest that rapid energy transfer from “bright” nanocrystals to “dark” trap states in nearest-neighbors can efficiently fill such trap states and improve the stability of aggregate emission.

4.2. Deeper Understanding of Surface Chemistry in Engineering Oriented Attachment in the Formation of Two Dimensional PbSe Nanoplates

4.2.1. Introduction

Colloidal synthesis methods are used to produce semiconductor nanocrystals of a wide range of materials because they offer excellent control over particle size. For a given composition, fine control over the size of semiconductor nanocrystals within the quantum confinement regime, or quantum dots, gives one the ability to tune the band gap. More recently, attention has increasingly turned to modifying synthesis conditions to allow control over nanocrystal shape. Specifically, achieving particles of controlled dimensionality offers additional means for higher-level manipulation of the optical properties of nanostructures, including dynamical behavior. Colloidally prepared “zero-dimensional” (0-D) quantum dots (QDs)¹¹ and quasi-one-dimensional (1-D) nanorods¹² both often exhibit high photoluminescence (PL) efficiencies, but in the latter case, tuning of the band gap can be accomplished by restricting the particle size in only two dimensions. In this case, elongation in the third, unrestrained dimension (nanorod length) can be used to alter charge carrier recombination and cooling processes within the nanoparticle, substantially impacting the efficiencies of multi-exciton Auger recombination and “carrier multiplication”. Such effects are potentially even greater in quasi-two-dimensional (2D) nanostructures such as nanoribbons and nanoplatelets (NPLs)¹³, wherein size tunability is provided by quantum confinement in only one dimension. Indeed, colloidal 2D nanostructures have recently been shown to offer efficient, very narrow emission, tunable as a function of thickness, but also unique carrier cooling dynamics¹⁴ and reduced Auger recombination efficiencies.¹⁵

2D nanostructures of lead chalcogenides, particularly of PbSe, are attractive for use in nanocrystal solar cells and infrared lasers. Although most QD-based solar cells to date have been based on PbS QDs¹⁶, PbSe QDs exhibit markedly higher efficiencies of carrier multiplication¹⁷, as has been demonstrated in PbSe QD solar cells with quantum efficiencies greater than unity.¹⁸ Enhanced carrier multiplication¹⁹ in 2D PbSe nanostructures can be expected to allow even higher efficiencies; additionally, reduced Auger recombination efficiency and high absorption cross-sections should translate into low-threshold lasing at infrared wavelengths of importance to telecommunications²⁰ and remote sensing.²¹

However, development of colloidal syntheses of 2D nanostructures of PbSe has lagged those of II-VI materials considerably. PbS nanosheets formed by oriented attachment of QDs, in a manner related to the synthesis of PbS nanowires and nanorods exhibit thickness-dependent PL,²² and reasonably efficient carrier multiplication.²³ Similar methods have been used to create PbSe nanosheets, but without determinant control over thickness or discernible PL.²⁴ In these reports, long-chain amines or oleates have been shown playing a critical role in formation of 2-D nanostructures oriented along (110) crystal lattice direction, which is supposed to be more reactive than the (100) surface of PbS or PbSe QDs.

In this project, we worked in collaboration with experimental group of Victor Klimov from Los Alamos National Lab, to investigate the interactions between quantum dots to provide insights into the chemical engineering of self-assembling of PbSe QDs into 2-D nanoplates. In their experiments, they could synthesize PbSe nanoplates exclusively growing in (100) direction at a fixed thickness of 2 nm, when an excess of PbCl₂ precursor was used, which was confirmed by analyzing their samples using high resolution transmission electron microscopy (HRTEM) as shown in Figure 4.9. They did not observe such nanoplates formation when PbI₂ was used as

precursor. However, when PbI_2 in combination with excess of Cl^- ion was used, they could get 4 nm and 6 nm thickness nanoplates. We performed DFT studies to give insights to the experimental observations and reasons for the exclusive formation of (100) directed nanoplates. In this regard, our main focus is to understand the role of halide ligands in the formation of nanoplates.

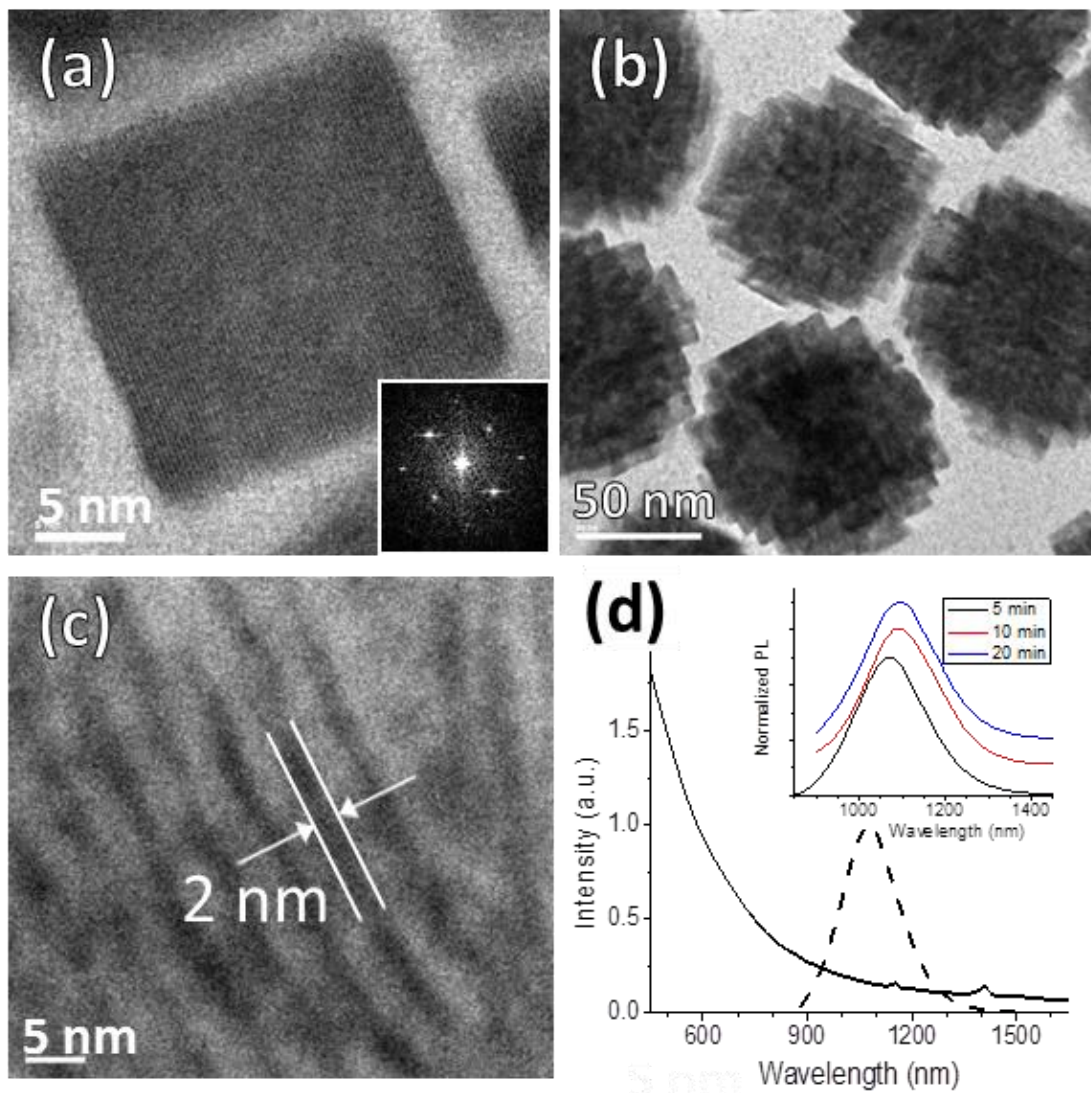


Figure 4.9. (a) HR-TEM image of PbSe NPL synthesized using PbCl_2 precursor. Inset: a selective area electron diffraction pattern, verifying the rock-salt crystal structure. (b) Top-down and (c) side-on TEM images of face-to-face stacks of NPLs (d) Absorption (solid) and PL (dashed) spectra of NPLs synthesized using PbCl_2 . Inset: The PL spectrum redshifts slightly as QDs attach into NPLs, then remains constant.²⁵

4.2.2. Computational Details

4.2.2.1. Gaussian Calculations of Isolated QDs with Ligand Passivation

The NCs we simulated are magic sized $(\text{PbSe})_{16}$ and $(\text{PbSe})_{68}$ clusters with diameters of about 1 nm and 1.8 nm, respectively, constructed based on a rock-salt lattice with bulk Pb-Se bonds, as described elsewhere.²⁶ The Cl, PbCl_2 , and amine ligands such as CH_3NH_2 are initially placed at the (100), (111), or (110) surfaces at distances typical for Pb-Cl and Pb-N bond lengths. All structures are then optimized to their lowest-energy configurations using the Gaussian-09⁹ suite of quantum chemical programs. We have utilized PBE1PBE²⁷ functional with LANL2DZ²⁸ basis set for heavier atoms (Pb, Se, I) and 6-31g*⁸ for rest of the atoms. Selected systems were also optimized in propyl amine solvent, which was used in the relevant addition to energetically optimized vacuum calculations, the resulting geometries of several experimental studies. Solvent effects were simulated using the conductor-like polarizable continuum model (CPCM)²⁹ with the appropriate dielectric constant, as incorporated in the Gaussian-09 software package. The NC-ligand binding energies per ligand are calculated as the energy difference between the NC functionalized by the particular ligands and the isolated NC and the ligand and then divided by the number of ligands passivating the surface.

4.2.2.2. VASP Calculations of 1-D, 2-D and 3-D QD-based Supersolids

In order to model the structures of nanoplates, we have performed our optimizations using the VASP code³⁰ which is particularly efficient for semiconductor crystals and surfaces. Explicitly, we have utilized the Perdew, Burke and Ernzerhof (PBE) functional⁷ and plane-wave basis sets³¹ within PAW pseudopotentials³² for these calculations, as this methodology is found to be efficient for optimizing PbSe QDs³³, published elsewhere. Moreover, here we are interested in just optimizing the structures and are not studying their electronic structure, thus the chosen

methodology is sufficiently enough. This is even supported by comparing the bond parameters of isolated 'PbCl₂ passivated (PbSe)₆₈' structures optimized from Gaussian and VASP methods. We found that there was only about ~ 1-3% change in bond lengths of Pb-Se and Pb-Cl between the structures obtained from these two different methodologies. However, when (PbSe)₆₈ bare QDs structures obtained from VASP were compared to bulk crystal, the bond lengths of Pb-Se in the core are within ~1% error, whereas the surface Pb-Se atoms bond lengths in optimized structures are reduced to about 4% compared to the bulk crystal. This is a typical behavior of the optimization as the surface atoms valencies are not completely satisfied.

Periodic boundary conditions (PBC) were applied between the quantum dots to form 0-, 2- and 3-Dimensional structures. For modeling 0-D QD, it is surrounded by vacuum of about a diameter of QD in all three directions, 2-D structures were obtained by applying PBC in such a way that each QD is about 3Å apart from each other in 2 directions, placing a vacuum (about a QDs diameter) on the third direction and 3-D structures were obtained by applying PBC in such a way that each QD is about 3Å apart in all three directions. The main reason behind placing them 3Å apart is because the actual bond length between Pb and Se is about 2.9-3.0Å. Electronic relaxations were performed until a threshold of 10⁻⁵ eV was reached while the ionic relaxations were performed until a threshold of 10⁻² eV/Å was reached and energy cutoff of 300 eV was set in each of these calculations. A mesh of 1x1x1 Monkhorst-Pack grid³¹ was used to sample the Brillouin zone. Other meshes like 6x6x6 and 6x6x1 were used in simulating 3D and 2D cases, respectively, but found that there is no substantial difference in the total energy values and were time consuming. Thus, the results shown here in the dissertation were obtained using 1x1x1 mesh (gamma-point) grids for consistency.

4.2.2.3. Calculations of the Surface Energy

A generalized scheme describing different surfaces on PbSe quantum dot is shown in Figure 4.11. A quantum dot comprises of 6 surfaces in (100), 12 surfaces in (110), 4 of lead terminated and 4 of selenium terminated surfaces in (111) directions.

In the following example (PbSe)₆₈ passivated by 12 of PbCl₂ ligands at (110) sites is illustrated below on how to calculate the surface energy of the quantum dots in presence of ligands (idea was adapted from a published paper).³⁴ The surface energy value of γ_{110}^{bare} denotes the stability of bare (PbSe)₆₈ quantum dots surface with miller index 110, can be calculated using Eq. (4.1) as follows:

$$\gamma_{110}^{bare} = \frac{1}{12 A_{110}} (E_{0D/bare} - 24E_{Pb} - 24E_{Se}) \quad (4.1)$$

Here number 12 represents number of 110 sites on (PbSe)₆₈ quantum dot; A₁₁₀ is the surface area of 110; E_{0D/bare}, E_{Pb} and E_{Se} represent the energy of the optimized bare quantum dot, the energy of lead atom and the energy of Se atom respectively. As shown in Figure 4.10, each of 110 sites contains 2 of Pb atoms and 2 of Se atoms. For all 12 available (110) surfaces, a total of 24 Pb and 24 Se atoms are involved in binding with ligands

Surface energy for the formation of 2D plate of (PbSe)₆₈ quantum dot along 100, passivated by PbCl₂ at 110 sites, denoted by $\gamma_{PbCl_2}^{2D}$, can be calculated as follows:

$$\gamma_{PbCl_2}^{2D} = \frac{1}{4 A_{100}} (E_{2D/(QD-PbCl_2)} - 32E_{Pb} - 24E_{Se} - 16E_{Cl}) \quad (4.2)$$

Where number '4' represents the QD growing in x, x', y and y' directions, E_{2D/(QD-PbCl₂)} is the energy of 2D plate growing along x, x', y and y', constructed by passivating PbCl₂ at 110 surface and E_{Cl} is the energy of Cl atom respectively. As shown in Figure 4.10, each of 100 sites contains 6 of Pb atoms and 6 of Se atoms of quantum dot, 4 of Pb atoms of ligand and 8 of

Chlorine atoms of ligand. For the 4 surfaces, a total of $8 * 4 = 32$ Pb (6 Pb of quantum dot and 4 Pb of ligand each shared by an adjacent dot = $4 / 2 = 2$ Pb), 24 Se and 16 Cl atoms are involved in 2D plate formation.

Surface energy for the formation of 3D box of $(PbSe)_{68}$ quantum dot along 100, passivated by $PbCl_2$ at 110 sites, denoted by $\gamma_{PbCl_2}^{3D}$, can be calculated as follows:

$$\gamma_{PbCl_2}^{3D} = \frac{1}{2 (A_{xy} + A_{yz} + A_{zx})_{100}} (E_{3D/(QD-PbCl_2)} - 48E_{Pb} - 36E_{Se} - 24E_{Cl}) \quad (4.3)$$

Where number ' $2(A_{xy} + A_{yz} + A_{zx})$ ' represents area of the quantum dot covered in all six directions, $E_{3D/(QD-PbCl_2)}$ is energy of 3D box. As shown in Figure 4.10, each of 100 sites contains 10 of Pb atoms, 6 of Se atoms and 8 of Chlorine atoms. For the 6 surfaces, a total of $8 * 6 = 48$ Pb (6 Pb of quantum dot and 4 Pb of ligand each shared by an adjacent dot = $4 / 2 = 2$ Pb), 36 Se and 24 Cl atoms are involved in 3D box formation.

For calculating the surface energy for amines to attach on 100, following formula is used:

$$\gamma_{100}^{amines} = \frac{1}{2 A_{100}} (E_{0D/QD-PbCl_2} - 20E_{Pb} - 12E_{Se} - 16E_{Cl}) \quad (4.4)$$

Where, $E_{0D/QD-PbCl_2}$ is the energy of 0 dimensional QD covered with $PbCl_2$ at 110. The factor '2' represents that amines are covered on 2 surfaces.

As shown in Figure 4.10, each of 100 sites contains 10 of Pb atoms, 6 of Se atoms and 8 of Chlorine atoms. For the 2 surfaces covered by amines, a total of 20 Pb, 12 Se and 16 Cl atoms are involved in amines binding to $PbSe+PbCl_2$ QD.

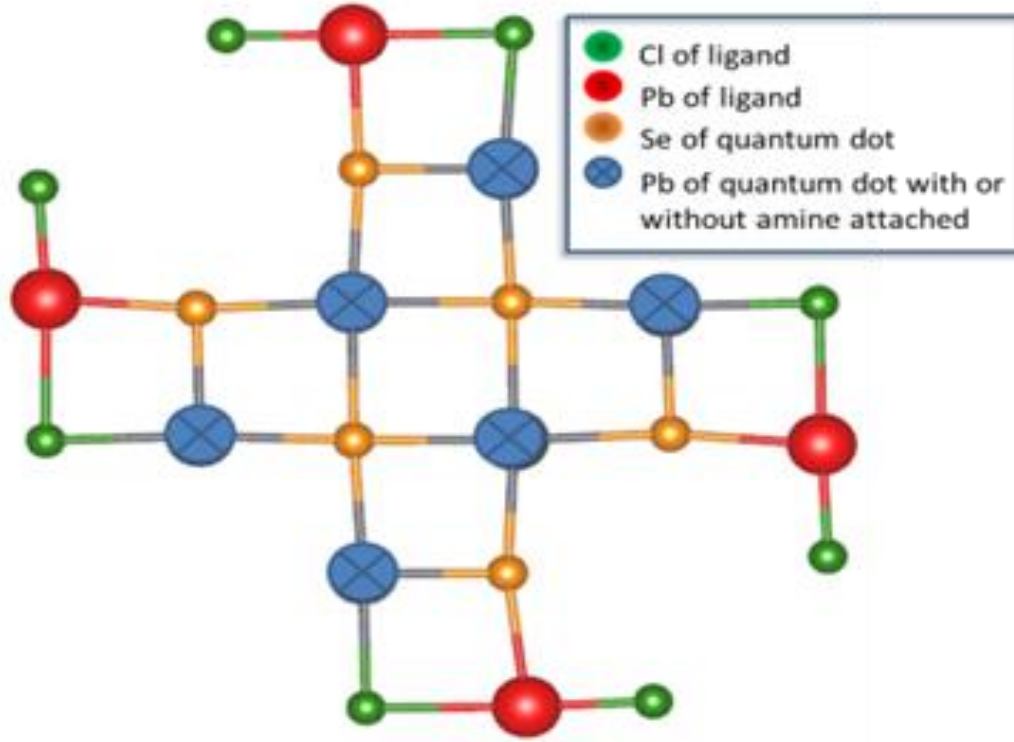


Figure 4.10. 100 surface of $(\text{PbSe})_{68}$ quantum dot with 12 PbCl_2 on 110 surfaces growing in x , x' , y and y'

Surface energy for the formation of 2D plate of $(\text{PbSe})_{68}$ quantum dot along 4 of 100 surfaces, passivated by PbCl_2 at 110 sites and 2 of CH_3NH_2 ligands on each side of left over 100 surfaces denoted by $\gamma_{\text{PbCl}_2 + \text{CH}_3\text{NH}_2}^{2D}$, can be calculated as follows:

$$\gamma_{\text{PbCl}_2 + \text{CH}_3\text{NH}_2}^{2D} = \frac{1}{4 A_{100}} (E_{2D/(\text{QD}-\text{PbCl}_2-\text{CH}_3\text{NH}_2)} - 32E_{\text{Pb}} - 24E_{\text{Se}} - 16E_{\text{Cl}}) \quad (4.5)$$

Where number '2' represents the QD growing in four directions, $E_{2D/(\text{QD}-\text{PbCl}_2-\text{CH}_3\text{NH}_2)}$ is energy of 2D plate of PbSe quantum dot covered with PbCl_2 on 110 and amines covered on leftover 100 surfaces. As shown in Figure 4.10, 4 of 100 sites contain 10 of Pb atoms, 6 of Se atoms and 8 of Chlorine atoms. For the 4 surfaces, a total of $8 * 4 = 32$ Pb (6 Pb of quantum dot and 4 Pb of ligand each shared by an adjacent dot = $4 / 2 = 2$ Pb), 24 Se and 16 Cl atoms are involved in 2D plate formation.

Eq. (4.6) is used to calculate adsorption energy of PbCl₂ in a 2D plate:

$$\Delta G_{PbCl_2}^{2D} = E_{2D/(QD-PbCl_2)} - E_{2D/bare} - 12E_{PbCl_2} \quad (4.6)$$

Eq. (4.7) is used to calculate adsorption energy of PbCl₂ in a 3D box:

$$\Delta G_{PbCl_2}^{3D} = E_{3D/(QD-PbCl_2)} - E_{3D/bare} - 12E_{PbCl_2} \quad (4.7)$$

Eq. (4.8) is used to calculate adsorption energy of amines in a 2D plate:

$$\Delta G_{PbCl_2+CH_3NH_2}^{2D} = E_{2D/(QD-PbCl_2-CH_3NH_2)} - E_{2D/(QD-PbCl_2)} - 12E_{CH_3NH_2} \quad (4.8)$$

Total surface energy of 2D plate of (PbSe)₆₈ covered with 12PbCl₂ growing in 4 directions of 100 is given by:

$$\gamma_{110}^{bare} + \gamma_{PbCl_2}^{2D} + \frac{1}{4A_{100}} * \Delta G_{PbCl_2}^{2D} \quad (4.9)$$

Total surface energy of 3D box of (PbSe)₆₈ covered with 12PbCl₂ growing in all 6 directions of 100 is given by:

$$\gamma_{110}^{bare} + \gamma_{PbCl_2}^{3D} + \frac{1}{2(A_{xy} + A_{yz} + A_{zx})_{100}} * \Delta G_{PbCl_2}^{3D} \quad (4.10)$$

Total surface energy of 2D plate of (PbSe)₆₈ covered with 2 of amines on each of two 100 surfaces and 12PbCl₂, growing in 4 directions of 100 is given by:

$$(\gamma_{110}^{bare}) + (\gamma_{PbCl_2+CH_3NH_2}^{2D}) + (\gamma_{100}^{amines}) + \frac{1}{4A_{100}} * (\Delta G_{PbCl_2+CH_3NH_2}^{2D}) \quad (4.11)$$

4.2.3. Results and Discussions

In order to provide insights into formation and growth direction of NPLs, we first model PbSe QDs of about 1 nm (PbSe)₁₆ and 2 nm (PbSe)₆₈ in diameters constructed from a bulk rock-salt lattice as described elsewhere. Both nanostructures clearly exhibit three main surfaces: (100), (110) and (111), Figure 4.11a. To investigate in which form chlorines and amine ligands are

bound to specific QD's surface, we optimize geometries of QDs with attached surfactants at their different confirmations as shown in Fig. Figure 4.11a

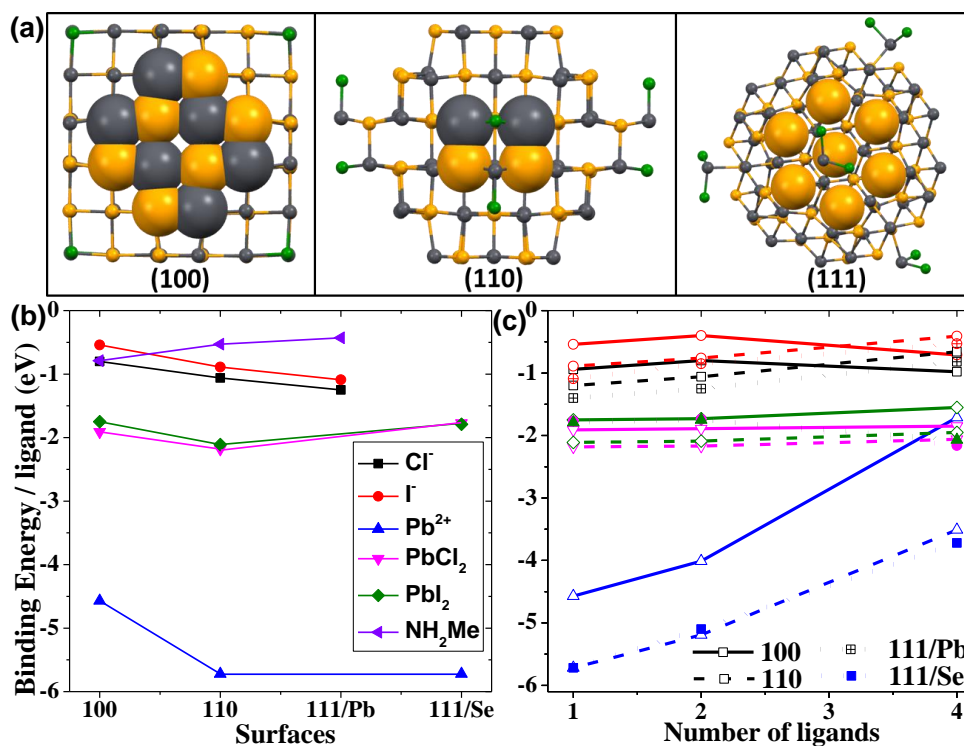


Figure 4.11. (a) Represents three main crystallographic surfaces of (PbSe)₆₈: six (100), twelve (110) passivated by PbCl₂ ligands, and four Pb-terminated and four Se-terminated (111). Selenium atoms are colored in yellow, leads are in grey, and chlorines are in green. The binding energy between the (PbSe)₆₈ QD and different ligands calculated in propyl amine solvent media. (b) A single ligand attached on (100), (110), and (111) crystal lattice surfaces of the QD. (c) Multiple ligands passivate either (100), or (110), or (111) surfaces of the QD.

Calculations of the QD-ligand binding energies show that a small amount of Pb²⁺ cations in solution strongly and preferentially binds to (111) and (110) surfaces of the (PbSe)₆₈ QD, creating reactive sites for binding of halide anions. These likely results in formation of PbCl₂ or PbI₂ neutral ligands strongly interacting with these surfaces even at high concentrations, while the interaction of charged species with the QD drastically decreases with their number, Figure 4.11.b and Figure 4.11.c. In contrast, primary amines (NH₂Me used as a reduced model of long

chain amine ligands to decrease computational cost) are the weakest interacting species preferentially binding to the (100) surface, Figure 4.11.b.

Table 4.4. Binding energy of single ligand on different surfaces

Ligand attachment face on (PbSe) ₆₈	Binding energy per ligand (eV)					
	Cl ⁻	I ⁻	Pb ²⁺	PbCl ₂	PbI ₂	NH ₂ Me
100	-0.8	-0.54	-4.57	-1.91	-1.75	-0.79
110	-1.06	-0.89	-5.72	-2.18	-2.11	-0.53
111	-1.25	-1.09	-5.72	-1.77	-1.79	-0.43

Table 4.5. Binding energy per ligand calculated in case of attachment of multiple ligands on different surfaces

Ligand attachment face on (PbSe) ₆₈	Number of ligands attached	Binding energy per ligand (eV)				
		Cl ⁻	I ⁻	Pb ²⁺	PbCl ₂	PbI ₂
100	1	-0.94	-0.54	-4.57	-1.91	-1.75
	2	-0.80	-0.40	-4.01	-1.89	-1.73
	4	-0.98	-0.71	-1.71	-1.85	-1.55
110	1	-1.20	-0.89	-5.72	-2.18	-2.11
	2	-1.06	-0.76	-5.19	-2.17	-2.09
	4	-0.66	-0.41	-3.51	-2.06	-1.95
111	1	-1.40	-1.09	-5.72	-1.77	-1.79
	2	-1.25	-0.85	-5.10	-1.74	-1.75
	4	-0.82	-0.53	-3.72	-2.16	-2.07

Overall, our calculations reveal selective attachment of neutral PbCl_2 to (110) and/or (111) surfaces of the stoichiometric PbSe QDs, which dominate the binding of Cl anions. Previous calculations of anionic ligands have shown a more rapid ligand coverage of the (111) facets than the (100) facets of PbSe QDs at small ligand concentrations.³⁵ As such, amine ligands are expected to mainly passivate (100) surfaces, despite their much weaker interaction with the QD compared to PbCl_2 . The ionic bond between the surface Se and PbCl_2 or PbI_2 explains more forceful interaction between the QD and lead halides than with amines interacting with the QD via coordinated bonds. Such weaker interactions of amines with the QD, allows us to assume that amine ligands are easy to be exchanged or eliminated from the (100) surface. Thus random collisions between QDs would transfer enough energy to amines to be detached from the surface, leaving the (100) surface empty from ligands, and thus providing favorable conditions for QD-QD binding along (100) crystal direction.

Another important finding is formation of Cl-Pb-Cl bridges between adjacent QDs with PbCl_2 passivating (110) and/or (111) surfaces as shown in Figure 4.12. For more realistic inclusion of QD-QD interactions, we utilize periodic boundary conditions to mimic QDs growing in 2-D and 3-D directions. Starting with the optimized $(\text{PbSe})_{68}$ with fully or partially passivated (110) surfaces by PbCl_2 , the final 2-D structures of NPLs demonstrate appearance of Pb-Cl-Pb bridging network with neighboring QDs along (100) lattice direction, as illustrated in Figure 4.13 and Table 4.6. The main reason for the formation of (100)-ordered NPLs facilitated by PbCl_2 capping of (110) or (111) surfaces is that the bond distance of Pb-Cl is close to that of Pb-Se, so that chlorines restore defects originated from the missed surface selenium in the QD's crystal lattice.

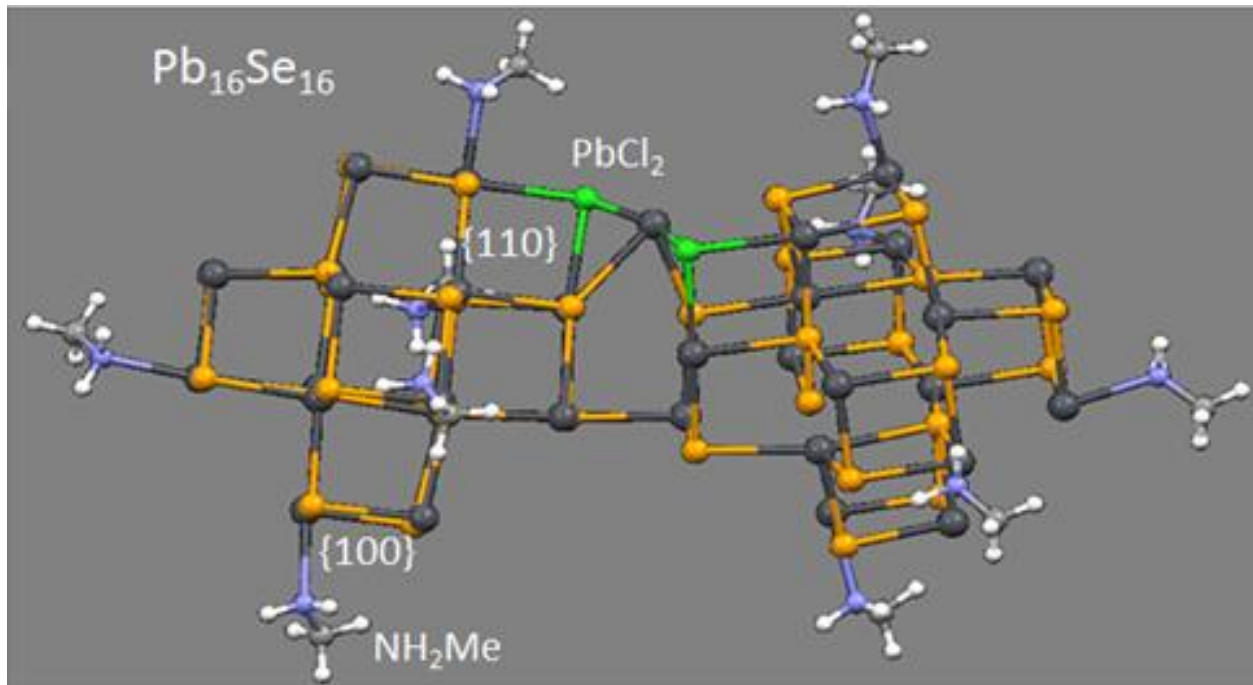


Figure 4.12. Gaussian simulations of two PbSe QDs passivated with amines on 5 different (100) sites and PbCl₂ on (110). After relaxation, PbCl₂ at (110) tend to form a bridge between two QDs.

Importantly, creation of the bridging network is more energetically favorable in 2-D, rather than 3-D directions, as can be seen from comparing the surface energy shown in Figure 4.13. Addition of amines on the top and bottom of (100) surfaces that are not involved in 2-D network, significantly stabilize the NPL energy, as compared to 3-D super lattice. This evidences thermodynamic preferences of (100)-ordered attachments of QDs in 2-D NPLs. Moreover, the surface energy of 2-D structures formed by (PbSe)₁₆ of ~1 nm in size is significantly less stable compared to those of 2 nm (PbSe)₆₈ QDs with PbCl₂ capping (110) surface. This explains the minimal thickness of NPLs being of ~2 nm, as observed in experiments: For PbSe QDs, it is more energetically favorable to grow up to 2 nm in size and then form NPLs.

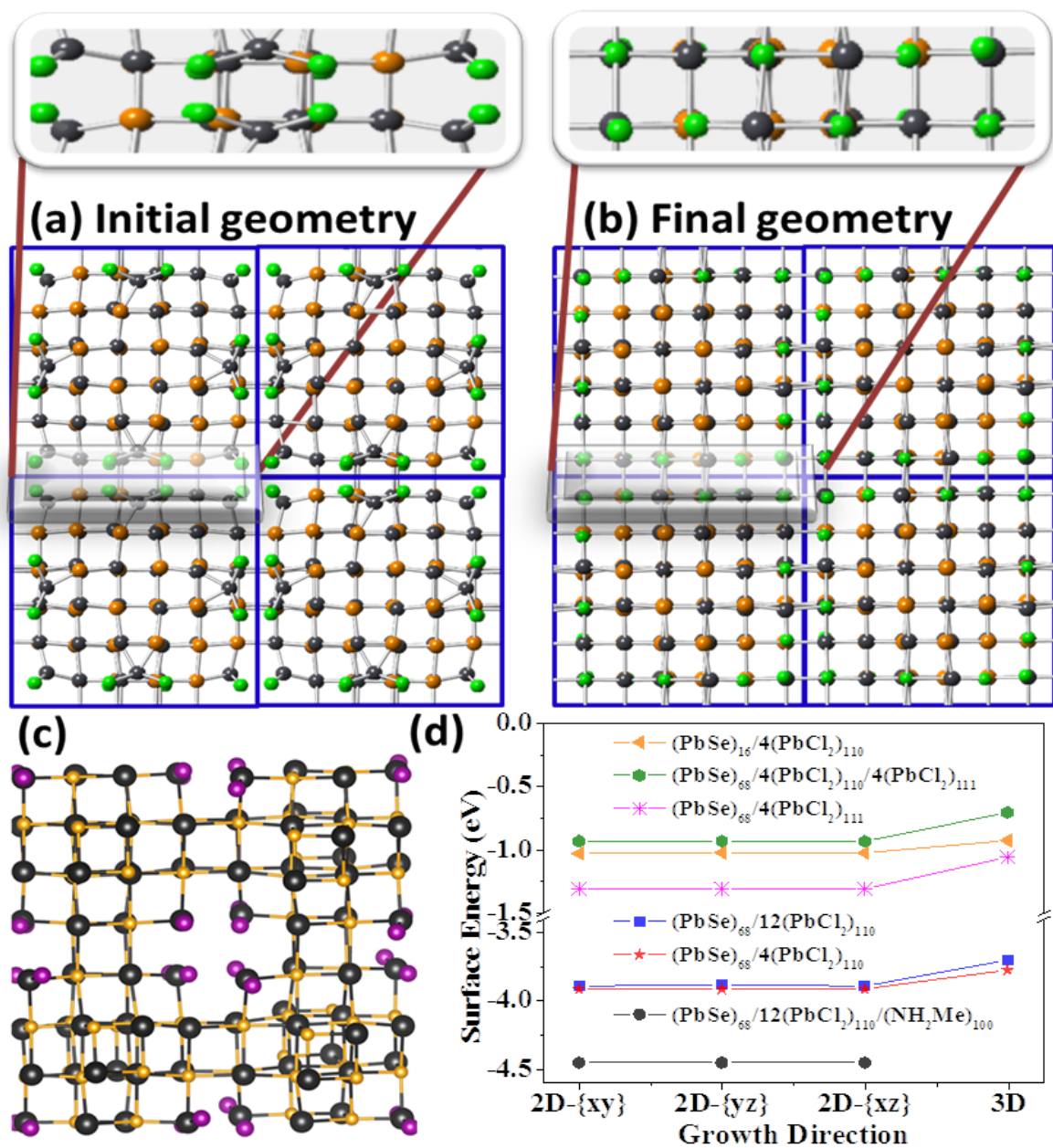


Figure 4.13. (a) and (b) are the geometries of $(\text{PbSe})_{68}$ QD passivated fully at (110) surface by PbCl_2 , before and after relaxation utilizing periodic boundary conditions to mimic QD-QD interactions in 2-D and 3-D directions. 2D network is stabilized due to formations of Pb-Cl-Pb bridging bonds selectively connecting neighboring QDs along (100) surface. Zoomed in pictures of before and after relaxations were projected to show the better visualization of the Pb-Cl-Pb bridge formations (c) Optimized geometry of 2-D structure constructed from $(\text{PbSe})_{68}$ QD with fully passivated (110) surface by PbI_2 ligands. Lacking of Pb-I-Pb bridging bonds reduce ordering and destabilize the 2-D array. (d) The calculated surface energy as a function of 2-D and 3-D super lattices constructed from $(\text{PbSe})_{16}$ or $(\text{PbSe})_{68}$ QDs with PbCl_2 ligands passivating either (110) or (111) or both surfaces with and without NH_2Me ligands capping (100) facets inactive in 2-D array formation.

Table 4.6. Surface energy of the $(\text{PbSe})_{68}$ quantum dot passivated by PbCl_2 ligands in either 110 or 111 or both as labelled below. Values in parenthesis show surface energies for $(\text{PbSe})_{68}$ quantum dot passivated by 12 PbCl_2 ligands on 110 surface growing along x and y directions. The z direction is passivated by 6 methyl amines on each side.

System		$(\text{PbSe})_{68}/$ $12(\text{PbCl}_2)_{110}$	$(\text{PbSe})_{68}/$ $4(\text{PbCl}_2)_{110}$	$(\text{PbSe})_{68}/$ $4(\text{PbCl}_2)_{111}$	$(\text{PbSe})_{68}/$ $4(\text{PbCl}_2)_{110}/$ $4(\text{PbCl}_2)_{111}$	$(\text{PbSe})_{16}/$ $4(\text{PbCl}_2)_{110}$
2D	xy	-3.8954 (-4.4574)	-3.9170	-1.3124	-0.9346	-1.0322
	yz	-3.8833 (-4.4575)	-3.9167	-1.3131	-0.9345	-1.0246
	zx	-3.8954 (-4.4572)	-3.9167	-1.3132	-0.9360	-1.02794
3D	xyz	-3.7038	-3.7764	-1.0606	-0.7067	-0.9276

In contrast, lead iodide precursors do not contribute to the bridging attachment due to a mismatch between Pb-I and Pb-Se bond lengths: Pb-I bond length is too long, as illustrated in Figure 4.13. Therefore, despite a strong interaction between the QD and PbI_2 , which is just slightly smaller than those with PbCl_2 (Fig. 2b, 2c), PbI_2 prevents the formation of NPLs, since this process is energetically unfavorable in absence of Pb-I-Pb bridging network. These calculations suggest that the use of PbCl_2 as a precursor is of great importance to the attachment process. Because of the strength of Pb-Cl bonds, and the abundance of Cl^- in solution, a large fraction of PbCl_2 tends to remain un-dissociated under reaction conditions, while strongly bind to (110) or (111) surfaces; moreover, the Cl-Pb-Cl bridge is of an appropriate bond length to favor selectively oriented coupling between opposing (100) surfaces of adjacent QDs, while top and bottom (100) facets inactive in 2-D growth are capped by amines.

Table 4.7. VASP optimized structures of the $(\text{PbSe})_{68}$ and $(\text{PbSe})_{16}$ quantum dot passivated by PbCl_2 ligands in either 110 or 111 or both as labelled below

System	'2D' xy projected along (100)	'2D' yz projected along (100)	'2D' zx projected along (100)	'3D' xyz projected along (111)
$(\text{PbSe})_{68} + (12(\text{PbCl}_2))_{110}$				
$(\text{PbSe})_{68} + (4(\text{PbCl}_2))_{110}$				
$(\text{PbSe})_{68} + (4(\text{PbCl}_2))_{111}$				
$(\text{PbSe})_{68} + (4(\text{PbCl}_2))_{110} + (4(\text{PbCl}_2))_{111}$				
$(\text{PbSe})_{16} + (4(\text{PbCl}_2))_{110}$				

The last question remained is why addition of small concentration of PbI_2 to PbCl_2 precursors resulted in increase of the nanoplates thickness in discrete manner from 2 nm to 4 nm to 6 nm, depending on reaction time. To address this question, we simulated two structures where PbX_2 ($X = \text{Cl}$ or I) are placed on (100) surface of $(\text{PbSe})_{68}$ fully passivated by amines at (100) with (110) surfaces fully capped by PbCl_2 as shown in Figure 4.14. Our DFT calculations show that either PbCl_2 or PbI_2 placed near the (100) surface, exhibit dissociation into halide ion that exchange the nearest amine on the (100) surface. Left PbCl^+ cation stays at the same (100) surface and is coordinated with the exchanged amine, because it still ‘fills’ some interaction with the dissociated Cl^- ion. In contrast, weaker electronegativity of dissociated iodine does weaken the interaction with the PbI^+ cation; therefore, it moves to the adjacent more reactive (111) surface, while amine is also completely kicked out from its initial (100) site. In addition, dissociation of PbI_2 at (100) surface leading to amine exchange is more rapid and efficient than those of PbCl_2 , since the bond energy of Pb-Cl (2.5 eV) is stronger than that of Pb-I (1.5 eV).³⁶ As such, PbI_2 provides more efficient ‘cleaning’ of amines from the top and bottom (100) surfaces allowing for merging of two NPLs together resulting in nearly twice thicker NPLs.

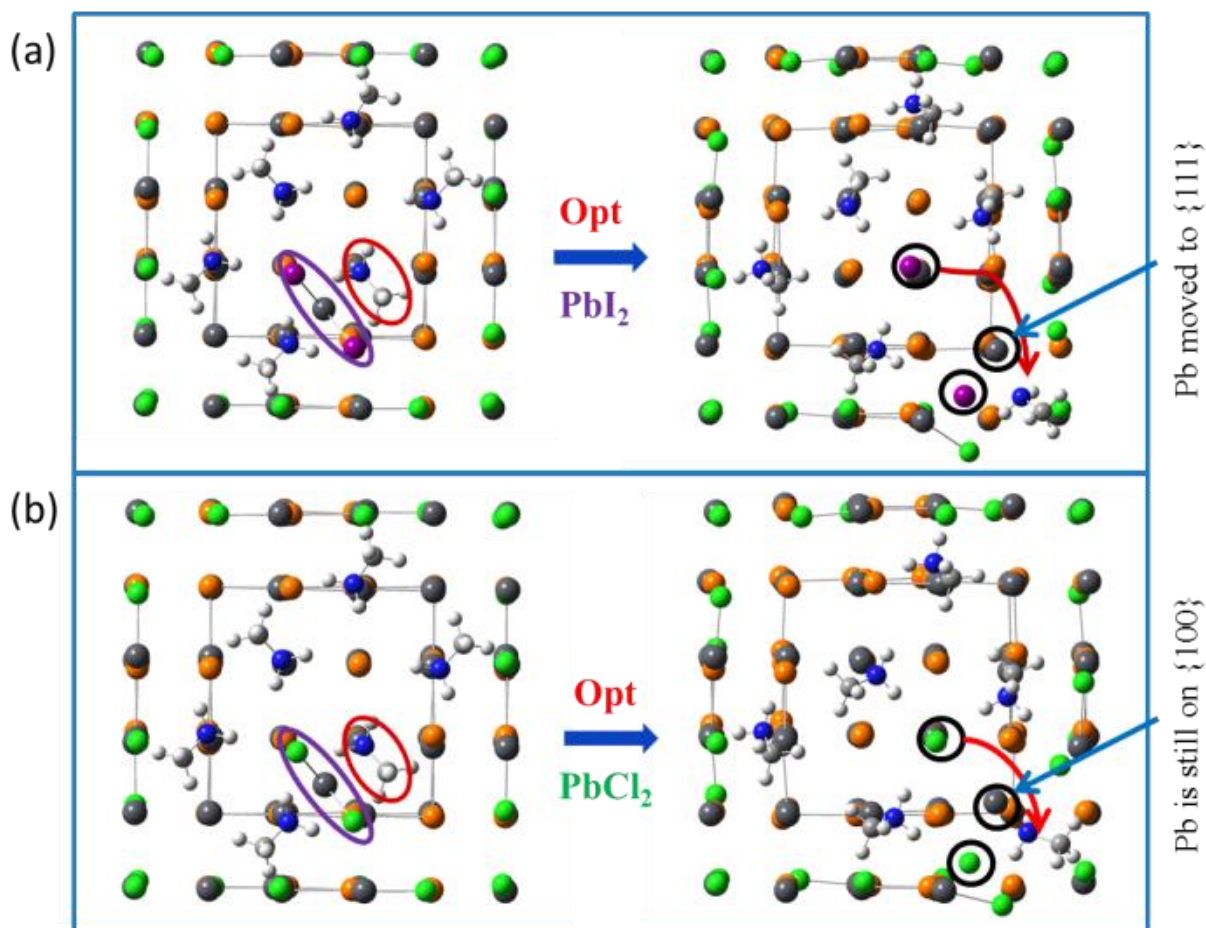


Figure 4.14. Geometry relaxation of $(\text{PbSe})_{68}$ quantum dot passivated by 12 PbCl_2 ligands in either 110, with amines on (100) direction. (a) PbI_2 is placed at (100) and relaxed (b) PbCl_2 is placed at (100) and relaxed.

4.2.4. Conclusions

In conclusion, we report the synthesis of quasi-2D PbSe NPLs wherein the thickness can be controlled by choice of lead halide precursor. DFT calculations show that there is a tendency of amines to weakly bind on the (100) sites, whereas PbCl_2 tend to very strongly interact with the (110) and (111) sites providing the Pb-Cl-Pb bridging network with neighboring QDs along (100) lattice direction and forming 2-D NPLs. In contrast, PbI_2 does not provide the bridging network due to mismatch between Pb-I and Pb-Se bond lengths, which explains random aggregation of QDs that do not form regularly shaped NPLs when PbI_2 is used in synthesis. However, using PbI_2 with excess Cl^- allows for controlling the thickness of NPLs discreetly

varying from 2.1 nm to 4.2 nm and 6.3 nm. We address it to higher ability of PbI₂ to dissociate at the amine passivated (100) surface leading to amine exchange. Rapid desorption of amines from the (100) surface provides a room for the NPLs to grow in the third direction via fusing of two or three NPLs together.

4.3. References

- 1 Medintz, I. L., Uyeda, H. T., Goldman, E. R. & Mattoussi, H. Quantum dot bioconjugates for imaging, labelling and sensing. *Nat Mater* **4**, 435-446, doi:10.1038/nmat1390 (2005).
- 2 Dohnalova, K., Gregorkiewicz, T. & Kusova, K. Silicon quantum dots: surface matters. *J Phys-Condens Mat* **26**, doi:Artn 173201 10.1088/0953-8984/26/17/173201 (2014).
- 3 Dohnalova, K. *et al.* Surface brightens up Si quantum dots: direct bandgap-like size-tunable emission. *Light-Sci Appl* **2**, doi:ARTN e47 10.1038/lisa.2013.3 (2013).
- 4 Valenta, J., Greben, M., Gutsch, S., Hiller, D. & Zacharias, M. Effects of inter-nanocrystal distance on luminescence quantum yield in ensembles of Si nanocrystals. *Appl Phys Lett* **105**, doi:Artn 243107 10.1063/1.4904472 (2014).
- 5 Miller, J. B. *et al.* Ensemble Brightening and Enhanced Quantum Yield in Size-Purified Silicon Nanocrystals. *Acs Nano* **6**, 7389-7396, doi:10.1021/nn302524k (2012).
- 6 Fernee, M. J., Tamarat, P. & Lounis, B. Spectroscopy of single nanocrystals. *Chem Soc Rev* **43**, 1311-1337, doi:10.1039/c3cs60209e (2014).
- 7 Perdew, J. P., Burke, K. & Ernzerhof, M. Generalized Gradient Approximation Made Simple [Phys. Rev. Lett. 77, 3865 (1996)]. *Physical review letters* **78**, 1396-1396 (1997).
- 8 Hariharan, P. C. & Pople, J. A. The influence of polarization functions on molecular orbital hydrogenation energies. *Theoret. Chim. Acta* **28**, 213-222, doi:10.1007/bf00533485 (1973).

- 9 Frisch, M. J. *et al.* *Gaussian 09*. (Gaussian, Inc., 2009).
- 10 Martin, R. L. Natural transition orbitals. *The Journal of chemical physics* **118**, 4775-4777 (2003).
- 11 Hines, M. A. & Guyot-Sionnest, P. Bright UV-blue luminescent colloidal ZnSe nanocrystals. *The Journal of Physical Chemistry B* **102**, 3655-3657 (1998).
- 12 Manna, L., Scher, E. C. & Alivisatos, A. P. Synthesis of soluble and processable rod-, arrow-, teardrop-, and tetrapod-shaped CdSe nanocrystals. *J. Am. Chem. Soc.* **122**, 12700-12706 (2000).
- 13 Ithurria, S. *et al.* Colloidal nanoplatelets with two-dimensional electronic structure. *Nat. Mater.* **10**, 936-941, doi:<http://www.nature.com/nmat/journal/v10/n12/abs/nmat3145.html#supplementary-information> (2011).
- 14 Pelton, M., Ithurria, S., Schaller, R. D., Dolzhenkov, D. S. & Talapin, D. V. Carrier Cooling in Colloidal Quantum Wells. *Nano Letters* **12**, 6158-6163, doi:10.1021/nl302986y (2012).
- 15 She, C. *et al.* Low-Threshold Stimulated Emission Using Colloidal Quantum Wells. *Nano Lett.* **14**, 2772-2777 (2014).
- 16 Luther, J. M. *et al.* Stability Assessment on a 3% Bilayer PbS/ZnO Quantum Dot Heterojunction Solar Cell. *Adv. Mat.* **22**, 3704-3707 (2010).
- 17 Stewart, J. T. *et al.* Carrier Multiplication in Quantum Dots within the Framework of Two Competing Energy Relaxation Mechanisms. *J. Phys. Chem. Lett.* **4**, 2061-2068, doi:10.1021/jz4004334 (2013).

- 18 Semonin, O. E. *et al.* Peak External Photocurrent Quantum Efficiency Exceeding 100% via MEG in a Quantum Dot Solar Cell. *Science* **334**, 1530-1533, doi:Doi 10.1126/Science.1209845 (2011).
- 19 Klimov, V. I. Detailed-balance power conversion limits of nanocrystal-quantum-dot solar cells in the presence of carrier multiplication. *Applied Physics Letters* **89**, 123118, doi:doi:http://dx.doi.org/10.1063/1.2356314 (2006).
- 20 Bakueva, L. *et al.* Size-tunable infrared (1000–1600 nm) electroluminescence from PbS quantum-dot nanocrystals in a semiconducting polymer. *Applied Physics Letters* **82**, 2895-2897, doi:doi:http://dx.doi.org/10.1063/1.1570940 (2003).
- 21 Rao, G. N. & Karpf, A. External cavity tunable quantum cascade lasers and their applications to trace gas monitoring. *Applied optics* **50**, A100-A115 (2011).
- 22 Zhang, H. *et al.* Colloidal Synthesis of PbS and PbS/CdS Nanosheets Using Acetate-Free Precursors. *Chemistry of Materials* **28**, 127-134, doi:10.1021/acs.chemmater.5b03348 (2016).
- 23 Aerts, M. *et al.* Highly efficient carrier multiplication in PbS nanosheets. *Nat Commun* **5**, 3789 (2014).
- 24 Lee, S. *et al.* Slow Colloidal Growth of PbSe Nanocrystals for Facile Morphology and Size Control. *RSC Adv.*, doi:10.1039/c3ra46875e (2014).
- 25 Weon-kyu Koh, N. D., Andrew F. Fidler, Victor I. Klimov, Jeffrey M. Pietryga, and Svetlana V. Kilina. (2016).
- 26 Kamisaka, H., Kilina, S. V., Yamashita, K. & Prezhdo, O. V. Ultrafast Vibrationally-Induced Dephasing of Electronic Excitations in PbSe Quantum Dots. *Nano Lett.* **6**, 2295-2300, doi:10.1021/nl0617383 (2006).

- 27 Perdew, J. P., Burke, K. & Ernzerhof, M. Generalized Gradient Approximation Made Simple. *Physical review letters* **77**, 3865-3868 (1996).
- 28 Wadt, W. R. & Hay, P. J. Ab initio effective core potentials for molecular calculations. Potentials for main group elements Na to Bi. *The Journal of Chemical Physics* **82**, 284-298, doi:doi:http://dx.doi.org/10.1063/1.448800 (1985).
- 29 Barone, V., Cossi, M. & Tomasi, J. Geometry optimization of molecular structures in solution by the polarizable continuum model. *Journal of Computational Chemistry* **19**, 404-417, doi:10.1002/(sici)1096-987x(199803)19:4<404::aid-jcc3>3.0.co;2-w (1998).
- 30 Kresse, G. & Furthmuller, J. Efficiency of ab-initio total energy calculations for metals and semiconductors using a plane-wave basis set. *Computational Materials Science* **6**, 15-50 (1996).
- 31 Kresse, G. & Joubert, D. From ultrasoft pseudopotentials to the projector augmented-wave method. *Physical Review B* **59**, 1758-1775 (1999).
- 32 Blöchl, P. E. Projector augmented-wave method. *Physical Review B* **50**, 17953-17979 (1994).
- 33 Kilina, S. V., Kilin, D. S. & Prezhdo, O. V. Breaking the Phonon Bottleneck in PbSe and CdSe Quantum Dots: Time-Domain Density Functional Theory of Charge Carrier Relaxation. *ACS Nano* **3**, 93-99, doi:10.1021/nn800674n (2009).
- 34 Fischer, G., Poteau, R., Lachaize, S. & Gerber, I. C. Surfaces of a Colloidal Iron Nanoparticle in Its Chemical Environment: A DFT Description. *Langmuir* **30**, 11670-11680, doi:10.1021/la502963n (2014).

- 35 Bealing, C. R., Baumgardner, W. J., Choi, J. J., Hanrath, T. & Hennig, R. G. Predicting Nanocrystal Shape through Consideration of Surface-Ligand Interactions. *ACS Nano* **6**, 2118-2127, doi:10.1021/nn3000466 (2012).
- 36 Huheey, J. E. *Inorganic Chemistry: Principles of Structures and Reactivity*. (Harper & Row, 1972).